Investigation of Low-Power Integrated Optical Switches and Modulators

Fatemeh Soltani

Department of Electrical and Computer Engineering
McGill University
Montréal, Québec, Canada
April 2018

A thesis submitted to McGill University in partial fulfillment of the requirements
of the degree of Doctor of Philosophy
© Fatemeh Soltani, 2018

To my Family

Abstract

With recent increasing demands for higher capacity in optical networks, there is a need for high-speed optical modulation. This desire is especially pronounced with the growth of high volume data centers. There is a demand for low-power modulators that can be placed on printed circuit boards. Mach-Zehnder modulators (MZM)s, in a range of different materials, are widely used for this purpose. However, their power consumption is determined by the relatively large electrode size which they require. Some time ago researchers in optical fiber switches introduced the concept of the loop-mirror for nonlinear applications. This device is conceptually an MZM in which two outputs are connected to make a loop at the end. Although loop-mirror was introduced in nonlinear optical switching it also can be used as an optical modulator.

In this thesis, we introduce for the first time an integrated loop-mirror modulator (LMM). We show that this device requires one-half the switching voltage and one-quarter the power consumption of a conventional MZM. This device is implemented in silicon-on-insulator technology with carrier depletion junctions. The reverse-biased PN junction modulator is fabricated with two different electrode configurations (series push-pull and dual-drive). On-Off Keying (OOK) modulation at 20 Gb/s and Differential phase shift keying (DPSK) modulation at 10 Gb/s is demonstrated experimentally. The frequency response of the LMM is analyzed and we conclude that the power efficiency gains of the LMM are only present in the lumped electrode regime. In the traveling-wave (TW) electrode regime it is not possible to simultaneously velocity match the forward and backward going optical and electrical waves in the electrodes. As a reflective modulator the proposed LMM could find applications in passive optical networks (PON).

Sommaire

Les récentes augmentations de la demande pour des réseaux optiques à plus grande capacité ont généré un besoin pour de la modulation optique à grande vitesse. Ce désir est spécialement marqué par la croissance des centres de données à volume élevé. Il y a une demande pour des modulateurs à faible puissance qui peuvent être mis en place sur des cartes de circuits imprimés. Les modulateurs de Mach-Zehnder (MZM) sont fréquemment utilisés à cette fin. Cependant, leur consommation en puissance est déterminée par la grande taille des électrodes qu'ils requièrent. Par le passé, des recherches sur les commutateurs à fibre optique ont introduit le concept des modulateurs à boucle (LMM). Ce dispositif est conceptuellement un MZM dont deux sorties sont connectées pour créer une boucle. Bien que la boucle réfléchissante fût instaurée pour les commutateurs optiques non-linéaires, elle peut aussi être utilisée dans un modulateur optique.

Dans cette thèse, nous présentons pour la première fois un LMM intégré. Nous démontrons que ce dispositif ne requière que la moitié du voltage de commutation et qu'un quart de la puissance qu'un MZM conventionnel. Ce dispositif est implémenté avec la technologie silicium-sur-isolant (SOI) avec des jonctions fonctionnant en déplétion. Le modulateur à jonction PN à polarisation inverse est fabriqué avec deux configurations d'électrode différentes (symétrique et double-entrainement). La modulation par tout ou rien (OOK) à 20 Gb/s et la modulation de phase différentielle (DPSK) à 10 Gb/s sont démontrées expérimentalement. La réponse en fréquence du LMM est analysée et nous concluons que les gains en efficacité de puissance du LMM ne sont présents que dans le régime d'électrode localisée. Dans le régime d'électrode par ondes progressives (TW) il n'est pas possible de faire coïncider les vitesses des ondes avant et arrière optiques et électriques dans

les électrodes. En tant que modulateur réflectif, le LMM présenté pourrait être utile pour certaines applications sur les réseaux optiques passifs (PON).

Table of Contents

Chapter 1

Chapter 2

Chapter 3

Chapter 4

Chapter 5

Chapter 6

Chapter 7

List of Figures

List of Tables

List of Abbreviations

ACP	Asia Communications and Photonics
AWG	Arrayed waveguide grating
BER	Bit error rate
BPG	Bit pattern generator
BPSK	Binary phase shift keying
CMOS	Complementary-metal-oxide-semiconductor
CO	Central office
CW	Continuous wave
DCA	Digital communication analyzer
DFB	Distributed feedback laser
DOS	Digital optical switch
DPSK	Differential phase shift keying
DQPSK	Differential quadrature phase shift keying
DWDM	Dense wavelength division multiplexing
EAM	Electro-absorption modulator
ED	Error detector
EDFA	Erbium-doped fiber amplifier
EO	Electro-optic
ER	Extinction ratio
FP	Fabry-Perot
FPI	Fabry-Perot interferometer
FSR	Free spectrum range
FTTH	Fiber to the home
FWHM	Full width at half maximum
GaAs	Gallium arsenide
GPON	Gigabit passive optical networks

GS	Ground-signal
GSGSG	Ground-signal-ground-signal-ground
IO	Input/output
IPC	IEEE Photonics Conference
InP	Indium phosphide
LMM	Loop-Mirror Modulator
MEMS	Micro-electro-mechanical systems
MMI	Multimode interference
MOS	Metal-oxide-semiconductor
MZI	Mach-Zehnder interferometer
MZM	Mach-Zehnder modulator
NRZ	Non-return-to-zero
NSERC	National sciences and engineering research council
OEO	Optical-electronic-optical
OLT	Optical line terminal
ONU	Optical network unit
OOK	On-Off Keying
OPL	Optical path length
OpSIS	Optoelectronic systems integration in silicon
OSNR	Optical signal-to-noise ratio
OXC	Optical cross connect
PD	Photodetector
PIC	Photonic integrated circuits
PIN	Positive-Intrinsic-Negative
PLC	Planar Lightwave Circuits
PLZT	Polarized Lead Zirconium Titanate
PN	Positive-Negative
PON	Passive optical networks
PRBS	Pseudo-random bit sequence
QPSK	Quadrature phase shift keying

RC	Resistor-Capacitor
RF	Radio frequency
RSOA	Reflective semiconductor optical amplifier
SOHO	Small office-home office
SOI	Silicon-on-insulator
TDM	Time division multiple
TE	Transverse electric
TEC	Thermoelectric cooler
TIA	Trans-impedance amplifier
TM	Transverse magnetic
TO	Thermo-optical
TW	Traveling-wave
VLSI	Very-large-scale integration
VOA	Variable optical attenuator
WDM	Wavelength division multiplexing

Acknowledgments

First of all, I would like to thank my advisor Prof. Andrew G. Kirk for the guidance and support that he has provided to me throughout the course of my Ph.D. program. I am grateful to him for all fruitful discussions in the last few years and for teaching me how to think critically. Thanks for giving me the opportunity to explore science under your supervision!

Additionally, I would like to thank Professor Michaël Ménard (UQAM) for sharing his knowledge and suggestions that impacted this research project considerably. Thanks for your encouragement throughout my Ph.D. program.

I thank my thesis committee members, Prof. Lawrence Chen (McGill University), and Prof. Amr Helmy (University of Toronto). I am grateful to Sandrine for translating my thesis abstract in French.

I would like to thank my colleagues at the photonic systems group who facilitated a wonderful experience for me at McGill. Venkat Veerasubramanian, Alireza Samani, David Patel, Sandrine Filion Côté, Ahmed Abumazwed, Mohamed Najih, and all the others with whom I had the chance to work along during my time at McGill: thank you, it has been a fun and rewarding experience.

I also appreciate the help in various matters that I received from our amazing administrative assistants, Christopher Rolston, Brent Snow, Maru Basanez, Carrie Serban. Also, my experimental work was not possible without the great help of our excellent assistant in the machine shop, Don. I am grateful to him for providing me machined parts in a timely manner.

During my PhD study I made many friends with whom I enjoyed this adventurous life journey together. Hadi Salmasian, Mahsa Derakhshani, Mohammad Moeini, Saeedeh Parsaeefard, Atoosa Dalili, Maryam Fazel-Zarandi, Nastaran Jafarpour, Niloufar Afsari, Golnaz Ghodoosi pour, Shohreh Shaghaghian, Dena Firoozi, Donya Mohammadshahi, Reyhaneh Rezvani, Malika Meghjani, Isabelle Lacroix, Mehrdad Givi, Somayeh Sadat, Hossein Abouee-Mehrizi, and everyone else with whom I had the chance to share wonderful memories.

Last but not least, I express my deep gratitude to my family: my mother Akram Ensafi, my father Zeyadali Soltani, my brothers Hamed and Omid. Without your love and support it would not have been possible to come this far. Thank you for always standing by my side and granting me the freedom to follow my dreams.

This work has received financial support from the National Sciences and Engineering Research Council (NSERC) of Canada through the Silicon Electronic-Photonic Integrated Circuits (Si-EPIC) CREATE program. In addition, the CMC Microsystems provided me access to the IME fabrication process and to design tools. I also grateful to Prof. Plant’s group at McGill University for technical assistance and providing equipment.

CHAPTER 1

INTRODUCTION

1.1 What is the need behind low-power modulator demand?

The present-day internet comprises over 100 billion web pages on over 100 million websites. This enormous amount of data is being accessed continually by nearly 3 billion users that conduct approximately 3 billion Google searches and send approximately 150 billion emails per day. In 2016 the global user traffic reached more than 42,000 gigabytes per second. With projections of over 600 million users streaming internet high-definition videos simultaneously at peak times, the peak demand is expected to be considerably higher in the near future [1].

All of this data flows via data centers to and from the enterprise, small office-home office (SOHO), and residential access networks, across long-haul telecommunication networks and passive optical networks (PON). Over the last decade, dense wavelength division multiplexing (DWDM) with channel counts of 40 and 100 wavelengths that support 10Gb/s and 40Gb/s data rates per channel have been deployed in the long-haul national and regional backbone networks and metropolitan core networks. The DWDM systems are now being improved with next generation 40Gb/s and 100Gb/s technologies for ultra-long-haul, long-haul and metropolitan networks. The impact of DWDM improvements and size reduction of optical components has been a growth in the capacity of optical networks by seven orders of magnitude in two decades, with no increase in cost or footprint. However, apart from high order modulation applications, the spectral efficiency gains for standard modulation applications are now almost exhausted.

Presently, the focus of data centers is not merely on delivering content to end users. Rather, they are also responsible for data management roles inside the centers before sending information to end users. Recently, with the development of cloud computing and big-data applications, data transfer rates and data management loads have massively increased and sometimes require parallel computing. This brings up the challenge of intra-data-center traffic. Figure 1 shows the trend of traffic increase within data centers [2].

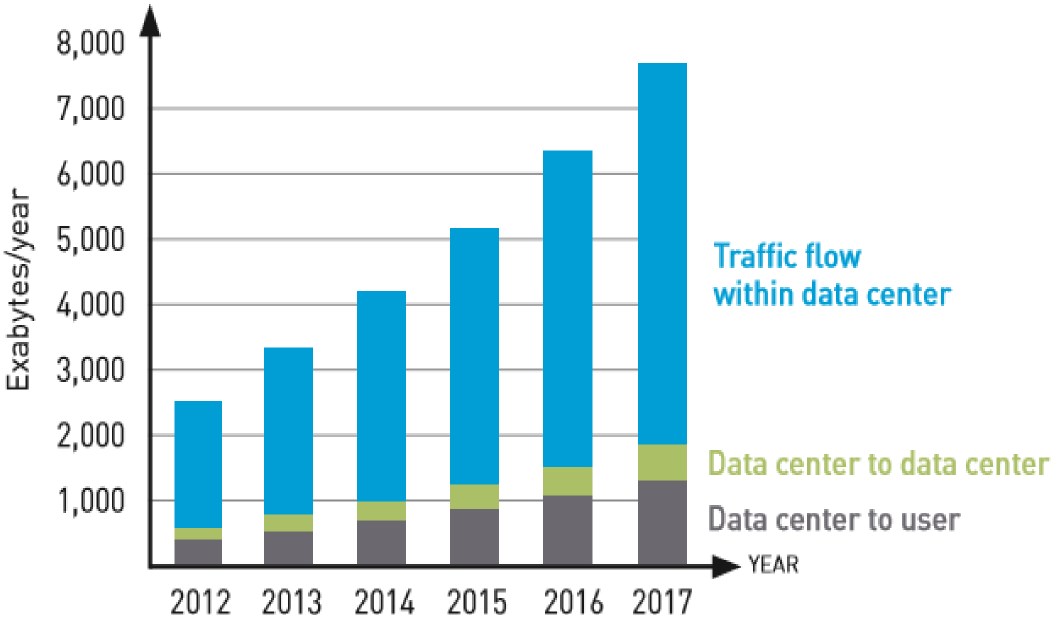

Figure 1 - Traffic flow within data centers (permission received to use from [2])

Figure 2 shows the network traffic growth is much faster than equipment efficiency improvements. An important observation is that the scaling trend for traffic is exponential. This brings up a need for more efficient optical networks in order to close the energy gap. Possible approaches include: 1) lower power and more compact optical components, 2) flexible (elastic) optical systems or software-defined networks that can be actively provisioned, and 3) dynamic optical switching.

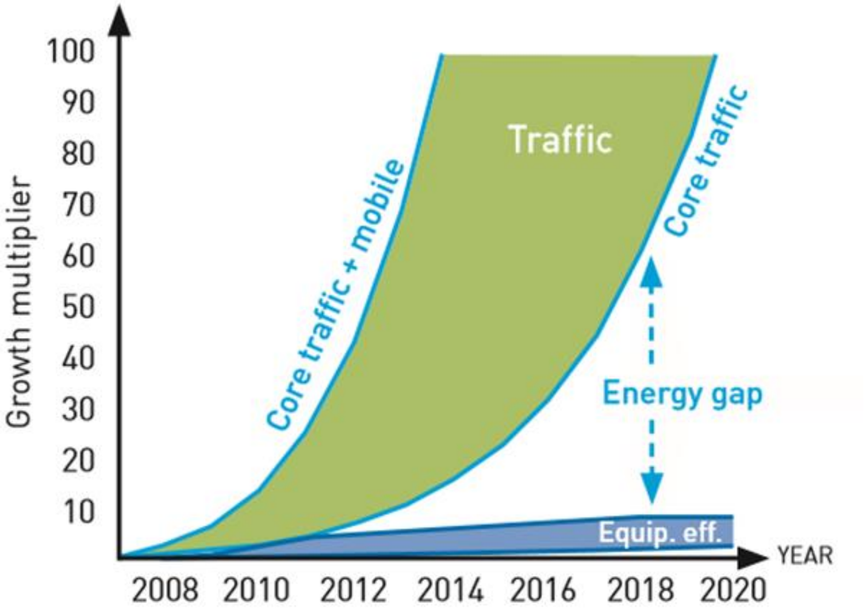

Figure 2 - Network traffic growth vs. equipment efficiency (permission received to use from [2])

Furthermore, power consumption is an emerging problem in data centers. For a single shelf in which the throughput is estimated as 1.2Tbps, the power consumption is about 15kW. For multiple shelves that in general include 80 shelves, for the throughput of 92Tbps, the power consumption is estimated to be more than 1MegaW and an additional power consumption of 1MegaW is required for cooling the central office. For some of the recent Google data centers the power consumption budget is estimated to be more than 100MegaW [13].

Photonic integration is part of the solution to the emerging demand for broad bandwidth and high capacity network equipment. Beside other integrated technologies such as InP (indium phosphide) and GaAs (gallium arsenide), silicon photonics is capable of high-density integration with multiple channels and requires a small footprint and low-power. In recent years foundries have been established to develop on-chip silicon photonics at large-scale.

External modulators, variable optical attenuators and optical gates that employ Mach-Zehnder interferometers (MZI)s are common structures within photonic integrated circuits. In most applications, and in particular in data centers with potentially tens of thousands of optical links with direct board-level applications, low-power consumption is required. Silicon photonics integration got a late start in comparison to the other semiconductor materials. However, since the first demonstration less than a decade ago, the number of component per chip has been doubling year over year (Figure 3).

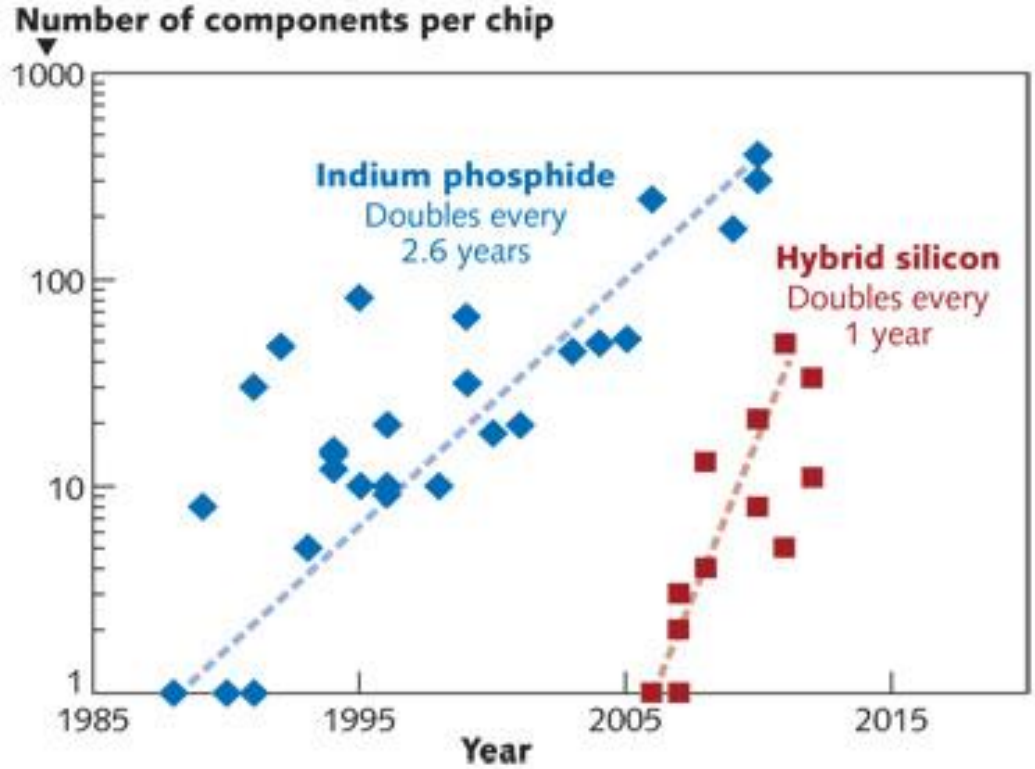

Figure 3 - Silicon photonics evolve to meet real-world requirements (permission received to use from [3])

The above discussion indicates the significance of building MZIs with low phase shift, because with lower phase shift it is possible to achieve reduced power consumption. In this thesis we take a step in this direction by introducing a low-power optical modulator that incorporates an optical loop-mirror.

The main idea of the research presented in this thesis was inspired by previous work on fiber loop-mirrors [4]–[7] that were developed for nonlinear optical processing. A loop-mirror consists of a power divider, generally a directional coupler, where the two outputs on one side of the divider are connected by a loop of fiber or waveguide. Light at the input of the loop-mirror is split in two and each half travels in the opposite direction along the loop. In nonlinear applications, the relative phase between the two halves of the initial signal is controlled by the power of a second signal that propagates in only one direction. Depending on the relative phase of each portion of the initial signal, it can be reflected toward the input or transmitted toward an output port. However, to implement a loop-mirror as an integrated optical modulator rather than as a nonlinear optical switch, it is necessary to control the coupling ratio in the power divider via external actuation.

We have demonstrated for the first time an integrated loop-mirror modulator (LMM) that consists of two identical 3dB couplers, which are cascaded to create an MZI, with the output waveguides connected to form a loop-mirror. The impact of the addition of the loop-mirror is a significant reduction (from 100% to only 50%) of the change in coupling ratio required to obtain complete modulation with the MZI. When no voltage is applied to the MZI arms, all the input power appears at the one arm of the loop-mirror and it is reflected toward the input. To send light to the output, the input power must be distributed equally between the upper and lower arms of the loop-mirror. This requires a smaller phase shift than in a regular MZI, where all the power should be transferred to the lower port to achieve efficient intensity modulation of the signal. This reduction of the phase shift needed to achieve complete modulation translates into a decrease of the voltage required to actuate the modulator, thereby resulting in a lower power consumption by the device. This integrated electro-optic (EO) modulator could be used as a cost-efficient and broadband reflective modulator in passive optical networks (PON) and Gigabit PON (GPON).

1.2 Original contributions

The work done in this thesis includes the following original contributions which have been submitted in the form of journal papers and published in conference papers as well as a provisional US patent. The information in brackets indicates the relevant thesis chapters.

- ✓ Analytical comparison for switching energy of resonant interferometer and non-resonant interferometer (Chapter 3): presented at the Photonics North conference and submitted for publication [8]
- ✓ The theoretical design and analysis of a novel reflective LMM (Chapter 4) which is filed for US Utility Patent Application titled "optical loop enhanced optical modulators" US Patent 20,170,293,083
- ✓ Design, analysis and experimental implementation of on-off keying (OOK) modulation (Chapters 4 and 5): presented at the IEEE Optical Interconnects Conference (OI) [9]
- ✓ Design, analysis and experimental implementation of and differential phase shift keying (DPSK) modulation (Chapter 6): presented at the IEEE Photonics Conference (IPC) and submitted for publication [10]
- ✓ The first demonstration of LMM as intensity modulator with 20 Gb/s modulation speed (Chapter 5): presented at the Asia Communications and Photonics Conference (ACP) and submitted for publication [11]
- ✓ Exhibiting potential application of the LMM as a reflective modulator in Gigabit passive optical networks (GPON) (Chapter 5): presented at the IEEE/OSA CLEO conference and submitted for publication [12]
- ✓ Low-power 20 Gb/s optical modulator with a silicon-based integrated loop-mirror (Chapters 4 and 5) submitted to IEEE Photonics Journal and it is under revision for publication. This paper is the extended version of the conference paper presented at the ACP conference listed above which includes the new analysis for EO response for intensity modulation.

- ✓ DPSK modulation with a dual-drive silicon photonics loop-mirror modulator (Chapter 6): in preparation to submit to IEEE Photonics Journal for publication. This paper is the extended version of the conference paper presented at the CLEO conference listed above which includes the new analysis for EO response for phase modulation.

1.3 Thesis organization

The remaining of the thesis is organized as follows:

- Chapter 2: This chapter is mainly devoted to the literature review and background on optical networks, optical switches and modulators. Furthermore, there are discussions on different technologies and materials that are used in optical devices. In addition, standard configurations for low-power EO switches and modulators are presented. At the end of this chapter different modulation formats and application of PON are described.
- Chapter 3: The switching energy of resonant and non-resonant EO switches is analytically compared and there is a detailed discussion on the efficiency of each configuration.
- Chapter 4: In this chapter we worked out the theoretical model of the LMM design with traveling-wave (TW) electrodes regime. The energy consumption theory in lumped electrodes regime is presented as well.
- Chapter 5: In this chapter we describe the fabrication process of LMM and report on pertinent measurement results in on-off keying (OOK) modulation. We also investigate the possibility of using integrated silicon photonic reflective modulator for PON.
- Chapter 6: This chapter presents design and measurement results of the LMM in differential phase shift keying. By showing experimental results, we conclude that the LMM is capable of arbitrary intensity and phase modulation.

- Chapter 7: This chapter includes further applications and implications of LMM and future research directions.

References

[1] M. Moore, “Tech giants and civic power,” *Cent. Study Media, Commun. Power.” King’s Coll. London*, 2016.

[2] D. Kilper, K. Bergman, V. W. S. Chan, I. Monga, G. Porter, and K. Rauschenbach, “Optical networks come of age,” *Opt. Photonics News*, vol. 25, no. 9, pp. 50–57, 2014.

[3] J. Hecht, “PHOTONIC FRONTIERS: SILICON PHOTONICS: Silicon photonics evolve to meet real-world requirements,” *Laser Focus World*. 2013.

[4] D. B. Mortimore, “Fiber loop reflectors.,” *J. Light. Technol.*, vol. 6, no. 7, pp. 1217–1224, 1988.

[5] C. A. Millar, D. Harvey, and U. Paul, “Fiber reflection Mach-Zehnder interferometer,” *Opt. Commun.*, vol. 70, no. 4, pp. 1–5, 1989.

[6] G. Dickinson, D. a Chapman, and D. a Gorham, “Properties of the fiber reflection Mach-Zehnder interferometer with identical couplers.,” *Opt. Lett.*, vol. 17, no. 17, pp. 1192–1194, 1992.

[7] K. P. Oakley, N. M. O’Sullivan, C. D. Hussey, and T. A. Birks, “Miniature high-performance fiber loop reflector,” *Electron. Lett.*, vol. 27, no. 25, 1991.

[8] F. Soltani and A. G. Kirk, “A comparison of switching energy of resonant and nonresonant electro-optic switches,” in *SPIE Photonics North*, 2012, vol. 8412, pp. 841222–841227.

[9] F. Soltani, M. Menard, and A. G. Kirk, “Optical modulator with an integrated loop mirror,” in *IEEE Optical interconnects conference (OI)*, 2015.

[10] F. Soltani, D. Patel, M. Menard, D. V. Plant, and A. G. Kirk, “Low-power DPSK modulation at 10 Gbps using a silicon photonic loop mirror modulator,” in *IEEE PhotonicsConference (IPC)*, 2016.

[11] F. Soltani, M. Menard, and A. G. Kirk, “Low-power 20Gb / s modulator with an integrated loop mirror,” in *Asia Communications and Photonics Conference (ACP)*

IEEE/OSA/SPIE sponsored, 2015.

[12] F. Soltani, M. Menard, and A. G. Kirk, “Integrated silicon photonic reflective modulator for passive optical networks,” in *IEEE/OSA CLEO conference*, 2017.

[13] Silicon Photonics – PhD course prepared within FP7 – *224312* Helios project

Chapter 2

Literature Review

2.1 Introduction

This chapter is devoted to background knowledge and literature review that is necessary for the explanation of the research project that is developed and implemented in this thesis. This chapter begins with Section 2.1 which presents the recent demands in telecom and datacom networks and the necessity to design and improve optical components, and particularly optical switches and modulators. In Section 2.2, different technologies to build optical switches and modulators are described. After summarizing the contents of Sections 2.1 and 2.2, Section 2.3 investigates different materials used in the implementation of EO switches and modulators. Since low-power modulation is the core of this research project, it is important to review the methods that are used so far to make power-efficient devices and summarize the switch characteristics. These are achieved in Section 2.4 and Section 2.5, respectively. The overview of different modulation formats is studied in Section 2.6. The research demonstrated in this project has a potential application in passive optical networks (PON) and Gigabit PON (GPON). For this reason, the applications of PON and GPON are reviewed in Section 2.7.

2.1.1 Optical networks

Light has been introduced into telecommunication networks because it can carry information with low dispersion over long distances. In addition, light's high bandwidth makes optical devices suitable for fulfilling the growing need for high capacity data transfer. In conventional optical networks, data transmitted through switching nodes are converted from optical form to electronic form (O/E conversion), buffered electronically, and converted to an optical form (E/O conversion) before being retransmitted. This process requires an optical-electronic-optical (OEO) switch. The OEO switches are necessary for routing operations and have many advantages, such as the ability to modify and restore signals and to perform wavelength conversion, data management and performance monitoring at the bit level. Their drawbacks include lack of transparency (i.e. dependency to different data rates and protocols), and high power consumption. The optical switches allow data to be transmitted and controlled without conversion to an electrical format [1]–[4]. The transfer of the switching function from electronics to optics by using optical switches leads to a reduction in the number of network equipment, an increase in switching speed that comes with an increase in network throughput, a decrease in operating power, and a decrease in the overall system cost [5]. As mentioned above, future all-photonics networks are expected to be transparent and independent of O/E conversion. However, reaching full transparency in practice is limited by the characteristics of network components [1], [2]. Therefore, improving the performance of optical networks necessitates the development of components which feature high switching speed, high modulation rates, and low-power consumption.

Wavelength division multiplexing (WDM) enables the efficient use of the huge bandwidth of optical fibers. Optical switches predate WDM, but the prospect of routing entire wavelength channels all-optically creates a demand for new types of switches. In the literature, scalability is defined as a characteristic of a system that has the capability to cope and perform under an increased workload. A system that scales well will be able to maintain or even increase its level of performance when it encounters larger operational demands [2], [6]. WDM brings several advantages to optical networks such as: huge information-carrying capacity, reconfigurability, the flexibility of design and operation, cost-effectiveness, and scalability [1], [7]. In addition, dense WDM (DWDM) is applied to optical networks to achieve increased data capacity even higher than WDM. DWDM uses smaller channel spacing than WDM and, like the WDM configuration, it has a wavelength multiplexer at the transmitter to combine independently modulated optical channels of different wavelengths into a single fiber and a corresponding demultiplexer at the receiver. An important application of DWDM is in transatlantic cables. These cables contain four fiber pairs, with each fiber supporting 48 DWDM channels. If the data rate in each channel is 10 Gb/s, then 4 x 48 x 10 Gb/S = 1.9 Tb/s data are transmitted in the cables [2], [6].

Optical networks can be classified into different categories based on their ability to reconfigure and rearrange the setting of elements [1], [6]. In this review we focus on the two most common and commercially available types of optical networks. The first is static networks (Figure 1), which have fixed structure and use OEO switching for data transmission purposes. The second is circuit switched networks (Figure 2), in which wavelength connections are established between nodes before they begin exchanging information [2]. The following sections will include discussions about optical switching techniques as well as optical modulators. Due to their efficient characteristics, the circuit switched networks are the leading network architecture for the future optical communications.

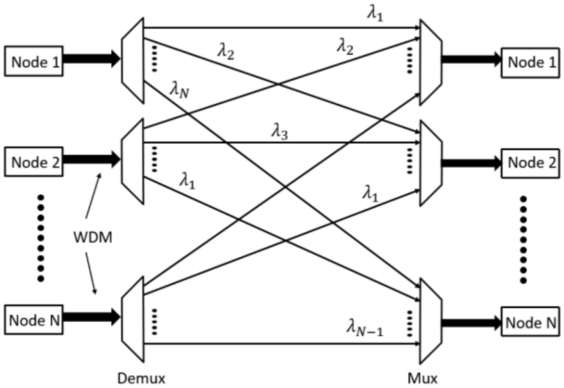

Figure 1 - Fixed (static) network (redrawn from [1]**)**

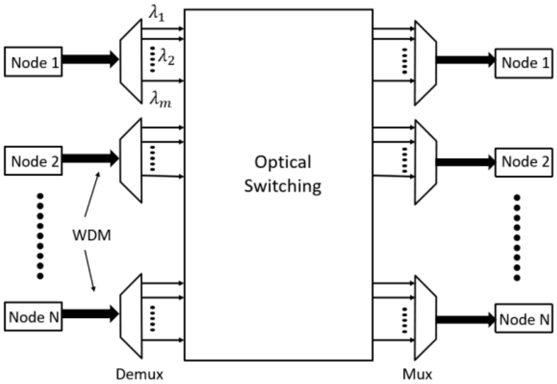

Figure 2 - Circuit switched (dynamic) network (redrawn from [1]**)**

2.1.2 Optical switches

Optical signals are passing from multiple inputs to multiple outputs through optical switches. These switches can be classified into different domains as space, time, and wavelength. This review is about optical space switches and their applications [1]. The technologies to manage optical space switching can be categorized based on the physical effects responsible for the switching process. These technologies and some of the materials used to implement them are listed below [1], [6], [7]:

- The optomechanical switches are developed based on the concepts of free space optics. The micro-electro-mechanical-systems (MEMS) switches have been fabricated by placing alternate layers of different optical materials. These switches will be explained in Section 2.2.1.
- The thermo-optical (TO) switches are developed based on the thermally induced change of refractive index of optical materials. They have been fabricated mainly from silica and polymers. These switches will be explained in Section 2.2.2.
- The EO switches are developed based on the electrically induced change of refractive index of optical materials. They can be fabricated from $\mathrm{LiNbO_3}$, liquid crystal, and III-V semiconductors. EO switches have recently been considered as a suitable option for next generation of optical space switches. These switches will be explained in Section 2.2.3.

Due to the complexity of optical-electrical circuit blocks, their performance improvement requires simultaneous verification of several parameters in optical component designs. Some of the design parameters are mode size, fiber interface, integrated actuation, central system complexity, switching speed, and quantity of switching elements as a function of the port count. Although several industry-specific standards exist for optical component product verification, there is no universal industry standard. In a practical sense, it can happen that one design variable limits the optimization of another for a specific application. One of the major challenges in the development of efficient optical designs is to reach a balance between cost and functionality of different verified parameters in optical links.

2.1.3 Optical modulators

Optical modulators have a significant role in transferring data in the telecommunication and datacom networks [8]. An optical modulator is part of an optical link to convert electrical data into an optical format with efficient performance. Board-level applications with complementary-metal-oxide-semiconductor (CMOS) compatibility require low-power components. That is one of the motivations for many researchers to work on lowering the power consumption of modulators as the core operating on-chip devices [9]–[12]. In addition to optical interconnects, such low-power modulators will also be applicable in high bandwidth fiber and wireless communication devices, video transmission and radio frequency distribution, ultrafast analog to digital converter, optical detection and radar systems [13].

2.2 Different technologies to fabricate optical switches and modulators

In this section the three main technologies to implement optical switches and modulators will be discussed. Taking the advantage of each technique or even the combination of different techniques, make it possible to develop desired optical switches and modulators for efficient optical links. These technologies are included here: MEMS technology (Section 2.2.1), TO technology (Section 2.2.2), EO technology (Section 2.2.3).

2.2.1 Micro-electro-mechanical systems technology

One of the main applications of the optical switching is in optical cross-connects (OXC), which are the elementary constituents for routing optical signals. Micro-electro-mechanical systems (MEMS) technology plays an important role in optical space switching [1]. It brings many of the advantages of macroscopic optomechanical switches and extends functional features of optical links by adding movable mirrors and shutters [14]. In general, free space beam steering switches are based on the deflection of beams from an input port to the desired output ports. This involves displacement and angular changes in positions of optical elements. The total traverse path length of the beam may change depending on the location of the input and output ports and the angle of incidence of the beam on a deflector. This affects insertion loss, which must be as low as possible. In most optical systems, there will be some limiting apertures which contribute to the beam propagation loss. In MEMS switches the limiting apertures are often the micromirrors. This is because typically the smaller MEMS mirror has better functionality and it allows the mirrors to be tightly packed to achieve a small system size with a large number of ports [15].

MEMS switches are based on the deflection of light via the movement of mechanical elements. Some of the MEMS switches use tiny reflective surfaces to redirect light beams to the desired port by either bouncing the light off neighboring reflective surfaces to a port or steering the light beam directly to the port [5]. Types of MEMS switches include: movable micromirrors [16] (compatible with integrated Fabry-Perot (FP) optical space switches), switchable diffraction gratings [17], movable prisms [18], and displaced optical fibers [19]. Actuation mechanisms include: piezoelectric, electromagnetic, electrothermal and electrostatic (the most widely used). Electrostatic actuators have many advantages for MEMS switches: 1) they can be applied to large port count switches; 2) they have low-power dissipation; 3) electrostatic fields are easily shielded with materials used in MEMS fabrication. Most MEMS switches have response times between 10 μs to 10 ms [1], [2], [20]–[22].

In MEMs, the $N \times N$ switches are expected to be capable of interconnecting N input fibers with N output fibers in any desired combination. Two general MEMS methods for building $N \times N$ switches are available [23]. The first method is to use mirrors as individual binary switching elements that are capable of being in one of only two discrete states. In this case, the complexity of the system that is the total number of switching elements is proportional to N^2. This is commonly referred to as a digital architecture since the mirrors have binary states. Digital architectures are more attractive for small switches ($N \leq 32$). They are mostly used in 2D-MEMS architectures as shown in Figure 3a. In the second method, which is known as beam steering or analog architecture, each element is capable of being in at least N distinct states, and then the total number of switching elements required is $2N$. In this approach, each mirror acts as a $1 \times N$ switch, where two sets of such $1 \times N$ switches are interconnected in free space. Reducing the number of switching elements enables the system to scale to much larger port counts than possible with digital mirrors. The analog architecture method is implemented in 3D-MEMS designs as shown in Figure 3b. A drawback of this method is that an expensive and complex feedback system is needed for stabilization of the insertion loss [5]. Factors that may limit scalability are beam diffraction and the mirror tilt angle which requires precise control within 0.1 degrees [2].

There is often some confusion about how the switching system scales, depending on whether it is based on digital/analog mirrors and planar/volume configurations [24]. This is because planar systems are usually made of digital mirrors and 3D (volume) systems are usually made of analog mirrors. Indeed, both digital and analog architectures can be implemented in a planar configuration (2D-MEMS). Taking into consideration the effects of beam diffraction, the physical dimensions of a planar switch scales with N^2 whether it is made of digital or analog mirrors. For volume configuration (3D-MEMS), only analog beam steering has been implemented. However, the physical size of a 3D switch scales proportional to N whether it is based on digital or analog mirrors. Moreover, the MEMS switches with waveguides can provide extremely low-less propagation with high ER in several hundred ports. The waveguide loss can be optimized by improvements in the waveguide dimensions and crossing design [123].

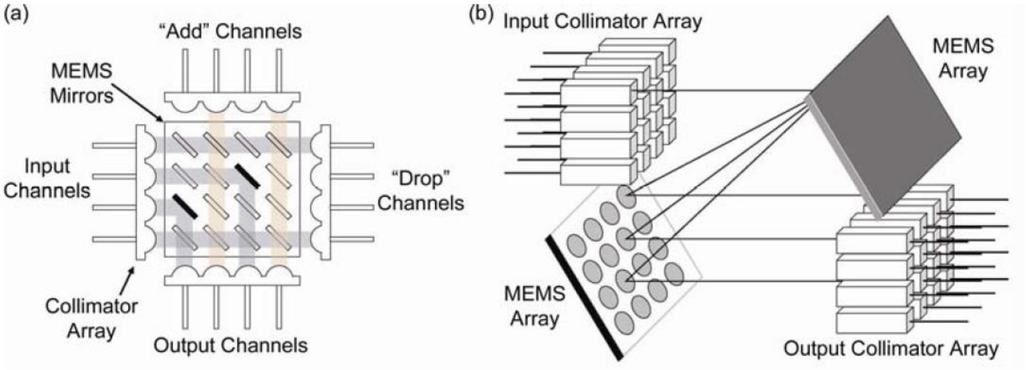

Figure 3 - Typical layout for (a-left) 2D and (b-right) 3D MEMS switches using micromirrors (permission received to use from [2])

2.2.2 Thermo-optical technology

Thermo-optical (TO) switches are regularly fabricated by using polymers, silica and silicon-on-insulator materials. A temperature variation causes a change in the material refractive index. For example, temperature variations will shift the resonant frequency of silica-based switches; the chromatic dispersion of silica-based switches is associated with this shift. In polymers, the density decreases due to thermal expansion, and this modifies the refractive index of the material.

In TO switches, the switching speed and the power efficiency are correlated. The speed of the switch is limited by the rate of generated and dissipated heat. A switch requiring less power can be obtained with materials that have a low thermal conductivity. They can absorb heat more efficiently, but they also have slower switching speeds. Moreover, heating in TO switches is achieved with electrical micro-heaters; therefore, switching times are limited by the speed of the electrical-thermal conversion and by the diffusion time [2].

Polymers have large thermo-optical coefficients and the largest index modulation of TO material platforms. They have a relatively low material and fabrication cost, and can easily be deposited as thin films on glass or silicon substrates. They also have low propagation loss (less than 0.1 dB/cm at 1550 nm), so they have very small insertion loss. However, the drawback of using polymers in TO switches is their low thermal conductivity in comparison to the thermal conductivity of silica – the latter is ten times larger than the former. The propagation loss in silica is lower than polymer waveguides (less than 0.01 dB/cm at 1550 nm), but the TO coefficient of silica is lower than that of polymers (by an order of magnitude). For their part, SOI materials have a high index contrast that can be used to make sharp waveguide bends and can be used in compact devices. The TO coefficient of SOI materials is the same as the TO coefficient of polymers but their thermal conductivity is 100 times higher than the thermal conductivity of silica. This means SOI materials can be used to fabricate switches with sub-microsecond switching time. The coupling and propagation loss of SOI materials is higher than those of silica and polymer materials [2]. Table 1 compares the properties and characterizations of silica, polymer and SOI.

The majority of TO switches are channel waveguide devices that can be classified as a digital optical switch (DOS) or MZI. DOS is a Y-junction with heaters on each branch, one input and two outputs. Micro-heaters are placed on each output path. The angle between output paths is 0.1 - 0.15 degrees, creating a switch that is in the order of millimeters long. Switching is controlled by increasing the refractive index of the desired output waveguide on the Y-junction. DOS is usually fabricated from polymers because their required refractive index difference is relatively large. Another advantage of DOS is that the digital response does not require precise control of the temperature; they are wavelength and polarization-independent devices. However, their scalability is limited by the DOS length.

Table 1- Characterization and properties of TO switches

	Silica	**Polymer**	**SOI**
TO coefficient	Less than polymer (an order of magnitude)	Large	The same as polymers
Thermal conductivity	Ten times larger than polymers	Polymer < Silica < SOI	100 times larger than silica
Wavelength	1550 nm	1550 nm	1550 nm
Propagation loss	< 0.01 dB/cm	< 0.1 dB/cm	high
Fabrication	Flame hydrolysis deposition/chemical vapor deposition	Deposited on thin films, glass or silicon substrates	Fabricated using e-beam lithography and Reactive Ion Etching(RIE) plasma etching [25]
Optical components and devices	Planar Lightwave Circuits (PLC)	Digital Optical Switch (DOS)	Sharp Waveguide bends / Compact devices / Mach-Zehnder interferometer (MZI) / Mostly Used in the Optical waveguide and resistive electrodes

In contrast, MZI has two 3dB couplers that can be directional couplers or multimode interferometers (MMI)s. There is a phase shifting region composed of two decoupled waveguides (Figure 4). Switching is achieved by controlling the phase difference between the two signals in the phase shifting region by modulating the refractive index of the waveguides. Depending on the phase difference, constructive interference will occur in one of the two outputs of the waveguide. MZI requires a smaller refractive index change than DOS and is mostly used in silica waveguides. MZI devices have lower power consumption when fabricated from polymer rather than other materials. As a trade-off, MZI is very sensitive to temperature changes and is hard to control. It is also a wavelength and polarization dependent structure [2], [6], [7], [26], [27].

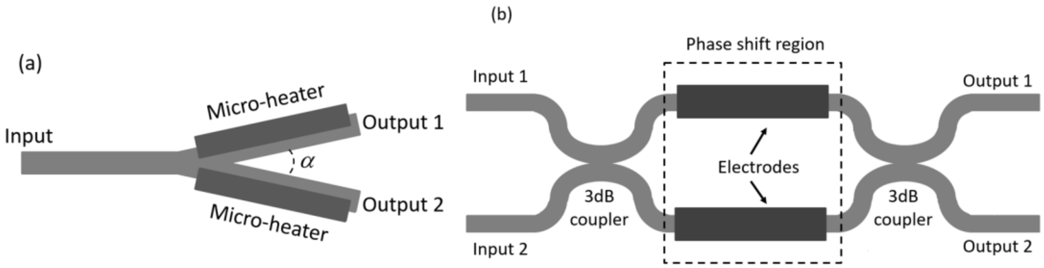

Figure 4 - Schematic diagrams of the most common TO switch configurations: (a) digital optical switch and (b) MZI switch (redrawn from [2]**)**

2.2.3 Electro-optic technology

The structure of an electro-optic (EO) switch (Figure 5) consists of two waveguides that are cascaded to make a directional coupler (DC). The voltage that is applied to DC changes the refractive index of the waveguides and causes a phase shift. In the waveguide path, the refractive index change will direct light to the desired output port (functioning as an optical switch). Changing the applied electric field of EO modulators has a considerable effect on the functionality of these modulators [21].

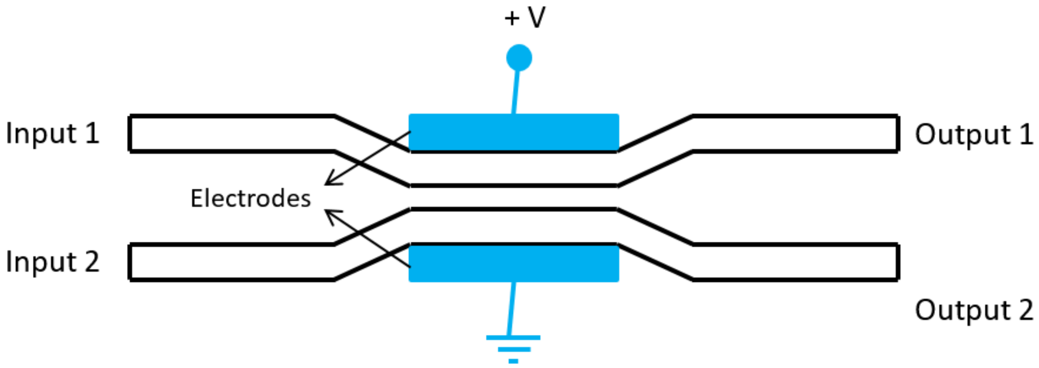

Figure 5 – Conventional EO directional coupler switch

The EO effect can be observed when an electric field is applied to a non-centrosymmetric crystal or to an EO polymer combined with chromophores. The application of an electric field redistributes the bound charges and deforms the ion lattice in the direction of the electric field; consequently, the refractive index changes.

The EO effect in Equation (1) has a linear term expressing the refractive index change as proportional to the electric field strength (Pockels effect). The EO effect is anisotropic and the induced change in refractive index is related to the direction of the applied field (polarization) and the crystal lattice shape or permanent dipoles. The modulation of the effective refractive index in an EO device is obtained from an electric field applied in a specific direction; it couples with one of the EO coefficients of the material. The EO effect can be expressed as:

$$\Delta n = \frac{1}{2} n^3 r E \tag{1}$$

where n is the refractive index, r is the Pockels coefficient (i.e. linear EO coefficient), and E is the applied electric field. Typical characteristics of EO materials can be listed as the following: 1) linear EO coefficients in most active materials are in the order of tens of pm/v; 2) the maximum change of the refractive index is estimated as 10^{-3} that is an order of magnitude less than the TO effect; 3) the switching time is very fast and is in the order of nanosecond or less (typically limited by the RC time constant of the electrodes).

Among the variety of methods that have been suggested in [28] to utilize EO effect in optical modulation based structures, we will need the plasma dispersion method. We will use this method in Chapters 4-6 to design and characterize a loop-mirror modulator. In this method the concentration of free charges in silicon changes the real (Δn) and imaginary ($\Delta \alpha$) parts of the refractive index. Consequently, optical modulators can be classified based on change in Δn as electro-refractive modulator or change in $\Delta \alpha$ as elecan tro-absorptive modulator. Recently fabricated high-speed Si-based waveguide-structured modulators operate by using plasma dispersion effect [11], [12], [29]–[33] attract huge attention.

There are three main configurations that are used to structure the free-carrier concentration in plasma-dispersion-based silicon optical modulators which are identified as: carrier accumulation, carrier injection, and carrier depletion. In the carrier accumulation configuration, a thin layer of insulator is placed between the two sides of PN junction (i.e. PIN diode) in the waveguide to form a capacitor to control the injection of free carriers into the path of the propagating light. In the carrier injection configuration, an intrinsic region is placed between the two highly doped sides of PN junction (i.e. PN diode) in the waveguide to minimize the modal overlap. In this method, a forward bias voltage is applied to the waveguide and the free electrons and holes are injected into the intrinsic region resulting in the injection of large currents at a small voltage. Thus, only a short length of the waveguide is needed to achieve the expected phase shift, and consequently high junction capacitance of the forward bias diodes leads to a fast switching speed. In the carrier depletion configuration, the PN junction is similar to the carrier injection configuration, but the sides of PN junction are lightly doped. In this method, a reverse bias voltage is applied to the waveguide and the intrinsic region becomes larger that causes a small leakage current. In comparison to the forward-biased diodes, the PN diodes that are operating in the reverse bias voltage are made with a longer waveguide and require a larger bias voltage to generate the expected phase shift at faster switching speeds.

2.3 Different materials to fabricate EO switches and modulators

Optical networks play a fundamental role as main carriers of information and are growing in importance largely because of their increasing presence in fiber to the home (FTTH) links. The desire to use the enormous potential bandwidth offered by optical carrier frequencies is the motivation to achieve power-efficient and high-speed modulators. Researchers are considering different optical materials to fabricate modulators with low-loss, large bandwidth, low drive power and small device geometries [34]. In the effort to design compact modulators, waveguide modulators are primarily investigated because of their compatibility with fibers and their capability to reach the goal of small footprint optical components. On some specific optical material substrates, waveguide modulators offer the potential for monolithic integration with sources and electrical driver circuitry.

This section describes EO properties of different optical materials and discusses the possibilities of utilizing these materials for implementing EO waveguide modulators. The most widely used EO materials are $\mathrm{LiNbO_3}$, compound semiconductors ($\mathrm{III-V}$ materials such as Indium Phosphide (InP)) and ferroelectric crystals, polymers, and silicon. The characteristics of these EO materials are explained in detail in the following subsections.

2.3.1 Lithium Niobate

Lithium Niobate ($\mathrm{LiNbO_3}$) is the most widely used crystalline material in the commercial manufacturing of EO devices. External $\mathrm{LiNbO_3}$ modulators are used in optical transmission devices and systems because they have efficient extinction ratio, insertion loss, chirp feature and optical transparency [35]. $\mathrm{LiNbO_3}$ has a high EO coefficient ($\mathrm{r_{33} = 32.6\,pm/v}$), but it has some drawbacks that limit its use. For example, it requires large bending radii that result in a large device footprint. Careful electrode fabrication is required to avoid voltage drifts and pyroelectric effects. $\mathrm{LiNbO_3}$ based modulators need to improve their integration capability and fabrication costs. By using micro-structuring techniques, such as etching, domain insertion and thin film processing, state-of-the-art $\mathrm{LiNbO_3}$ based integrated EO modulators are expected to give rise to new configurations. These proposed fabrication techniques facilitate the development of small form factor optical modulators and lead to a higher density of optical components in the telecommunication links.

2.3.2 Indium Phosphide

MZM based on Indium Phosphide (InP) exhibit high 3dB bandwidth [36] and low driving voltage [37]. Furthermore, InP can potentially be integrated with a wide range of components, such as lasers, semiconductor optical amplifiers (SOA)s, photodetectors, passive optical circuits, and even electronic drivers [38], [39]. For semiconductor-based modulators (e.g. InP or GaAs), the optical refractive index is usually bigger than microwave refractive index ($n_{opt} > n_{\mu}$). This helps to develop state-of-the-art TW modulators with high modulation bandwidth. Moreover, the telecommunications market is interested in TW modulators with low insertion loss. Therefore, the MZMs must compete with low-loss modulator architectures that are based on $\mathrm{LiNbO_3}$ or polymers. The fiber-chip coupling loss, material absorption loss and scattering loss at the optical waveguide sidewalls can be reduced by an optimized design. In recent years, InP-based modulators have shown lower loss in comparison to the $\mathrm{LiNbO_3}$ based modulators [39]. The EO coefficient of compound semiconductors is smaller than the EO coefficient of $\mathrm{LiNbO_3}$. The high refractive index of compound semiconductors compensates for their low EO coefficient. Moreover, they can have a relatively high modification of the refractive index when an electric field is applied [1], [2], [6], [7].

2.3.3 Optical modulators based on polymers

Recently improved EO polymers have higher speed, wider bandwidth, and lower drive voltage V_{π} [40], [41] than the EO materials described earlier. The EO coefficient of polymers is larger than that of $\mathrm{LiNbO_3}$. However, they have limited availability and, unlike TO polymers, stability is an issue (because the relaxation of the dipoles occurs after polling). These properties increase their potential to provide applications in high bandwidth communication devices, video transmission and radio frequency distribution, ultrafast information processing A to D, optical detection and radar systems [13], [42]–[46]. It is possible to integrate polymeric EO materials with very-large-scale integration (VLSI) semiconductor electric circuits or with passive optical circuitry [13]. EO polymers can either be deposited onto or adhere to semiconductor substrates. This is a significant step toward the development of integrated opto-electronic chips [43], [47]–[49].

In an integrated EO polymer circuit with a top layer of active polymer materials and a lower layer of polymer materials, which contains optical waveguides, light can be coupled from one layer to the other. EO polymer devices require drive voltages less than one volt, while $\mathrm{LiNbO_3}$ modulators typically require a drive voltage in the order of volts. By adjusting the chromophore/polymer design, drive voltages lower than 0.1 volts have been reported [13], [50]. Furthermore, improved EO polymer materials display very low chromatic dispersion [42].

The operational and temperature stability of polymeric devices is very competitive with devices fabricated from $\mathrm{LiNbO_3}$ and GaAs [13], [50]. In comparison to the crystalline materials, EO polymers have higher EO coefficient $\mathrm{r_{33}}$ for dense device arrays. EO polymers have lower relative permittivity than $\mathrm{LiNbO_3}$. As a result, several individual high-speed modulators can be packaged close to each other without having crosstalk issues between them. This supports the preference to develop polymer-based compact multichannel optical communication links [13].

Relatively large transmission areas and complex integrated optical circuits and devices can be built at relatively low-cost using the polymer technology. One of the advantages of the optical polymer technology is the ability to use different types of polymers within the same integrated optical circuit to perform specific functions. For instance, EO polymers used in light amplifying polymers and low-loss polymers can build low-loss interconnections with 0.1 dB/cm loss at 1310 nm. Polymers specially designed for high EO coefficients inevitably have a higher loss.

It is very difficult or sometimes impossible to achieve both very low-loss and very high EO coefficients in the same design and material [10], [13], [50]. EO polymers used in optical communication devices have been categorized into two main applications: either high-speed devices or low-loss devices [45]. The properties of each application are summarized in Table 2. Single mode operation is required for photonic applications of EO polymer devices and for controlling the refractive indices of the core and cladding materials in waveguides. The width and thickness of the guiding layer and the etching depth should be optimized in the design and fabrication of these devices.

Table 2 - Application of EO polymers [45]

	High-speed (and broad bandwidth) devices	**Low-loss devices**
Polymer type	Nonlinear optical polymer (NLO)	Low-loss optical polymer
Applicable devices	1) EO Mach-Zehnder modulator (MZM) 2) EO 2x2 switches 3) Polarization controller 4) Second harmonic generators 5) Optical frequency converter 6) Photonic sensors	1) DOS 1x2 , 2x2 , 4-arrayed 2x2 2) 16 x 16 arrayed waveguide grating (AWG) routing 3) Tunable Bragg wavelength filters 4) Variable optical attenuators (VOA) 5) AWG multiplexer/demultiplexer
Optical system applications	Increase the channel bitrate for time division multiplexing (TDM)	Coupled to the WDM based applications
Implemented materials and significant applications	Mainly implemented in $\mathrm{LiNbO_3}$ and applicable to compound semiconductor devices	Mainly implemented in Silica and applicable in planar lightwave circuits (PLC)
Using polymer characteristics	Low dielectric constant – Low optical dispersion – Fast electronic response (low frequency to optical frequency)	Ease of device fabrication – Flexibility of device structure – Low-loss polymer- Large TO coefficient – Easy controllability of the refractive index

Table 3 provides a summary of the performances of some EO polymer switches in comparison to the DOS [45] in which EO polymers are used to change the refractive index of the structure. EO switches show lower polarization dependency and they are power-efficient devices. In contrast to EO switches, DOS switches that are implemented in TO technology require lower driving voltage and the insertion loss is very small.

Table 3 - Performance of Polymer-Based Devices [45]

	EO 2×2 Switch	**1×2 DOS**	**2×2 DOS**	**4-arrayed 2×2 DOS**
Operation wavelength (µm)	1.3	1.520-1.560	1.520-1.560	1.520-1.560
Cross talk (dB)	cross arm: –18.1 straight arm: –18.5	< 25	< 30	< – 30 ± 2
Operating voltage (V)	8.5	~ 3-5	~ 6-10	~ 7–10 [51]
Total insertion loss (dB)	~5	< 2.5	< 3.5	3.5 to 4.0
Polarization dependent loss (PDL) (dB)	~0.02 - 0.2	<0.2	< 0.3	~ 0.2 – 0.7
Switching time (ms)	~ 4 x 10^{-6}[52]	< 3	< 3	The falling and rising times were <5
Operation electrical power (mW)	~ 3.1[52]	< 100	< 300	250

2.3.4 Optical modulators based on silicon

Optical components fabricated in integrated silicon (Si) photonics are applicable in optical telecommunications and in optical interconnects [53]. Silicon is capable to overcome the limitation of global metallic connections that brings the advantage for optical interconnects in data centers and on-chip implementations. Since Si exhibits compatibility with existing CMOS technology and SOI substrates are widely used in microelectronics, it introduces a route toward developing combined photonics and electronic technologies [54] to provide efficient, reliable and low-cost optical devices. There are several physical effects to consider in the optical modulation in silicon [55]. For example, strained silicon is used for linear EO operation [56], bulk silicon-germanium provides electro-absorption [57], SiGe/Ge quantum-well waveguide modulators provide the quantum-confined Stark effect [58], and free-carrier concentration is used for refractive index variations [59]–[65]. The high-speed modulators integrated into the silicon waveguides are based on carrier accumulation in metal-oxide-semiconductor (MOS) capacitors and plasma dispersion effect in PN or PIN diodes [61], [62], [66].

2.3.5 Summary and comparison of different electro-optic materials

Table 4 summarizes the properties and characteristics of the various EO materials that were discussed in Sections 2.3.1 – 2.3.4.

Table 4 - Properties of EO Materials

	$\mathbf{LiNbO_3}$	**Polymer**	**Compound semiconductors ($\mathbf{III-V}$ materials)**
EO coefficient	High r_{33}=32.6 pm/v	Bigger than $\mathrm{LiNbO_3}$	Lower than $\mathrm{LiNbO_3}$
Fabrication process	Titanium diffusion, proton exchange	UV photolithography	Add PIN structure in reverse bias to modify the refractive index
Highlights and advantages	Invert domains by electrical poling to maximize refractive index contrast, Linear EO effect	Linear EO effect	High refractive index so Δn is high
Comments	Careful electrodes fabrication is required to avoid voltage drifts and pyroelectric effects	Unlike TO polymers stability is an issue with EO polymers, as is limited availability	Used to fabricated EO optical modulators

Since the scope of this thesis is about silicon-based switches and modulators, Section 2.4 is dedicated to the characteristics of silicon-based optical components and its place in the other optical materials.

2.4 Different methods to fabricate low-power optical switches and modulators

To satisfy the demand for wide bandwidth and high capacity in optical networks, massive numbers of parallel optical links are required in high-performance computing systems and data centers. These links are used to connect racks, boards, modules, and chips that must provide reliable communication while maintaining extremely low-power dissipation. The desired power efficiency should be in the order of pico-Joules and femto-Joules per transmitted bit, while the expected cost should be less than a few cents per Gbps [67]–[69]. It is statistically observed that in the current optical networks the capacity growth rate is much faster than the energy efficiency scaling. This causes increasing power density by 20% per year [70].

In Section 2.3.4 the integrated silicon photonics is proposed as a promising solution to adopt the emerging large-volume market needs for deployment of high-speed, low-power and cost-effective optical interconnects [71]. Furthermore, silicon has an advantageous price volume curve [72] and demonstrates efficient optical properties in the near infrared region. Hybrid integration, which takes full advantage of both electrical interconnects (i.e. CMOS circuits) and optical interconnects, has the potential to lead to a major breakthrough in the development of optical devices which meet the future network demands [69]. Today, the hybrid CMOS-integrated silicon nanophotonics technology is employed in distances spanning from just a meter to about 10km.

The silicon-based optical modulator is a fundamental component in optical interconnects which is desirable due to its resilience when one needs to change different characterization parameters, such as modulation speed and depth, optical bandwidth, insertion loss, footprint, and power consumption. In the characterization of optical modulators, the power consumption parameter (i.e. the energy expended in producing each bit of data) has a very significant importance. As argued in the literature [68], the optical interconnects can only be accepted for on-chip applications if their power consumption is lower than the present electrical interconnects [73]. The power efficiency is an extremely demanding target for future optoelectronic devices and systems. Optical modulators are categorized into amplitude, phase or polarization modulators. In this section we focus on amplitude modulation. Phase modulation will be discussed in Section 2.6.2 and Chapter 6.

As was discussed in Section 2.3, optical devices based on the EO effect have the potential to provide higher modulation efficiency compared to the other physical effects [74]. The mechanism of energy consumption in the optical modulators involves charging and discharging of the PN junction. As discussed in [75], if the applied reverse bias voltage or small forward bias voltage is sufficiently high so that one can ignore the relatively small forward current effect in an optical modulator, then the minimum total power consumption of the device (considering optical plus net electrical) can be estimated as one-quarter of PN junction capacitance multiplied by square of the drive voltage to the modulator.

There are two methods for converting a change in refractive index into intensity modulation. The first method, employed in a non-resonant interferometer (such as an MZI), uses the change of refractive index to modify the phase shift between propagating waves. Due to insertion loss values and their footprint, the MZI-based devices are attractive in long-haul applications. The second method, employed in a resonant interferometer (such as a microring resonator), reshapes the resonance conditions [76]. The devices that are based on micro-rings are used in photonic integrated circuits (PIC) in SOI technology. They have a potential for high-density integration at the expense of enormous temperature sensitivity. Table 5 presents the performances of optical configurations that are based on the EO effect and plasma dispersion methods [29], including reversed-biased and forward-biased MZI, reverse-biased and forward-biased ring.

Note that the maximum speed achieved by the devices described above is measured at their maximum non-return-to-zero (NRZ) modulation rate. MZM has a large footprint, a power consumption in the order of $5\mathrm{pJ}$ per bit, and $\mathrm{V_{pp}}$ values as large as $6.5\ \mathrm{V}$. A long phase-shifter is used to get lower drive voltage for an MZM. The performance of an MZM is determined by its speed, insertion loss, and V_{π}, which is usually a trade-off between speed and insertion loss [12].

The microring-based modulators have high confinement of light, and their power consumption is considerably lower compared to the non-resonant modulators. The modulation rate of the microring modulator is limited by the photon lifetime in the resonance cavity. The main issue in using ring modulators in integrated devices is their narrow bandwidth, as this means that they need precise resonance tuning. Furthermore, they are particularly sensitive to fabrication errors, which cause a shift in their resonant wavelength. The four parameters that characterize the performance of microcavity modulators are: drive voltage, insertion loss/extinction ratio, speed and energy consumption [12]. The power consumption of microring modulators strongly depends on their dimensions and, consequently, on the device capacitance. For instance, in a microring optical modulator, decreasing the radius by a few μm reduces the device capacitance by tens of fF [12] and consequently, the output impedance is elevated and the power consumption is reduced.

Table 5 – Comparison of configurations based on plasma dispersion method [29]

	Reverse bias MZM				**Forward bias MZM**	**Forward bias ring**	**Reverse bias ring**				
$\mathbf{V_{pp}}$ to achieve full modulation ($\mathbf{V}$)	6.5	6.5	6.0	3.5	2.3 (after pre-emphasis)	3.5 (after pre-emphasis)	2.0	3.5	1.0	1.0	0.5
Modulation speed (Gb/s)	30	40	30	30	25	> 12.5	10	10	12.5	25	10
Power consumption ($\frac{\mathbf{pJ}}{\mathbf{bit}}$)	N/A	5.3	N/A	N/A	N/A	0.3	0.05	0.085	0.010	0.007	0.003
Tuning efficiency (nm/mW)	N/A	N/A	N/A	N/A	N/A	N/A	N/A	N/A	N/A	0.19	N/A
Modulation depth – ER (dB)	> 20	~ 25	7.2	8.5	4.5	> 10	6.5	8.0	8.0	5.0	5.0
Insertion loss ($\mathbf{dB}$)	~7	15	5.0	9.0	7.9	< 0.5	2	1.5	4.0	6.0	3.0
References	[77]	[30]	[31]	[32]	[78]	[61], [79], [80]	[29]	[11]	[33]	[81]	[82]

2.5 Summary of switch characteristics

Table 6 provides a brief comparison of different types of optical switch techniques and their characteristics. MEMS switches are the most scalable, and they have low insertion loss, crosstalk and polarization dependent loss (PDL). EO switches also have very good performance that is applicable to high-speed and low-power demands. However, to design any specific optical component, different parameters such as the geometry of the device and specific optical material must be optimized. These parameters can affect each other in the efficacy of their performance. Currently the available fast switches either have excessive loss and crosstalk, or polarization dependent. This brings up the need to develop novel switching designs. The EO switch configurations can be implemented in bulk or planar waveguides, prism deflectors [83], [84], Bragg-diffraction switches [85], [86], phase arrays [87], [88], and horn-shaped [89] and parabolic electrodes [90]. However, the linear EO effect is mostly employed in polymers and $\mathrm{LiNbO_3}$, and the current injection phenomenon is mostly used in InP and SOI-based devices [1], [2], [6], [7].

Table 6 - Comparison of different technologies in optical switching

	Optical MEMS	**TO PLC**	**EO**
Switching Time	3D: ~10 ms 2D: ~3 ms	DOS~ 1.0 ms MZI~ 0.7-2.0 ms	Prism < 1 µs Phase Array~20 ns MZI~200 ps DOS: N/A
Scalability	64x64, 1000x1000, 1100x1100 for 3D 8x8, 16x16 for 2D	DOS:8x8, 16x16 MZI:8x8, 32x32	Prism:8x8 Phase Array:64x64 MZI:4x4, 8x8 DOS: 4x4, 8x8
Potential Applications	OCS, OBS, OXC, OADM	OCS, OBS, OXC, OADM	OXC, OADM, OSM
Level of Transparency	Strict	Strict	N/A
Crosstalk (dB)	2D < -50 3D < -60	DOS < -30 MZI < -43	Prism: N/A Phase Array < -25 MZI < -15 DOS < -13
PDL Loss (dB)	2D < 0.5 3D < 0.1	DOS < 0.5 MZI~ 0.3	Prism: small Phase Array: Pol. Dep. MZI: < 1.0 DOS: Pol. Indep.
Scheme	Use tiny reflective surfaces	Temperature control to change the index of refraction	Dielectric
Strengths	Size, scalability	Integration wafer-level manufacturability	Speed
Weaknesses	Packaging, Reliability	Optical performance, power consumption, speed, scalability	High insertion loss, polarization, scalability, expensive
Insertion Loss (dB)	2D ~ 3.1-5.0 3D ~ 1.9-2.1	DOS: 6.0-10.7 MZI: 5.1-6.6	Prism: 15.0 Phase Array: 14.5 MZI: 5.0-11.4 DOS: 8.0-15.0
Ref.	[2], [4], [91]–[93]	[2], [4], [94]–[99]	[2], [4], [84], [100]–[106]

2.6 Modulation formats

Two fundamental modulation formats, on-off keying (OOK) and differential phase shift keying (DPSK), are considered in this thesis. The OOK and DPSK modulation formats will appear in verifying the functionality of the LMM as an intensity modulator (Chapter 4 and 5), and a phase modulator (Chapter 6) respectively.

2.6.1 On-off keying

In on-off keying (OOK) modulation, signals are coded and processed as binary digital signals. Binary encoding can be performed by representing a logical zero as a low-voltage signal and a one as a high voltage signal. This encoding is known as OOK. In an NRZ encoding, the signal is maintained at one or zero levels for the whole duration of a clock cycle [107].

2.6.2 Differential phase shift keying

In differential phase shift keying (DPSK), optical power appears in each bit slot, with the binary data encoded as either zero or π optical phase shift between adjacent bits. The optical power in each bit can occupy the entire bit slot (NRZ-DPSK) or can appear as an optical pulse (RZ-DPSK). The most obvious benefit of DPSK compared to OOK is the $\sim 3\mathrm{dB}$ lower optical signal-to-noise ratio (OSNR) required to reach a better bit error rate (BER) [108]. For example, at a BER of 10^{-9} , the quantum limit for an optically pre-amplified receiver is 38 photons/bit for OOK signals [109]–[111], but only 20 photons/bit for DPSK signals using balanced detection [110]–[112]. Intuitively, this can be understood by comparing the signal constellations for DPSK and OOK. For the same average optical power, the symbol distance in DPSK (expressed for the optical field) is increased by $\sqrt{2}$. Therefore, only half the average optical power should be needed for DPSK compared to OOK to achieve the same symbol distance.

Note, however, that this benefit of DPSK can only be extracted using balanced detection. The lower OSNR requirement of DPSK can be used to extend transmission distance, reduce optical power requirements, or relax component specifications. Numerical simulations and experiments have shown DPSK to be more resilient than OOK to some nonlinear effects because: 1) the optical power is more evenly distributed than in OOK (power is present in every bit slot for DPSK, reducing bit-pattern-dependent nonlinear effects); and 2) the optical peak power is 3dB lower for DPSK than for OOK for the same average optical power. Finally, an extension to differential quadrature phase shift keying (DQPSK) and other multilevel formats should enable higher spectral efficiency and greater tolerance to chromatic- and polarization-mode dispersion. There are some other types of advanced modulation formats such as PAM-4, 16QAM, and 32QAM that are currently employed in optical links to increase the capacity of optical networks that are utilized in either long-haul optical transport or intra-data center communications.

2.7 Passive optical networks and Gigabit passive optical networks

Due to recent demands for higher capacity and larger bandwidth, new access networks require to transmit data at high-speed (more than 100 Mb/s) in symmetric platforms instead of only a peak bandwidth of 100 Mb/s that is shared with many subscribers [113]. Since video-centric applications will drive bandwidth demand in future access networks, it is necessary to guarantee bandwidths for video services over 20 km transmission distance. Besides technical performance, economic considerations, small footprint and low-power consumption play key roles in choosing a network architecture. Passive optical networks (PON) allow sharing of the infrastructure and components at the central office (CO). It is cost-efficient to use the unlimited transmission bandwidth of single mode optical fiber over large distances. PON is applicable to point-to-multipoint architecture enabling a higher number of optical network unit (ONU)s to communicate on a single feeder fiber [114].

2.7.1 The comparison between TDM-PON and WDM-PON

Various applications require sharing a PON architecture. There are two main access techniques for practical future systems. The first technique is the time division multiple (TDM) access. In TDM a single transmission channel passes through an optical splitter and is shared with multiple subscribers in the time domain. There is a tight coupling between subscribers. TDM-PON is popular for the current bandwidth demands. The second technique is the WDM access. In WDM a dedicated pair of wavelengths is specified per user. This provides a point-to-point bidirectional optical connection over a shared infrastructure with cost-efficient transmitters and receivers. WDM-PON offers large improvements in optical power penalty and many management issues related to sharing the PON are eliminated. Considering the combination of recent advances in WDM technology coupled with future data rate projections and traffic patterns, WDM-PON is the most preferred technology for the future fiber-based access networks.

2.7.2 Colorless optical network unit techniques applied in WDM-PON

In general, a group of ONUs or all ONUs emit and receive wavelengths that are different from their neighbors. Using colorless (i.e. wavelength independent) ONU lowers the cost of utilizing WDM-PON in large-scale optical networks and makes maintenance easier.

There are several techniques to obtain colorless ONU to provide identical optical network terminals (ONT)s to all the subscribers. Some of the widely used techniques [113] are listed here.

- Tunable lasers are used as transmitters. For a given network configuration the wavelength at the installation can be tuned with appropriate tuning speed. Economically it is only efficient to utilize this method in small-scale access networks.

- Broadband sources with spectrum slicing are a cost-efficient alternative technique to the tunable laser method. As an example, the super-luminescent diode is applicable in this method and has high power emitted output with customized wavelength center and wavelength width. However, the modulation speed can only reach around 1 Gbit/s and dispersion and slicing loss limits the transmission distance.
- The remote modulation technique is preferred for high bitrate data transmissions. This method is cost-efficient, and has very low dispersion dependency. From the CO, an optical carrier is sent, and the upstream data is modulated at the ONU which will be sent back to the optical line terminal (OLT). To adapt data transfer to different bitrates various optical components can be used as a modulator.

2.7.3 Optical components for remote modulation techniques

Based on injection-locked Fabry-Perot (IL-FP) laser diodes, colorless ONUs have been proposed for the data transfer at bitrates up to 1.25 Gb/s. IL-FP is usually coupled to an unpolarized, incoherent and multi-wavelength broadband source. The unpolarized source is a solution to polarization dependency issue of the IL-FP laser. In TDM-PONs, conventional FP lasers are employed because they represent the cheapest solution. However, FP laser cavities are not suitable for WDM-PON because of their high gain bandwidth which arises in relation to their multimodal propagation [115]. The IL-FP technique is quite expensive and due to backscattering problems, it requires additional fibers to send the seed. As a result, the number of users would be limited by the locking range.

For bitrates higher than 1.25 Gb/s, the reflective semiconductor optical amplifier (RSOA) is proposed as a suitable single fiber architecture. Plenty of colorless ONU solutions are based on the use of semiconductor optical amplifiers (SOA)s and RSOAs [115]. Their usage is considered strategic because no light source is needed at the ONU which eases the maintenance. In addition, they can modulate and amplify the signal simultaneously with low polarization dependency instead of using separate devices with extra manufacturing cost. In the RSOA configuration, the signal travels twice through the device which allows double gain and makes it a cost-efficient optical component due to its gain property. However, RSOA-based systems performance is restricted by saturation power and chirping effect which limits the power budget. Moreover, the power budget is reduced due to Rayleigh backscattering and other reflections from connectors and splices in the fiber link but the required injected power can be as low as -20 dBm [114]. The modulation bandwidth of RSOA is insufficient and prevents the device from being directly modulated at data rates of 10 Gb/s, without using complex modulation formats [116]. Currently RSOAs are expensive for large-scale applications in PONs and they require TEC modules for cooling.

For a bitrate of 10 Gb/s, electro-absorption modulator (EAM) is applicable. EAM has the large electrical bandwidth and low polarization dependency. However, it is not cost-efficient, and its insertion loss is very high. Usually semiconductor optical amplifiers (SOA)s are needed in the optical path to compensate propagation loss and provide round-trip transmission in the network. The power budget for the EAM based approach would be more challenging than the other two schemes mentioned before. Some integrated version of EAM+SOA are developed recently to lower the loss but still their usage is limited in current network architectures.

Within the OLT of a WDM-PON there is also a need to reduce optical component costs to meet the requirements of access networks. At the OLT photonic integration offers a great opportunity for high-density integration and high volumes production not only to reduce cost and size but also to eliminate the fiber traffic [117]. Moreover, with the right choice of integration technology it should be possible to achieve cooler-less operation of DWDM modules which leads to significant reductions in power consumption. Components for the next generation access networks should be compact, colorless (i.e. wavelength-agnostic) and cooler-less (i.e. avoid using a thermoelectric cooler (TEC)) [118]–[122].

2.8 Conclusion

In this chapter we explained the recent demands in optical networks for higher capacities and larger bandwidths. To fulfill these demands optical components need to improve in order to provide low-power consumption. Here we reviewed different materials and techniques to develop power-efficient optical switches and modulators. Considering forthcoming applications in passive optical networks, eventually we can conclude that among the preferred materials and techniques for future designs, silicon-based EO switches and modulators play a leading role.

References

[1] T. S. El-Bawab, *Optical switching*. New York: Springer US, 2006.

[2] M. Menard, “Integrated Fabry-Perot optical space switches,” McGill University, Canada, 2009.

[3] J. R. Erickson, “Guided-Wave Optical Switching,” *IEEE Trans. Consum. Electron.*, vol. 35, no. 2, pp. 125–132, 1989.

[4] Y. Semenova, “Optical Communications Systems, Optical Switching,” Dublin Institute of Technology, 2003.

[5] Papadimitriou, G. I., C. Papazoglou, and A. S. Pomportsis., “Optical switching: switch fabrics, techniques, and architectures,” *J. Light. Technol.*, vol. 21, no. 2, pp. 384–405, 2003.

[6] E. Hecht, *Optics*, 4th ed. Addison Wesley, 2003.

[7] A. Yariv, *Photonics: Optical Electronics in Modern Communications*, 6th ed. New York: Oxford University Press, 2007.

[8] A. Shacham, K. Bergman, and L. P. Carloni, “Photonic networks-on-chip for future generations of chip multiprocessors,” *IEEE Trans. Comput.*, vol. 57, no. 9, pp. 1246–1260, 2008.

[9] R. Ding *et al.*, “Sub-volt silicon-organic electro-optic modulator with 500 MHz bandwidth,” *J. Light. Technol.*, vol. 29, no. 8, pp. 1112–1117, 2011.

[10] X. Zhang, A. Hosseini, X. Lin, H. Subbaraman, and R. T. Chen, “Polymer-based hybrid-integrated photonic devices for silicon on-chip modulation and board-level optical interconnects,” *IEEE J. Sel. Top. Quantum Electron.*, vol. 19, no. 6, 2013.

[11] M. R. Watts, D. C. Trotter, R. W. Young, and A. L. Lentine, “Ultralow power silicon microdisk modulators and switches,” *2008 5th Int. Conf. Gr. IV Photonics, GFP*, vol. 2, no. ll, pp. 4–6, 2008.

[12] P. Dong, “Low voltage silicon photonic modulators,” *IEEE Photonics Soc. Summer Top. Meet. Ser. PSST 2012*, vol. 1, pp. 130–131, 2012.

[13] L. R. Dalton *et al.*, “From molecules to opto-chips : organic electro-optic materials,” *J. Mater. Chem.*, vol. 9, no. 9, pp. 1905–1920, 1999.

[14] M. Glick, “The role of integrated photonics in datacenter networks,” *Next Gener. Opt. Networks Data Centers Short-Reach Links IV*, vol. SPIE 10131, p. 1013104, 2017.

[15] C. H. Tsai and J. C. Tsai, “MEMS optical switches and interconnects,” *Elsevier Displays*, vol. 37, pp. 33–40, 2015.

[16] R. R. A. Syms, “Scaling laws for MEMS mirror-rotation optical cross connect switches,” *J. Light. Technol.*, vol. 20, no. 7, pp. 1084–1094, 2002.

[17] M. Simard, Z. Khalid, and A. G. Kirk, “Digital optical space switch based on micromotor grating scanners,” *IEEE Photon. Tech. Lett.*, vol. 18, no. 1–4, pp. 313–315, 2006.

[18] W. Li *et al.*, “Design and fabrication of a micro-optic switch,” *Opt. Express*, vol. 16, no. 9, pp. 6324–6330, 2008.

[19] Y. J. Yang, W. C. Kuo, K. C. Fan, and W. L. Lin, “A 1x2 optical fiber switch using a dual-thickness SOI process,” *J. Micromech Microeng*, vol. 17, no. 5, pp. 1034–1041, 2007.

[20] A. K. Dutta, N. K. Dutta, and M. Fujiwara, *WDM technologies: passive optical components*, Vol. II. Boston MA USA, 2003.

[21] X. Ma and G.-S. Kuo., “Optical switching technology comparison: optical MEMS vs. other technologies,” *IEEE Commun. Mag.*, vol. 41, no. 11, pp. S16–S23, 2003.

[22] M. J. Potasek, “All-optical switching for high bandwidth optical networks,” *Opt. Networks Mag.*, vol. 3, no. 6, pp. 30–43, 2002.

[23] J. Ma, “Advanced MEMS-based technologies and displays,” *Elsevier Displays*, vol. 37, pp. 2–10, 2015.

[24] E. Gusev, E. Garfunkel, and A. Dideikin, *Advanced Materials and Technologies for Micro/Nano-Devices, Sensors and Actuators*. Springer, 2010.

[25] J. T. Y. and R. M. O. R. L. Espinola, M. C. Tsai, “Fast and Low-Power Thermooptic Switch on Thin Silicon-on-Insulator,” *IEEE Photonics Tech. Lett.*, vol. 15, no. 10, 2003.

[26] A. M. Al-Hetar, A. S. M. Supa’at, A. B. Mohammad, and I. Yuhanti, “Crosstalk improvement of a thermo-optic polymer waveguide MZI-MMI switch,” *Opt. Commun.*, vol. 281, no. 23, pp. 5764–5767, 2008.

[27] M. C. Oh, H. J. Lee, M. H. Lee, J. H. Ahn, and S. G. Han, “Asymmetric X-junction thermooptic switches based on fluorinated polymer waveguides,” *IEEE Photon. Tech. Lett.*, vol. 10, no. 6, pp. 813–815, 1998.

[28] A. Chen and E. Murphy, *Broadband Optical Modulators: Science, Technology, and Applications*, Illustrate. CRC Press, 2016.

[29] D. Po, “Low V pp, ultralow-energy, compact, high-speed silicon electro-optic modulator,” *Opt. Express*, vol. 17, no. 25, pp. 22484–22490, 2009.

[30] D. J. Thomson, “High contrast 40Gbit/s optical modulation in silicon,” *Opt. Express*, vol. 19, no. 12, pp. 11507–11516, 2011.

[31] Long and Chen, “Monolithic silicon chip with 10 modulator channels at 25 Gbps and 100-GHz spacing,” *Opt. Express*, vol. 19, no. 26, pp. B946–B951, 2011.

[32] P. Dong, L. Chen, and Y. Chen, “High-speed low-voltage single-drive push-pull silicon Mach-Zehnder modulators,” *Opt. Express*, vol. 20, no. 6, pp. 6163–6169, 2012.

[33] D. Po, “High-speed and compact silicon modulator based on a racetrack resonator with a 1 V drive voltage,” *Opt. Lett.*, vol. 35, no. 19, pp. 3246–3248, 2010.

[34] R. C. Alferness, “Waveguide Electro-optic Modulators,” *IEEE Transactions on Microwave Theory and Techniques*, vol. 30, no. 8. pp. 1121–1137, 1982.

[35] D. Janner, D. Tulli, M. García-Granda, M. Belmonte, and V. Pruneri, “Micro-structured integrated electro-optic LiNbO3 modulators,” *Laser Photon. Rev.*, vol. 3, no. 3, pp. 301–313, 2009.

[36] H. N. Klein, H. Chen, D. Hoffmann, S. Staroske, A. G. Steffan, and K. O. Velthaus, “1.55

um Mach-Zehnder Modulators on InP for Optical 40/80 Gbit/s Transmission Networks," *2006 International Conference on Indium Phosphide and Related Materials Conference Proceedings*. pp. 171–173, 2006.

[37] K. Tsuzuki *et al.*, "40 Gbit/s n-i-n InP Mach-Zehnder modulator with a V-pi voltage of 2.2 V," *Electronics Letters*, vol. 39, no. 20. pp. 1464–1466, 2003.

[38] H. Chen, "Development of an 80 Gbit / s InP-based Mach-Zehnder Modulator," *Thesis*, 2007.

[39] H. Klein, "Integrated InP Mach-Zehnder Modulators for 100 Gbit/s Ethernet Applications using QPSK Modulation," 2010.

[40] N. P. S.R. Marder, B. Kippelen, A.K.Y. Jen, "Design and synthesis of chromophores and polymers for electro-optic and photorefractive applications," *Nature*, vol. 388, pp. 845–851, 1997.

[41] J. V. R. Dinu, D. Jin, G. Yu, B. Chen, D. Huang, H. Chen, A. Barklund, E. Miller, C. Wei, "Environmental stress testing of electro-optic polymer modulators," *J. Light. Tech.*, vol. 27, pp. 1527–1532, 2009.

[42] W. H. Steier, "Polymer electro-optic devices for integrated optics," *Chem. Phys.*, vol. 245, no. 1, pp. 487–506, 1999.

[43] M. L. L. Dalton, A. Harper, A. Ren, F. Wang, G. Todorova, J. Chen, C. Zhang, "Polymeric electro-optic modulators: From chromophore design to integration with semiconductor very large scale integration electronics and silica fiber optics," *Ind. Eng. Chem. Res.*, vol. 35, no. 8, 1999.

[44] L. R. D. S. Kalluri, A. Chen, V. Chuyanov, M. Ziari, W. H. Steier, "Integration of polymer electro-optic devices on nonplanar silicon integrated circuits," in *Proc. SPIE, 375*, 1995, p. 2527.

[45] Lee and Myung-Hyun, "Polymer-based devices for optical communications," *ETRI J.*, vol. 24, no. 2, pp. 259–269, 2002.

[46] R. M. and K. Petermann, "4x4 Digital Optical Matrix Switch Using Polymeric Oversized Rib Waveguides," *IEEE Photon. Technol. Lett.*, vol. 10, no. 5, pp. 684–686, 1998.

[47] M. H. and L. R. D. S.M. Garner, V. Chuyanov, S. S. Lee, A. Yacoubian, A. Chen, W. H. Steier, F. Wang, A. S. Ren, "Three dimensional integrated optics using polymers," *IEEE*

Photonics Technol. Lett., vol. 11, p. 842, 1999.

[48] W. V. and D. M. B. J. I. Thackara, J. C. Chon, G. C. Bjorklund, "Polymeric electro-optic Mach-Zehnder switches," *Appl. Phys. Lett.*, vol. 67, p. 3874, 1995.

[49] H. F. and L. R. D. S. Kalluri, Z. Ziari, A. Chen, V. Chuyanov, W. H. Steier, D. Chen, B. Jalali, "Monolithic integration of waveguide polymer electro-optic modulators on VLSI circuitry," *IEEE Photonics Technol. Lett.*, vol. 8, p. 644, 1996.

[50] N. T. Sandhya K. Yesodha, Chennakattu K. Sadashiva Pillai, "Stable polymeric materials for nonlinear optics: a review based on azobenzene systems," *Prog. Polym. Sci.*, vol. 29, pp. 45–74, 2004.

[51] W. H. S. and H. R. F. W. Yuan, S. Kim, G. Sadowy, C. Zhang, C. Wang, "Polymeric electro-optic digital optical switches with low switching voltage," *Electron. Lett.*, vol. 40, no. 3, 2004.

[52] Y. A. V. Joris Van Campenhout, William M. J. Green, Solomon Assefa, "Ultra-Broadband, Low-Power, 2x2 Electro-Optic Switch using Sub-Micron Silicon Waveguides," in *IEEE OFC conference*, 2010.

[53] D. Thomson *et al.*, "High-performance Mach-Zehnder based silicon optical modulators," *IEEE J. Sel. Top. Quantum Electron.*, vol. 19, no. 6, p. 3400510, 2013.

[54] T. Y. Liow *et al.*, "Silicon modulators and germanium photodetectors on SOI: Monolithic integration, compatibility, and performance optimization," *IEEE J. Sel. Top. Quantum Electron.*, vol. 16, no. 1, pp. 307–315, 2010.

[55] L. C. Rasigade, G., Marris-Morini, D., Vivien, "Performance evolutions of carrier depletion silicon optical modulators: from PN to PIPIN diodes," *IEEE J. Sel. Top. Quantum Electron.*, vol. 16, no. 1, pp. 179–184, 2010.

[56] R. S. Jacobsen *et al.*, "Strained silicon as a new electro-optic material," *Nature*, vol. 441, no. 7090, pp. 199–202, May 2006.

[57] S. Jongthammanurak *et al.*, "Large electro-optic effect in tensile strained Ge-on-Si films," *Appl. Phys. Lett.*, vol. 89, no. 16, 2006.

[58] Y.-H. Kuo *et al.*, "Strong quantum-confined Stark effect in germanium quantum-well structures on silicon," *Nature*, vol. 437, no. 7063, pp. 1334–1336, Oct. 2005.

[59] A. Liu *et al.*, "A high-speed silicon optical modulator based on a metal-oxide-

semiconductor capacitor," *Nature*, vol. 427, no. 6975, pp. 615–618, Feb. 2004.

[60] L. Liao *et al.*, "High-speed silicon Mach-Zehnder modulator," *Opt. Express*, vol. 13, no. 8, pp. 3129–3135, 2005.

[61] S. Manipatruni, "High-speed carrier injection 18 Gb/s silicon micro-ring electro-optic modulator," in *Lasers and Electro-Optics Society LEOS and The 20th Annual Meeting of the IEEE*, 2007.

[62] L. Liao *et al.*, "40 Gbit/s silicon optical modulator for high-speed applications," *Electronics Letters*, vol. 43, no. 22. p. 1, 2007.

[63] W. M. J. Green, M. J. Rooks, L. Sekaric, and Y. A. Vlasov, "Ultra-compact , low RF power , 10 Gb / s silicon Mach-Zehnder modulator," *Opt. Express*, vol. 15, no. 25, pp. 17106–17113, 2007.

[64] T. Pinguet, V. Sadagopan, A. Mekis, B. Analui, D. Kucharski, and S. Gloeckner, "A 1550 nm, 10 Gbps optical modulator with integrated driver in 130 nm CMOS," *2007 4th IEEE International Conference on Group IV Photonics*. pp. 1–3, 2007.

[65] D. Marris-Morini, L. Vivien, J. M. Fédéli, E. Cassan, P. Lyan, and S. Laval, "Low loss and high-speed silicon optical modulator based on a lateral carrier depletion structure," *Opt. Express*, vol. 16, no. 1, pp. 334–339, 2008.

[66] R. A. Soref and B. R. Bennett, "Electrooptical effects in silicon," *IEEE J. Quantum Electron.*, vol. 23, no. 1, pp. 123–129, 1987.

[67] Y. A. Vlasov, "Silicon CMOS-integrated nano-photonics for computer and data communications beyond 100G," *IEEE Commun. Mag.*, vol. 50, no. 2, pp. 67–72, 2012.

[68] G. T. Reed, G. Mashanovich, F. Y. Gardes, and D. J. Thomson, "Silicon optical modulators," *Nat. Photonics*, vol. 4, no. 8, pp. 518–526, 2010.

[69] X. Zheng and A. V. Krishnamoorthy, "Si photonics technology for future optical interconnection," *Proc. SPIE 8309, Opt. Transm. Syst. Subsystems, Technol. IX*, vol. 8309, p. 83091V, 2011.

[70] P. Dong, Y.-K. Chen, G.-H. Duan, and D. T. Neilson, "Silicon photonic devices and integrated circuits," *Nanophotonics*, vol. 3, no. 4–5, pp. 215–228, 2014.

[71] X. Chen, C. Li, and H. K. Tsang, "Device engineering for silicon photonics," *NPG Asia Mater.*, vol. 3, no. 1, pp. 34–40, 2011.

[72] Krishnamoorthy and A. V., “Computer systems based on silicon photonic interconnects,” *Proc. IEEE*, vol. 97, no. 7, pp. 1337–1361, 2009.

[73] W. Bogaerts, M. Fiers, and P. Dumon, “Design Challenges in Silicon Photonics,” *IEEE J. Sel. Top. Quantum Electron.*, vol. 20, no. 4, pp. 1–8, 2014.

[74] G. L. Li and P. K. L. Yu, “Optical Intensity Modulators for Digital and Analog Applications,” *Lightwave*, vol. 21, no. 9, pp. 2010–2030, 2010.

[75] D. A. B. Miller, “Energy consumption in optical modulators for interconnects,” *Opt. Express*, vol. 20, no. S2, pp. A293–A308, 2012.

[76] T. Ye and X. Cai, “On power consumption of silicon-microring-based optical modulators,” *J. Light. Technol.*, vol. 28, no. 11, pp. 1615–1623, 2010.

[77] MLA and *et al.* Liu, Ansheng, “High-speed optical modulation based on carrier depletion in a silicon waveguide,” *Opt. Express*, vol. 15, no. 2, pp. 660–668, 2007.

[78] S. Akiyama *et al.*, “12.5-Gb/s operation with 0.29-V· cm Vπ.L using silicon Mach-Zehnder modulator based on forward-biased pin diode,” *Opt. Express*, vol. 20, no. 3, pp. 2911–2923, 2012.

[79] D. R., “Demonstration of a low V π L modulator with GHz bandwidth based on electro-optic polymer-clad silicon slot waveguides,” *Opt. Express*, vol. 18, no. 15, pp. 15618–15623, 2010.

[80] M. L. Manipatruni, Sasikanth, Long Chen, “50 Gbit/s wavelength division multiplexing using silicon microring modulators,” in *Group IV Photonics, GFP and 6th IEEE International Conference on. IEEE*, 2009.

[81] G. Li, “25Gb/s 1V-driving CMOS ring modulator with integrated thermal tuning,” *Opt. Express*, vol. 19, no. 21, pp. 20435–20443, 2001.

[82] W. A. Zortman, “Low-voltage differentially-signaled modulators,” *Opt. Express*, vol. 19, no. 27, pp. 26017–26026, 2011.

[83] A. L. Glebov, M. G. Lee, L. Huang, S. Aoki, K. Yokouchi, and M. K. M. Ishii, “Electro-optic planar deflector switches with thin film PLZT active elements,” *IEEE J Sel. Top. Quant*, vol. 11, no. 2, pp. 422–430, 2005.

[84] H. O. A. Sugama, T. Akahoshi, K. Sato, S. Aoki, Y. Kai, Y. Takita, M. Kato, “Integrated 8x8 Electro-optic High-Speed Switch for Optical Burst Transport Networks,” in *Optical Fiber*

Communication Conference, 2007.

[85] W. S. C. C. C. H. Peng, R. J. Falster, "NxM planar optical-waveguide switch for computer communications," *J Opt Soc Am*, vol. 70, no. 12, pp. 1577–1578, 1981.

[86] M. F. E. M. Philipp-rutz, R. Linares, "Electro-optic Bragg-diffraction switches in low cross talk integrated optics switching matrix," *Appl. Opt.*, vol. 21, no. 12, pp. 2189–2194, 1982.

[87] Y. N. T. Tanemura, M. Takenaka, A. Abdullah, K. Takeda, T. Shioda, M. Sugiyama, "Design and Fabrication of Integrated 1x5 Optical Phased Array Switch on InP," in *The 20th Annual Meeting of the IEEE Lasers and Electro-Optics Society*, 2007, pp. 780–781.

[88] T. H. L. M. Jarrahi, R. Fabian, W. Pease, D. A. B. Miller, "Optical switching based on high-speed phased array optical beam steering," *Appl. Phys. Lett.*, vol. 92, no. 1, 2008.

[89] T. E. S. Y. Chiu, J. Zou, D. D. Stancil, "Shape-optimized electro-optic beam scanners: Analysis, design, and simulation," *J Light. Technol.*, vol. 17, no. 1, pp. 108–114, 1999.

[90] D. V. P. Y. Y. Zuo, M. Mony, B. Bahamin, E. Grondin, V. Aimez, "Bulk electro-optic deflector-based switches," *Appl. Opt.*, vol. 46, no. 16, p. . 3323-3331, 2007.

[91] "OMM Inc. [Online]." [Online]. Available: available: http://www.omminc.com/products/datasheets.html.

[92] J. V. G. J. Kim, C. J. Nuzman, B. Kumar, D. F. Lieuwen, J. S. Kraus, A. Weiss, C. P. Lichtenwalner, A. R. Papazian, R. E. Frahm, N. R. Basavanhally, D. A. Ramsey, V. A. Aksyuk, F. Pardo, M. E. Simon, V. Lifton, H. B. Chan, M. Haueis, A. Gasparyan, H. R. Shea, S. A, "1100 x 1100 port MEMS-based optical crossconnect with 4-dB maximum loss," *EEE Photon. Tech. Lett.*, vol. 15, no. 11, pp. 1537–1539, 2003.

[93] J. S. Turner, "WDM burst switching for petabit data networks," in *Opt. Fiber Commun. Conf. Tech. Dig. Postconference Edition. Trends Opt. and Photon, Vol. 37*, 2000, pp. 47–49.

[94] "NEL NTT Electronics Corp. [Online]." [Online]. Available: available: http://www.nelworld.com/products/photonics/thermo_opt_88.html.

[95] P. L. A. Borreman, T. Hoekstra, M. Diemeer, H. Hoekstra, "Polymeric 8x8 digital optical switch matrix," in *European Conference on Optical Communication, Vol. 5*, 1996, pp. 59–62.

[96] H. T. S. Sohma, T. Watanabe, N. Ooba, M. Itoh, T. Shibata, “Silica-based PLC Type 32x32 Optical Matrix Switch,” in *European Conference on Optical Communications*, 2006, pp. 1–2.

[97] K. H. T. Goh, A. Himeno, M. Okuno, H. Takahashi, “High-extinction ratio and low-loss silica-based 8x8 strictly nonblocking thermooptic matrix switch,” *J Light. Technol*, vol. 17, no. 7, pp. 1192–1199, 1999.

[98] S. O. Y. Yamabayashi, M. Koga, “Autonomously controlled multiprotocol wavelength switching network for Internet backbones,” *IEICE Trans. Commun*, vol. E83B, no. 10, pp. 2210–2215, 2000.

[99] W. I. K. Sato, N. Yamanaka, Y. Takigawa, M. Koga, S. Okamoto, K. Shiomoto, E. Oki, “GMPLS-based photonic multilayer router (Hikari router) architecture: An overview of traffic engineering and signaling technology,” *IEEE Commun. Mag.*, vol. 40, no. 3, pp. 96–101, 2002.

[100] “Lynx Photonic Networks [Online].” [Online]. Available: available: http://www.lynxnetworks.com/prod/packet8x8detail_new.asp.

[101] S.-W. A. and S. Shin, “Grating-Assisted Codirectional Coupler Filter Using Electro-optic and Passive Polymer Waveguides,” *IEEE J. Sel. Top. quantum Electron.*, vol. 7, no. 5, 2001.

[102] M. B. E. Shekel, D. Majer, G. Matmon, A. Krauss, S. Ruschin, T. McDermott, M. Birk, “Broadband testing of a 64x64 nanosecond optical switch,” in *The 15th Annual Meeting of the IEEE Lasers and Electro-Optics Society, vol.2*, 2002, pp. 371–372.

[103] H. M. R. Krahenbuhl, R. Kyburz, W. Vogt, M. Bachmann, T. Brenner, E. Gini, “Low-loss polarization-insensitive InP-InGaAsP optical space switches for fiber optical communication,” *IEEE Photon. Tech. Lett.*, vol. 8, no. 5, pp. 632–634, 1996.

[104] T. S. Y. Nakabayashi, M. Kitamura, “DC-drift free polarization independent Ti:LiNbO3 8x8 optical matrix switch,” in *European Conference on Optical Communication, Vol.4*, 1996, pp. 157–160.

[105] M. E. M. Renaud, M. Bachmann, “Semiconductor optical space switches,” *IEEE J Sel. Top. Quant*, vol. 2, no. 2, pp. 277–288, 1996.

[106] H. O. and M. Kawahara, “Ti:LiNbO3 digital optical switch matrices,” *Electron. Lett.*, vol.

29, pp. 765–766, 1993.

[107] L. Pavesi and D. J. Lockwood, *Silicon photonics*, vol. 1. Springer Science & Business Media, 2004.

[108] A. H. Gnauck and P. J. Winzer, “Optical phase-shift-keyed transmission,” *J. Light. Technol.*, vol. 23, no. 1, pp. 115–130, 2005.

[109] P. S. Henry, “Error-rate performance of optical amplifiers,” in *OFC*, 1989, p. THK3.

[110] P. A. Humblet and M. Azizoglu, “On the bit error rate f lightwave systems with optical amplifiers,” *Light. Technol.*, vol. 9, no. 11, pp. 1576–1582, 1991.

[111] G. Jacobsen, *Noise in digital optical transmission systems*. Boston MA: Artech House, 1994.

[112] S. R. Chinn, D. M. Boroson, and J. C. Livas, “Sensitivity of optically preamplified DPSK recievers with Fabry-Perot filters,” *Light. Technol.*, vol. 14, no. 3, pp. 370–376, 1996.

[113] F. Payoux, P. Chanclou, and N. Genay, “WDM-PON with colorless ONUs,” *OFC/NFOEC 2007 - Opt. Fiber Commun. Natl. Fiber Opt. Eng. Conf. 2007*, pp. 2–4, 2007.

[114] T. Koonen, “Fiber to the home/fiber to the premises: What, where, and when?,” *Proc. IEEE*, vol. 94, no. 5, pp. 911–934, 2006.

[115] T. Muciaccia, F. Gargano, and V. Passaro, “Passive Optical Access Networks: State of the Art and Future Evolution,” *Photonics*, vol. 1, no. 4, pp. 323–346, 2014.

[116] B. Schrenk, G. De Valicourt, M. Omella, J. A. Lazaro, R. Brenot, and J. Prat, “Direct 10-Gb/s modulation of a single-section RSOA in PONs with high optical budget,” *IEEE Photonics Technol. Lett.*, vol. 22, no. 6, pp. 392–394, 2010.

[117] G. de Valicourt *et al.*, “Directly modulated and fully tunable hybrid silicon lasers for future generation of coherent colorless ONU,” *Opt. Express*, vol. 20, no. 26, pp. B552-7, 2012.

[118] D. W. Smith, “Reducing the optical component cost for future fiber access,” in *35th European Conference on Optical Communication*, 2009, pp. 4–5.

[119] L. H. Spiekman, “Active devices in passive optical networks,” *J. Light. Technol.*, vol. 31, no. 4, pp. 488–497, 2013.

[120] P. Vetter *et al.*, “Energy efficiency improvements for optical access,” *IEEE Commun. Mag.*, vol. 52, no. 4, pp. 136–141, 2014.

[121] J. Elbers, “Optical Access Solutions Beyond 10G-EPON / XG-PON,” in *Optic Engineers Conference (OFC/NFOEC)*, 2010, pp. 8–10.

[122] S. Lambert *et al.*, “Power consumption evaluation for next-generation passive optical networks,” in *24th Tyrrhenian International Workshop on Digital Communications - Green ICT, TIWDC*, 2013.

[123] T. J. Seok *et al.* “Large-scale broadband digital silicon photonic switches with vertical adiabatic couplers,” Optica, vol. 3, no. 1, pp 64-70, 2016.

Chapter 3

A Comparison of Switching Energy of Resonant and Non-Resonant Electro-Optic Switches

3.1 Introduction

Optical space switching is used as an important function of DWDM in optical communication systems, and particularly in reconfigurable optical add-drop multiplexers (ROADMs) [1]. Several years of research in optical transmission has produced a variety of switching technologies. Power consumption (i.e. energy per switching operation multiplied by switching rate) is a significant parameter in the selection of a switching technology. EO switches that utilize a refractive index change caused by an external voltage application (i.e. the Pockels effect) only dissipate power when the switch state is changed. EO switches have lately been considered as an option for satisfying the high traffic demands of networks and the possibility of achieving sub-microsecond response time. Space switches based on EO effects and current injection in silicon with nanosecond switching speeds and average power consumption on the order of mW have been introduced recently [2], [3]. EO switches can be implemented either as non-resonant designs (for example MZI) or as resonant designs (for example Fabry-Perot interferometer (FPI)).

In this chapter, the switching energies of EO MZI and EO FPI based switches are compared. This is a case study for comparison of the switching energy between resonant switches and non-resonant switches. The switching energy ratio is extracted depending on either a fixed length of the active region for interferometers or a fixed voltage applied to the modulation part of interferometers. It is also important to consider the fact that as the finesse of resonant cavity modulators increases (which typically allows a reduction in switching voltage) the maximum modulation bandwidth decreases due to the increase in photon lifetime in the cavity. As a result, at a certain modulation rate the switching energy of the resonant interferometer and the non-resonant interferometer become equal and the interferometers exhibit similar modulation characteristics. Here we investigate optical modulation based on the Pockels effect. However, according to [4] and [5], this theoretical formalism is also applicable to EO modulators based on free-carrier plasma dispersion in lumped electrodes regime. For both methods, a temporal response down to the femtosecond range is expected which enables ultrafast modulation beyond 1 THz [6].

3.2 EO switches

As mentioned in the introduction, EO switches are designed based on the Pockels effect [7], [8]. In the schematic of an EO switch, as shown in Figure 1, the induced electric field is defined as $E = V_G/h$ in which h is the distance between top and bottom electrodes and the input voltage is called V_G.

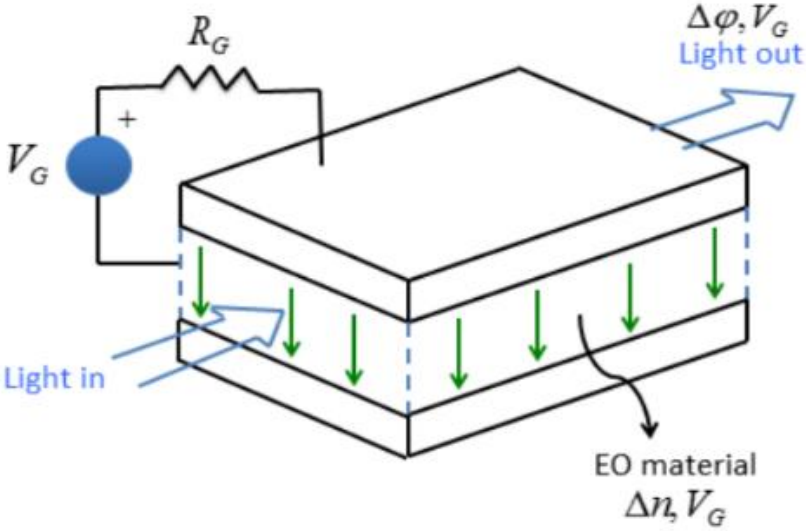

Figure 1 – Schematic of a switch designed based on the EO effect

The top and bottom electrodes act as plates of a capacitor whose dielectric is a slab of EO material that is placed between electrodes. By applying V_G the refractive index of EO material is changed by Δn. This introduces a phase shift to the input light and leads to the switched output light.

When different phase shifts are introduced in two arms of the Mach-Zehnder interferometer, changes in intensity can be observed at the output of the interferometer. Amplitude modulation can be obtained from phase shifts by making the two modulated beams interfere either constructively or destructively. This is the principle of the interferometer as shown in Figure 2 and Figure 3. When there is no phase shift light will interfere constructively resulting in maximum possible light out of the interferometer. The EO switch is called in ON state.

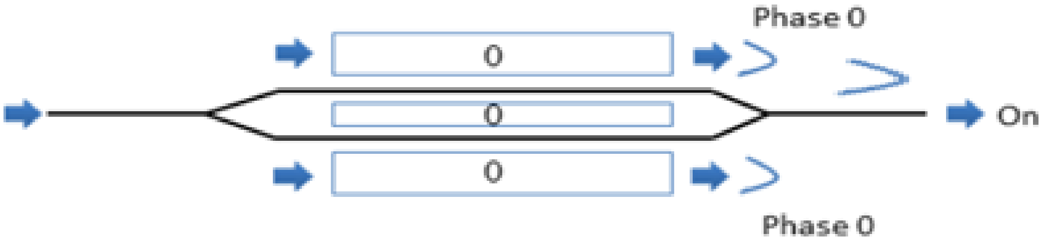

Figure 2 – Modulated light with constructive interference in an interferometer

When there is applied voltage on interferometer a π phase shift relative to the other arm would lead to destructive interference. The EO switch is called in OFF state.

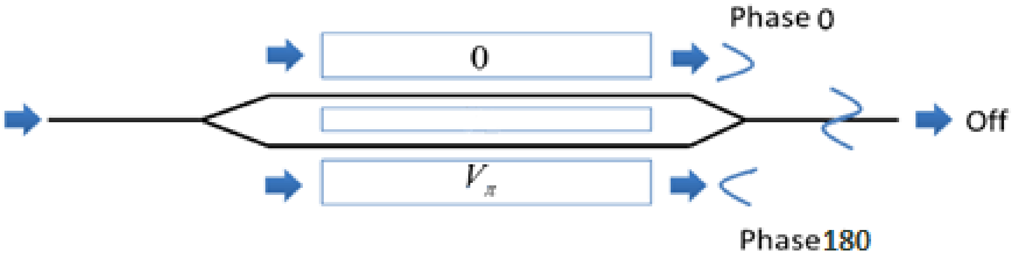

Figure 3 – Modulated light with destructive interference in an interferometer

Additionally, Figure 2 and Figure 3 show the schematic of an MZI that can be utilized to detect relative phase shifts between two optical paths [9]. The configuration of an

MZI is formed by splitting input light into two paths. When light travels in each path, it can be subjected to phase shift due to applied voltage by electrodes placed on the path. The output of the MZI is the result of recombination of light passing through these paths.

3.3 Energy calculation analysis

The switching energy of the MZI that was introduced in Section 3.2 will be derived in Section 3.3.1. The introduction of the FPI and its switching energy analysis is presented in Section 3.3.2.

3.3.1 Switching energy of an MZI

In Figure 4, a voltage is applied to the upper arm of an MZI (single-sided MZI) and its refractive index is changed by Δn.

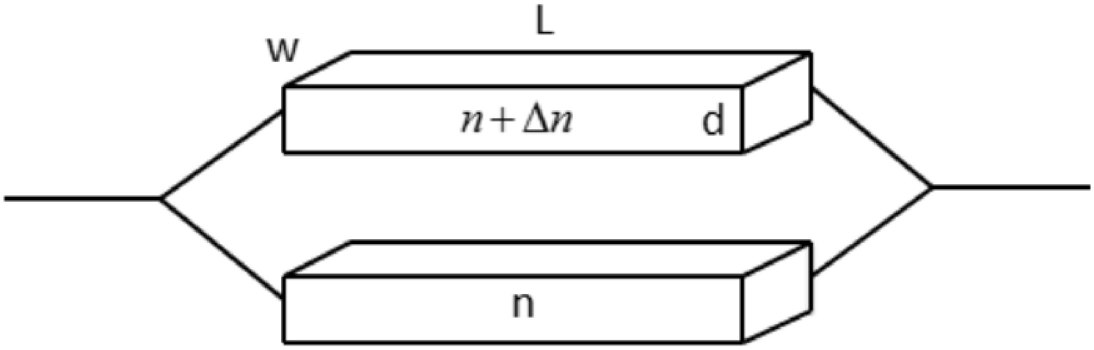

Figure 4 – Schematic view of a single-drive MZI

The optical path length (OPL) difference of the light propagating through the MZI is defined as

$$\Delta\mathrm{OPL}_{\mathrm{MZI}} = (n + \Delta n)L - nL \tag{1}$$

Ideally in an MZI for a phase shift of $\Delta\phi_{MZI} = \pi$, the $\mathrm{OPL}_{\mathrm{MZI}}$ should be equal to half a wavelength $\frac{\lambda}{2}$ as

$$\Delta nL = \frac{\lambda}{2} \tag{2}$$

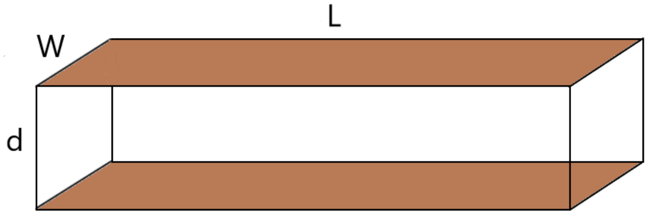

Figure 5 – The cuboid's brown sides are the top and bottom electrodes placed in active modulation region of an interferometer (for example the upper arm of an MZI or the resonant cavity of an FPI)

The top and bottom sides of an MZI's arm are connected to the electrodes. These electrodes behave like the plates of the capacitor in Figure 5. From the definition of the Pockels effect [10]

$$n(E) \approx n - \frac{1}{2} R n^3 E \tag{3}$$

Here R is the Pockels effect coefficient and n is ordinary index of refraction. Let the electrical field applied to a single arm of MZI be

$$E = \frac{V_{MZI}}{d} \tag{4}$$

In which V_{MZI} is the applied voltage, then the change of refractive index Δn will be

$$\Delta n = \frac{1}{2} R n^3 \frac{V_{MZI}}{d} \tag{5}$$

The phase difference is defined as

$$\Delta\phi_{MZI} = \frac{\mathrm{OPL_{MZI}}}{\lambda}(2\pi) = \frac{\Delta n L}{\lambda}(2\pi) \tag{6}$$

Thus as a substitution with (5) we will get

$$\Delta\phi_{MZI} = \frac{2\pi}{\lambda}\frac{1}{2} R n^3 \frac{V_{MZI}}{d} L_{MZI} \tag{7}$$

If $\Delta\phi_{MZI} = \pi$ then from Equation (6) and Equation (7) the voltage applied to MZI is

$$V_{MZI} = \frac{\lambda d}{R n^3 L_{MZI}} \tag{8}$$

In an MZI structure a capacitor is formed by a pair of parallel plates of electrodes. The capacitance can be written as

$$\mathrm{C}_{MZI} = \frac{\varepsilon A}{d} = \frac{\varepsilon L_{MZI} w}{d} \tag{9}$$

The switching energy that is dissipated in the capacitor formed by the MZI between charge and discharge states is shown in Equation (10). It is important to indicate this is an ideal model where there is no charge leakage while the switch is in one state or another.

$$E_{MZI} = \frac{1}{2}\mathrm{C}_{MZI}{V_{MZI}}^{2} = \frac{1}{2}\left(\frac{\varepsilon L_{MZI} w}{d}\right)\left(\frac{\lambda d}{Rn^{3}L_{MZI}}\right)^{2} = \frac{1}{2}\frac{\varepsilon w d \lambda^{2}}{R^{2}n^{6}L_{MZI}} \tag{10}$$

3.3.2 Switching energy of an FPI

A typical FPI consists of two partially reflecting mirrors of width *W* and length *d* that are separated by a gap size *L.* These dimensions are identical to the ones shown in Figure 5. Light incident on an FPI filter will experience multiple reflections within that gap which is considered as the modulation cavity of the interferometer. If the optical length of the cavity ($\mathrm{OPL}_{\mathrm{FPI}}$) formed of the two mirrors is an even multiple of the light half-wavelength $\frac{\lambda}{2}$, then light will be transmitted through the cavity. If the cavity optical length corresponds to odd multiples of $\frac{\lambda}{2}$, then light is completely reflected by the filter [11]. The phase shift that occurs by the two mirror reflections is $\Delta\phi_{FPI} = \pi$ at each mirror (which is similar to what happens in the case of metallic mirrors). The transmission response of FPI is periodic [12], [13] and a schematic of two periodic peaks is shown in Figure 6.

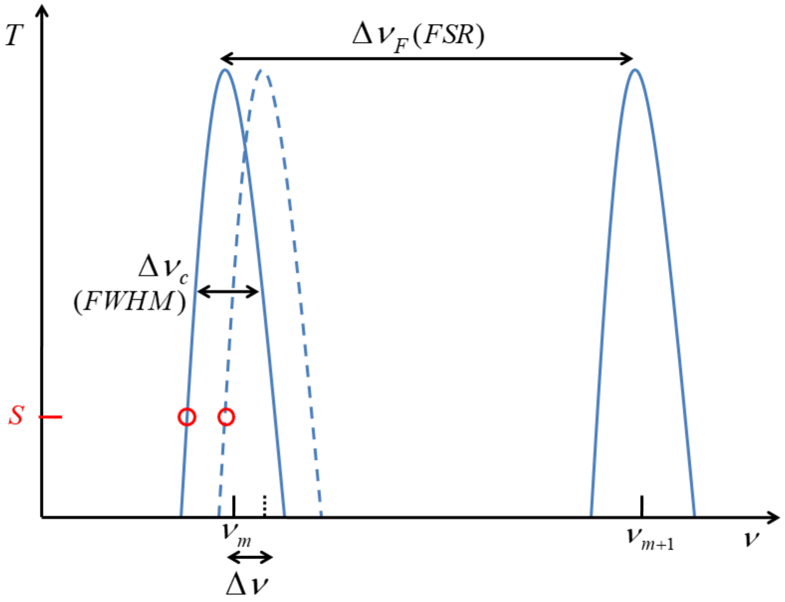

Figure 6 – Transmission over the frequency of an FPI

The full width at half maximum (FWHM) or modulation bandwidth in a cavity for a resonance peak is defined as

$$\Delta\nu_c = \frac{C}{2nL_{FPI}} \frac{1-\sqrt{R_1R_2}}{\sqrt[4]{R_1R_2}} \tag{11}$$

where C is the speed of light, R_1 is the reflectivity from the front-side mirror and R_2 is the reflectivity from the back-side mirror. The Free spectral range (FSR) of the cavity is defined as

$$\Delta\nu_F = \frac{C}{2nL_{FPI}} \tag{12}$$

The finesse is given by

$$F = \frac{\Delta\nu_F}{\Delta\nu_C} = \frac{\pi\sqrt[4]{R_1R_2}}{1-\sqrt{R_1R_2}} \tag{13}$$

If $R_1 = R_2 = R_r$ then

$$F = \frac{\pi\sqrt{R_r}}{1-R_r} \tag{14}$$

High finesse values can be achieved by using dielectric mirrors with high reflectivity. By using finesse defined in Equation (14), Equation (11) for the FWHM can be rewritten as

$$\Delta\nu_c = \frac{C}{2nL_{FPI}F} \tag{15}$$

In FPI, there is a trade-off between the modulation bandwidth and finesse. This means that in a resonant cavity, the higher the value of finesse, the lower the modulation bandwidth. The cavity modulation rate is defined as the rate of charge and discharge of the capacitance in the cavity and has an inverse relationship to the photon lifetime in the cavity. In view of Equation (15) and [15], the relation between the FWHM and the cavity modulation rate ($\frac{1}{\tau_c}$) can be defined as

$$\Delta\nu_c = \frac{C}{2nL_{FPI}F} = \frac{1}{\tau_c} \tag{16}$$

In conclusion the relation between the finesse and the photon lifetime is defined as

$$F = \frac{C}{2nL_{FPI}\,(\frac{1}{\tau_c})} \tag{17}$$

The change of refractive index (Δn) in FPI cavity causes a shift in the transmission frequency and consequently the transmittance is reduced. This reduction is defined as the isolation parameter [14] which is shown by S in Equation (18) below.

$$T(\nu,\Delta n) = \frac{\mathrm{S}}{1+\frac{4R_r}{(1-R_r)^2} sin^2(4\pi\frac{(n+\Delta n)\,L_{FPI}\,\nu}{C})} = \mathrm{S}\,T(\nu,0) \tag{18}$$

From Equations (14) and (18), the isolation has a value of

$$\mathrm{S} = \frac{1}{1+\frac{4F^2}{\pi^2}\,sin^2(4\pi\frac{\Delta n\,L_{FPI}\,\nu}{C})} \tag{19}$$

This value can be simplified to

$$\sqrt{\frac{1}{\mathrm{S}}-1} = \frac{4F}{\pi}\,\sin(4\pi\,\frac{\Delta n\,L_{FPI}\,\nu}{C}) \tag{20}$$

In the small-angle mathematical approximation, the phase is close to zero at the maximum value of a transmittance, and therefore

$$\sqrt{\frac{1}{\mathrm{S}}-1} = \frac{4F}{\pi}\,\frac{4\pi\,\Delta n\,L_{FPI}\,\nu}{C} \tag{21}$$

Which gives us the index change needed for a given isolation value:

$$\Delta n = \frac{c}{16FL_{FPI}\,\nu}\sqrt{\frac{1}{\mathrm{S}} - 1} \tag{22}$$

By considering the Pockels effect, the change of refractive index is given by

$$\Delta n = \frac{1}{2}Rn^3\frac{V_{FPI}}{d} \tag{23}$$

Accordingly, the applied voltage on FPI is derived from Equation (23) and results in

$$V_{FPI} = \frac{2d\Delta n}{Rn^3} \tag{24}$$

From above, the minimum applied voltage to FPI can be rewritten as

$$V_{FPI} = \frac{d\lambda}{Rn^3 8FL_{FPI}}\sqrt{\frac{1}{\mathrm{S}} - 1} \tag{25}$$

The electrodes of an FPI are on top and bottom sides of the cavity as shown in Figure 5. It is assumed that all of the dimensions of the MZI structure and the FPI cavity are identical. As a result, the calculated capacitances of the two interferometers resemble each other, that is

$$C_{FPI} = \frac{\varepsilon L_{FPI}w}{d} \tag{26}$$

The switching energy of an FPI is defined in Equation (27) in which the resonance behavior of the cavity is considered.

$$E_{FPI} = \frac{1}{2}C_{FPI}{V_{FPI}}^2 = \frac{1}{2}\left(\frac{\varepsilon L_{FPI}w}{d}\right)\left(\frac{d\lambda}{Rn^3 8FL_{FPI}}\right)^2\left(\frac{1}{\mathrm{S}} - 1\right) \tag{27}$$

If Equation (17) is substituted into Equation (27) then the switching energy for FPI can be written as

$$E_{FPI} = \frac{1}{2}\,\varepsilon L_{FPI}wd\left(\frac{1}{\mathrm{S}} - 1\right)\left(\frac{\lambda\frac{1}{\tau_c}}{4CRn^2}\right)^2 \tag{28}$$

As explained by Equations (14) and (15), finesse is determined by the modulation bandwidth. The trade-off between finesse and modulation bandwidth also affects switching energy in Equation (28). As a conclusion, a resonant modulator with high finesse has limited modulation bandwidth and low switching energy.

3.3.3 Switching energy comparison of FPI and MZI

We can compare the two types of devices on the basis of either equal lengths (i.e. assuming that space is the limiting factor) or equal supply voltage (i.e. assuming that voltage is the limiting factor). Taking the condition of equal lengths first, if $L_{MZI} = L_{FPI}$ then the ratio between the two energies in MZI and FPI will be

$$\frac{E_{FPI}}{E_{MZI}} = \frac{\frac{1}{S}-1}{(8F)^2} \tag{29}$$

From Equation (8) for minimum applied voltage to MZI, the maximum length of the device is

$$L_{MZI}(Max) = \frac{d\lambda}{Rn^3 V_{MZI-Min}} \tag{30}$$

From Equation (25) for minimum applied voltage to FPI, the maximum length of the device is

$$L_{FPI}(Max) = \frac{d\lambda}{8FRn^3 V_{FPI-Min}} \sqrt{\frac{1}{S}-1} \tag{31}$$

If $V_{MZI-Min} = V_{FPI-Min}$ then the ratio between the two energies in MZI and FPI will be

$$\frac{E_{FPI}}{E_{MZI}} = \frac{1}{8F} \sqrt{\frac{1}{S}-1} \tag{32}$$

The final comparison with an MZI depends on whether we want to compare the interferometers based on the assumption of equal length or equal voltage.

3.4 Analytical discussion

In this section, the analytical derivation of switching energy ratio between FPI and MZI will be discussed. Here two different cases are considered in these derivations, the first case is the fixed length of the active modulation region and the second case is the fixed voltage applied to the modulation region. It is important to mention in these models that the phase mismatch between the RF signals and the light waves propagation through the MZI arms is ignored.

3.4.1 The case for modulation region with a similar length

The values given in Table 1 are assigned to the indicated parameters in our model. Consequently, the relation between switching energy per bit and modulation frequency can be shown in Figure 7 and Figure 8. The numerical results related to the graphs in these figures are shown in Table 2.

Table 1 – Numerical values used for switching energy estimation

R	10 pm/V
n	1.5
λ_0	1550 nm
ε	8.85×10^{-12} F/m
w	500 nm
d	220 nm
S	0.01
Δn	1.7×10^{-4}
f_0	193.5 THz
R_r	0.95

If $L_{FPI} = L_{MZI} = 2.5\ \mathrm{mm}$ then the switching energy for both FPI and MZI relative to the frequency will be as shown in Figure 7. If the switching energies for MZI and FPI are assumed to be equal, that is $\frac{E_{FPI}}{E_{MZI}} = 1$, then the modulation rate (i.e. the frequency in which both interferometers show similar modulation characteristics) would be

$$\frac{1}{\tau_c} = \frac{4C}{L\, n \sqrt{\frac{1}{S} - 1}} \cong 32.16\ GHz \qquad (33)$$

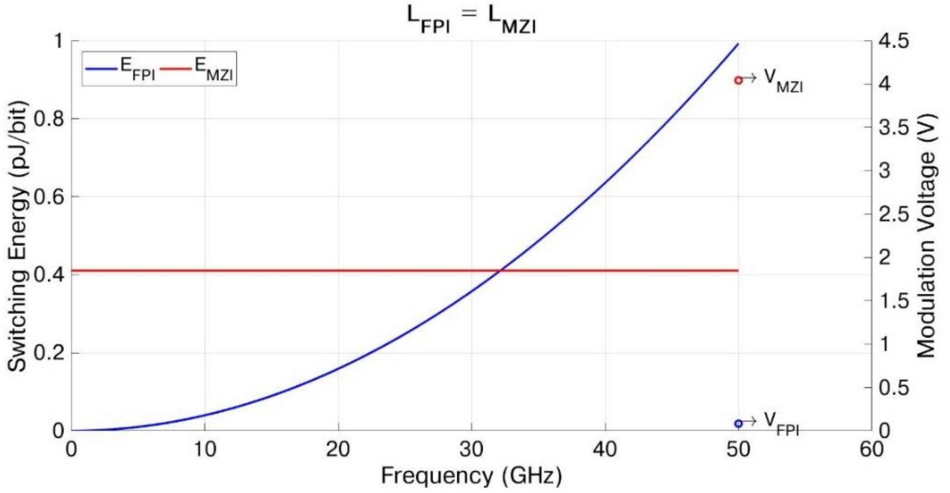

Figure 7 – Switching energy for FPI and MZI relative to the frequency for the case of $L_{FPI} = L_{MZI}$ – for numerical comparison V_{MZI} and V_{FPI} are applied modulation voltages according to Table 1 for this case

3.4.2 The case for modulation region with a similar voltage

If Equation (30) is substituted in Equation (10) then the E_{MZI} can be rewritten as

$$E_{MZI} = \frac{1}{2}\frac{\varepsilon w d\lambda^2}{R^2 n^6}\,\frac{Rn^3 V_{MZI}}{d\lambda} = \frac{1}{2}\frac{\varepsilon w\lambda V_{MZI}}{Rn^3} \tag{34}$$

If Equation (31) is substituted in Equation (28) then the E_{FPI} can be rewritten as

$$E_{FPI} = \frac{1}{2}\,\varepsilon wd\,\left(\frac{1}{S}-1\right)\left(\frac{\lambda\frac{1}{\tau_c}}{4CRn^2}\right)^2\frac{d\lambda}{8FRn^3V_{FPI}}\,\sqrt{\frac{1}{S}-1}$$

$$E_{FPI} = \frac{1}{2}\,\varepsilon wd^2\left(\frac{1}{S}-1\right)^{\frac{3}{2}}\,\frac{\lambda^3\,(\frac{1}{\tau_c})^2}{128C^2R^3n^7F\,V_{FPI}} \tag{35}$$

If $V_{FPI} = V_{MZI} = 4.0$ V then the switching energies for both FPI and MZI relative to the frequency will be as shown in Figure 8.

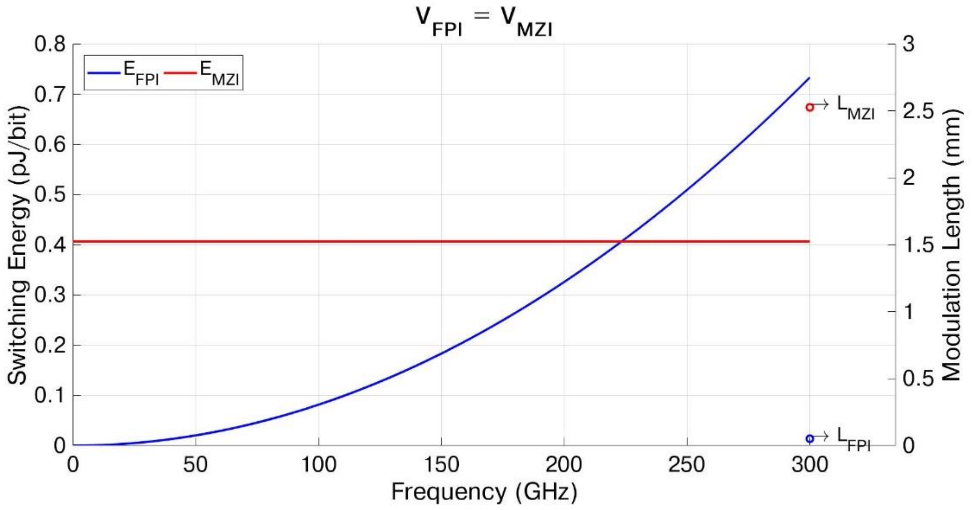

Figure 8 – Switching energy for FPI and MZI relative to the frequency for the case of $V_{FPI} = V_{MZI}$ – for numerical comparison L_{FPI} and L_{MZI} are length of these interferometers according to Table 1 for this case

Similar to the case in Section 3.4.1, if the switching energies for MZI and FPI are assumed to be equal, that is $\frac{E_{FPI}}{E_{MZI}} = 1$, then the modulation rate (i.e. the frequency in which both interferometers show similar modulation characteristics) would be

$$\frac{1}{\tau_c} = \frac{8CRn^2V}{d\lambda}\sqrt{\frac{2F}{\left(\frac{1}{S}-1\right)^{\frac{3}{2}}}} \cong 223.36\,GHz \qquad (36)$$

A summary of the simulation results for switching energy comparison of MZI and FPI is listed in Table 2.

Table 2 – Summary of simulation results for switching energy comparison of MZI and FPI

	Fixed length			Fixed voltage		
	V	L	Crossing frequency	V	L	Crossing frequency
FPI	0.082 V	2.5 mm	32.16 GHz	4 V	0.005 mm	223.36 GHz
MZI	4.041 V	2.5 mm		4 V	2.5 mm	

3.5 Conclusion

To compare the switching energy of the resonant and the non-resonant EO switches, it has been shown in this chapter and also in [5], [16] that the resonant switches are more power-efficient than non-resonant switches in optical networks at low frequencies. However, the resonant switches have a narrow transmission bandwidth that limits their applications in broadband systems. Furthermore, as it is calculated in this chapter there is a certain frequency at which the resonant and non-resonant switches require equal energy and their modulation characteristics become identical. From Figures 7 and 8 it can be inferred that at frequencies higher than this critical value, non-resonant switches are preferred. In this chapter we present a simple model that ignores many factors that would limit the maximum modulation rate efficiency such as velocity mismatch in the traveling-wave (TW) electrodes. It is necessary to note that many of these limits will affect resonant and non-resonant structures equally. Although this analysis was undertaken based on the Pockels effect, it will also be valid for devices that are based on plasma dispersion. According to [5] for a modulator operating by the plasma dispersion method, the refractive index change Δn in Equations (5) and (23) should be replaced by

$$\Delta n = \left(K_n + K_p\right). \exp(\frac{eV}{2k_B T}) \tag{37}$$

where K_n and K_p represent the linearized index change coefficients, k_B is the Boltzmann constant, and T is the junction temperature. The variety of available switches reflects the extent of the technologies that are employed in the software-defined networks. In this thesis we focus our investigation on EO FPI and EO MZI-based switches. Future work will provide a broader view of optical switching by comparing other existing switching technologies.

References

[1] T. S. El-Bawab, *Optical switching*. New York: Springer US, 2006.

[2] J. Van Campenhout, W. M. J. Green, S. Assefa, and Y. A. Vlasov, “Low-power, 2×2

silicon electro-optic switch with 110-nm bandwidth for broadband reconfigurable optical networks," *Opt. Express*, vol. 17, no. 26, pp. 24020–24029, 2009.

[3] Y. A. V. Joris Van Campenhout, William M. J. Green, Solomon Assefa, "Ultra-Broadband, Low-Power, 2x2 Electro-Optic Switch using Sub-Micron Silicon Waveguides," in *IEEE OFC conference*, 2010.

[4] D. A. B. Miller, "Energy consumption in optical modulators for interconnects," *Opt. Express*, vol. 20, no. S2, pp. A293–A308, 2012.

[5] H. Lin, S. Member, O. Ogbuu, J. Liu, L. Zhang, and J. Michel, "Breaking the energy - bandwidth limit of electro - optic modulators : theory and a device proposal," *J. Light. Technol.*, vol. 31, no. 24, pp. 4029–4036, 2013.

[6] D. A. B. Miller, "Device Requirement for Optical Interconnects to Silicon Chips," *Proc. IEEE Spec. Issue Silicon Photonics*, vol. 97, no. 7, pp. 1166–1185, 2009.

[7] H. S. Hinton, T. J. Cloonan, F. B. McCormick, A. L. Lentine, and F. A. P. Tooley, "Free space digital optical systems," *Proceedings of the IEEE*, vol. 82, no. 11. pp. 1632–1649, 1994.

[8] G. Giovanni, "Semiconductor Devices for High-speed Optoelectronics." Cambridge University Press, New York, 2009.

[9] D. Patel, "Design, analysis, and performance of a silicon photonic traveling wave Mach-Zehnder modulator," McGill University, 2014.

[10] E. Hecht, *Optics*, 4th ed. Addison Wesley, 2003.

[11] M. Menard, "Integrated Fabry-Perot optical space switches," McGill University, Canada, 2009.

[12] B. E. A. Saleh, M. C. Teich, and B. E. Saleh, *Fundamentals of Photonics*, vol. 22. Wiley New York, 1991.

[13] A. Yariv, *Photonics: Optical Electronics in Modern Communications*, 6th ed. New York: Oxford University Press, 2007.

[14] H. Daussy, R. Dumanchin, and O. de Witte, "Fabry-Perot with short pulse lasers: spectral selection and spectral analysis in dye lasers," *Appl. Opt.*, vol. 17, no. 3, pp. 451–458, 1978.

[15] J. Liu, *Photonic Devices*. Cambridge: Cambridge University Press, 2005.

[16] B. G. Lee *et al.*, "Comparison of ring resonator and Mach-Zehnder photonic switches integrated with digital CMOS drivers," *2010 23rd Annu. Meet. IEEE Photonics Soc. PHOTINICS 2010*, no. dc, pp. 327–328, 2010.

Chapter 4

Theory and Design of Integrated Silicon Photonics Loop-Mirror Modulator

4.1 Introduction

This chapter describes the design and analysis of the loop-mirror modulator (LMM). The idea of silicon-based integrated LMM was inspired primarily by previous work on fiber loop-mirrors [1]–[5] developed for nonlinear optical processing. A schematic of the LMM design is given in Figure 1. A loop-mirror is made of a power divider with two outputs on one side of the divider connected by a loop of fiber or waveguide. Light at the input of the loop-mirror is split in two, and each half travels in the opposite direction along the loop. In nonlinear applications, the relative phase between the two halves of the initial signal is controlled by the power of a second signal that propagates in only one direction. The impact of the addition of the loop-mirror is to reduce the change in coupling ratio required to obtain complete modulation with the MZI. By varying the coupling ratio from 50% to 100% it is possible to change the device from a transmission device to a reflection device. In Figure 1, the length of the loop piece is L_1, and the length of the power divider part is L_2.

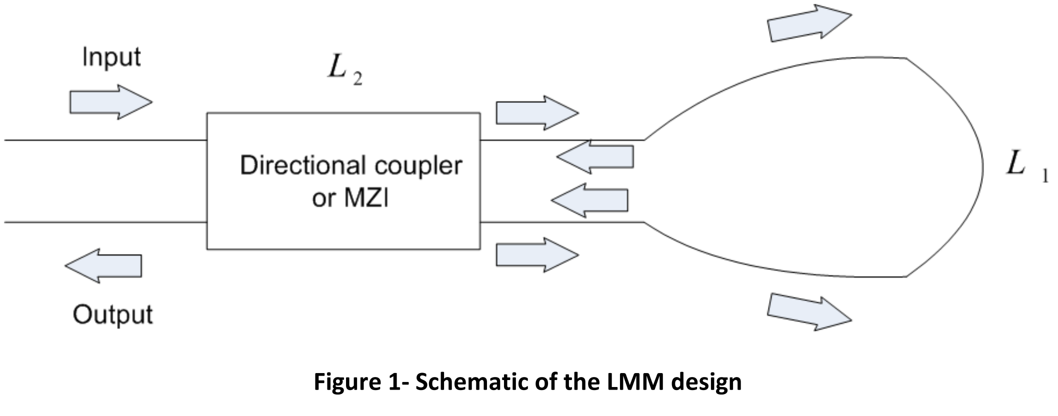

Figure 1- Schematic of the LMM design

4.2 Discussions on design and implementation of the power divider

To design an integrated LMM, as described in Section 4.1, it is necessary to control the coupling ratio in the power divider via external actuation. The two main options to implement an integrated controllable power divider are to use either a tunable directional coupler or an MZI. At the beginning of the design process, we looked at the possibility of using a directional coupler for the power divider part of LMM. We started the process by going through the details of the directional coupler's design, modeling and numerical estimations. The modification of different parameters, such as the length of the directional coupler, the gap between the straight waveguides, as well as the width and height of the waveguides are considered. We find out that if an LMM is implemented with a directional coupler at the power divider part, the tunability of the modulator is too small to be detected by our available measurement equipment. These investigations are also in agreement with the previously reported tunability results of the directional coupler in [6], [7]. Eventually we concluded that the tunable directional coupler is not a good candidate for the power divider part of LMM. The MZI is our next option for the design of the power divider part in LMM. The tunability of MZI was good enough to meet our design expectations which are explained in Section 4.2.2.

The implemented loop-mirror MZI consists of two identical 3dB couplers that are cascaded to create an MZI, with the output waveguides connected to form a loop-mirror. Assuming that the electrodes can be analyzed in the lumped regime, when no voltage is applied to the MZI arms, after the forward propagation all of the input power appears on the lower arm of the loop, and therefore in the backward direction it is sent through the upper port of the MZI toward the through port. To reflect light toward the input, the input power must be distributed equally between the upper and lower arm of the loop-mirror. A phase shift is required to transfer all the power to the input port of the LMM to achieve efficient intensity modulation of the signal. The phase shift needed to achieve complete modulation is provided by applying a voltage to MZI arms, which actuate the modulator [5]. The analysis and calculation of the length of the 3dB coupler and the length of the MZI appear in detail in Section 4.2.1 and Section 4.2.2 respectively.

4.2.1 Design and analysis of 3dB directional coupler

There are two 3dB directional couplers in the cascaded MZI that is used in the power divider part of the LMM. In this section, the analytical method to design the effective length of these couplers is discussed. The schematic of a directional coupler is shown in Figure 2. The transfer matrix and related parameters are required to model a directional coupler. Here the transmitted light is shown by t, and the coupled light by κ. The 3dB coupler length is L_C. The input light has an initial phase of φ.

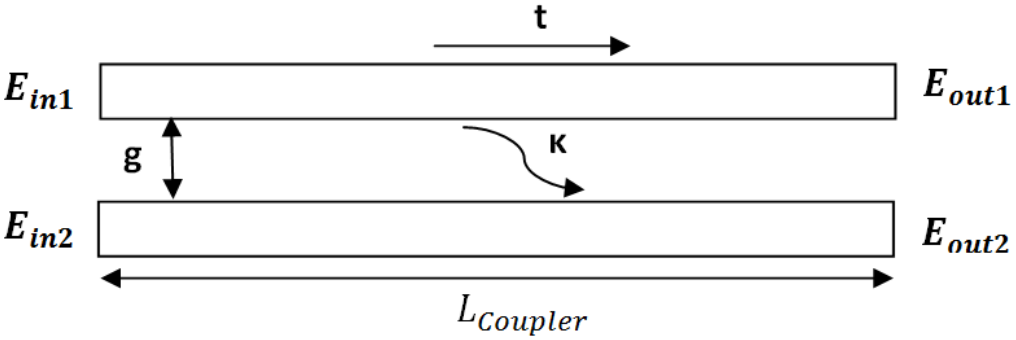

Figure 2- Schematic of a directional coupler

Accordingly, the transfer matrix of the directional coupler can be derived as

$$\begin{bmatrix} E_{out1} \\ E_{out2} \end{bmatrix} = \begin{bmatrix} t & \kappa \\ \kappa & t \end{bmatrix} \begin{bmatrix} E_{in1} \\ E_{in2} \end{bmatrix} \tag{1}$$

$$t = \cos(CL_C)\, e^{-j\varphi} \tag{2}$$

$$\kappa = \sin(CL_C)\, e^{-j\varphi} e^{-j\frac{\pi}{2}} \tag{3}$$

$$C = \frac{\pi \Delta n}{\lambda} \tag{4}$$

where C is the coupling constant and Δn is the supermode refractive index. The value for Δn is obtained by supermode simulation [7] and using Lumerical MODE solutions software [8]. The methodology of MODE solution in this software is based on solving Maxwell's equations and extracting a set of eigenmodes. The operating modes are computed by dividing the geometry into multiple cells and then solving for the modes at the interface between adjacent cells. Eventually, using this tool makes it possible to gain the final field profile. In our simulations, we use a rib waveguide structure for the LMM with values listed in the Table 1. Two different cases should be considered in supermode simulations. The first case (Fig. 3) is symmetric and this case is about the transmission of light through both straight waveguides of a directional coupler. The second case (Fig. 4) is anti-symmetric and this case is about the coupling of light from one of the straight waveguides to the other straight waveguide of a directional coupler. The difference in the effective refractive indices for these two cases is the supermode refractive index and it is used in the Equations (1) - (4) to define the 3dB coupling length L_C of a directional coupler.

Table 1 –Values used in supermode simulation of a directional coupler

BOX (buried oxide)	2.0 μm
waveguide width (w)	0.5 μm
waveguide height (h)	0.22 μm
central wavelength (λ_c)	1.55 μm
slab height	0.09 μm
cladding	Air (n = 1)

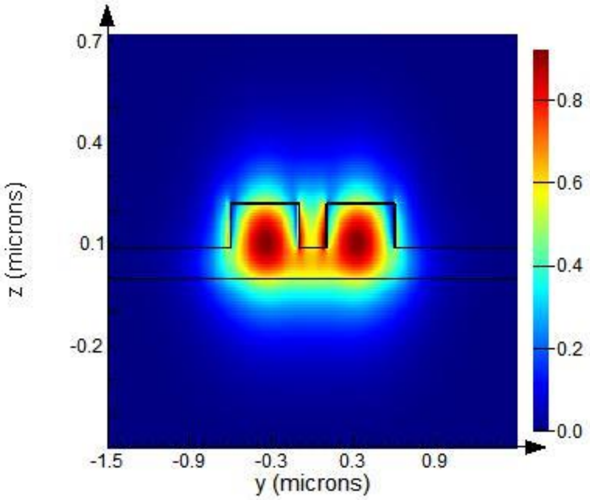

Figure 3 - Symmetric supermode, n_{sym}= 2.5925

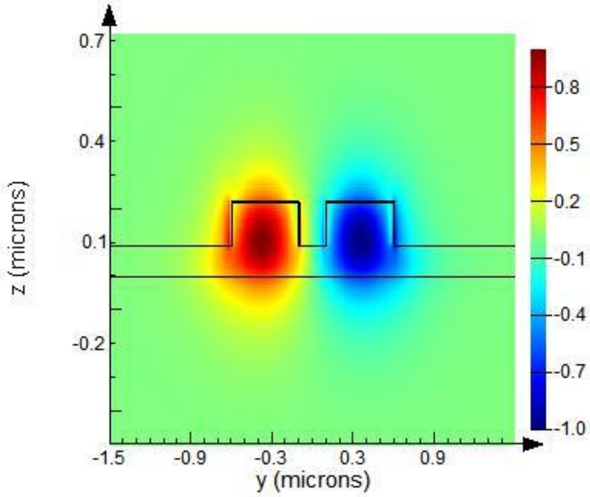

Figure 4 - Anti-symmetric supermode, n_{asym}= 2.5416

If the directional coupler is considered lossless, then the relationship between t and κ is

$$t^2 + \kappa^2 = 1 \tag{5}$$

In the case of 50% power transfer of the 3dB coupler,

$$t^2 = \kappa^2 = \frac{1}{2} \text{ and } |t| = |\kappa| = \frac{1}{\sqrt{2}} \tag{6}$$

and accordingly

$$\sin(CL_C) = \frac{1}{\sqrt{2}} \text{ or } CL_C = \frac{\pi}{4} \tag{7}$$

From the supermode simulations above, the change in the supermode refractive index is

$$\Delta n = n_{symmetric} - n_{anti-symmetric} = 0.1809 \tag{8}$$

Equations (4), (7) and (8) results in

$$L_C = L_{3dB} = 7.61\ \mu m \tag{9}$$

4.2.2 Design and analysis of MZI

As discussed previously, the MZI is placed as the power divider part of the LMM. The length of MZI arms should be designed properly to reach the desired phase shift in the modulator. In this section, the analytical method to model the effective length of MZI arms is presented. The schematic of an MZI is shown in Figure 5. Here L_{3dB} is the length of the 3dB couplers, and L_{MZI} is the length of the MZI arm. The transfer matrix Equations of the MZI are shown in Equations (10) -(20). The matrix for the 3dB coupler is expressed as the parameter *C*, the MZI matrix as M_{MZI}, and the input matrix as $\begin{bmatrix} E_{in1} \\ E_{in2} \end{bmatrix}$. Then, the expression for the output can be given by $\begin{bmatrix} E_{out1} \\ E_{out2} \end{bmatrix}$.

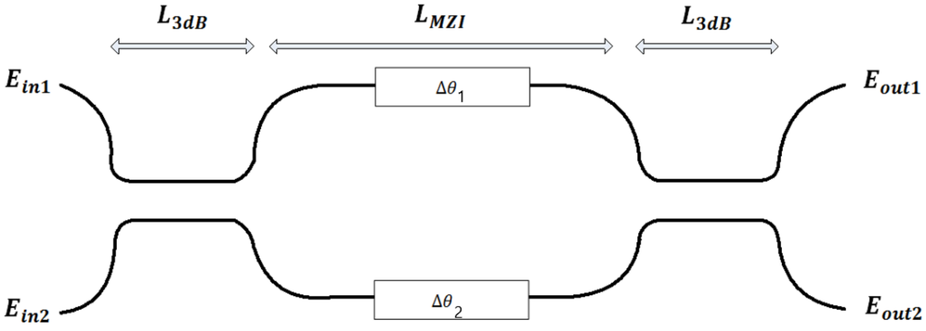

Figure 5- Schematic of a conventional MZI

$$C = \begin{bmatrix} \frac{\sqrt{2}}{2} e^{-j\varphi} & -j\frac{\sqrt{2}}{2} e^{-j\varphi} \\ -j\frac{\sqrt{2}}{2} e^{-j\varphi} & \frac{\sqrt{2}}{2} e^{-j\varphi} \end{bmatrix} \tag{10}$$

$$M_{MZI} = \begin{bmatrix} e^{-j(\theta+\Delta\theta_1)} & 0 \\ 0 & e^{-j(\theta+\Delta\theta_2)} \end{bmatrix} \tag{11}$$

In the above matrices, φ is the initial phase of the 3dB coupler, θ is the initial phase shift of the MZI, $\Delta\theta_1$ is the phase shift in the top arm of MZI, and $\Delta\theta_2$ is the phase shift in the bottom arm of MZI caused by voltage applied to them. The relationships between these angles and the geometry of the modulator are:

$$\varphi = \frac{2\pi}{\lambda} n \, L_{3dB} \tag{12}$$

$$\theta = \frac{2\pi}{\lambda} n \, L_{MZI} \tag{13}$$

Since the top and bottom arms are assumed to have equal lengths, it follows that

$$\Delta\theta_1 = \Delta\theta_2 = \Delta\theta = \frac{2\pi}{\lambda} \Delta n_{eff} L_{MZI} \tag{14}$$

$$\begin{bmatrix} E_{out1} \\ E_{out2} \end{bmatrix} = C.\, M_{MZI}.\, C. \begin{bmatrix} E_{in1} \\ E_{in2} \end{bmatrix} \tag{15}$$

where n is the effective refractive index of the optical waveguide, and Δn_{eff} is the change of effective refractive index in the MZI arm caused by the applied voltage. The matrix for the output of the MZI is

$$\begin{bmatrix} E_{out1} \\ E_{out2} \end{bmatrix} = e^{-j(2\varphi+\theta)} \begin{bmatrix} \frac{1}{2} - \frac{1}{2} e^{-j\Delta\theta} & \frac{-j}{2} - \frac{j}{2} e^{-j\Delta\theta} \\ \frac{-j}{2} - \frac{j}{2} e^{-j\Delta\theta} & \frac{-1}{2} + \frac{1}{2} e^{-j\Delta\theta} \end{bmatrix} \begin{bmatrix} E_{in1} \\ E_{in2} \end{bmatrix} \tag{16}$$

For simplification, Equation (17) can be substituted in Equation (16) as

$$\cos\frac{\Delta\theta}{2} = \frac{e^{j\frac{\Delta\theta}{2}} + e^{-j\frac{\Delta\theta}{2}}}{2} \quad , \quad \sin\frac{\Delta\theta}{2} = \frac{e^{j\frac{\Delta\theta}{2}} - e^{-j\frac{\Delta\theta}{2}}}{2j} \tag{17}$$

$$\begin{bmatrix} E_{out1} \\ E_{out2} \end{bmatrix} = e^{-j(2\varphi+\theta)} \times (-j)\, e^{-j\Delta\theta} \begin{bmatrix} -\sin\frac{\Delta\theta}{2} & \cos\frac{\Delta\theta}{2} \\ \cos\frac{\Delta\theta}{2} & \sin\frac{\Delta\theta}{2} \end{bmatrix} \begin{bmatrix} E_{in1} \\ E_{in2} \end{bmatrix} \tag{18}$$

All of the phase-related terms can be summarized in a constant value of A shown as

$$A = -je^{-j(2\varphi+\theta+\Delta\theta)} \tag{19}$$

Finally, the output matrix for an MZI matrix is

$$\begin{bmatrix} E_{out1} \\ E_{out2} \end{bmatrix} = A \begin{bmatrix} -\sin\frac{\Delta\theta}{2} & \cos\frac{\Delta\theta}{2} \\ \cos\frac{\Delta\theta}{2} & \sin\frac{\Delta\theta}{2} \end{bmatrix} \begin{bmatrix} E_{in1} \\ E_{in2} \end{bmatrix} \tag{20}$$

The study of efficient biasing in [9] demonstrates that the push-pull MZI configuration shown in Figure 6, leads to lower power consumption than conventional MZI modulators. The push-pull design only requires one-half of the PN junction capacitance. This is an advantage, given that the capacitance is the limiting factor in reverse bias modulators. The push-pull design also reduces the chirp from modulation-induced effect.

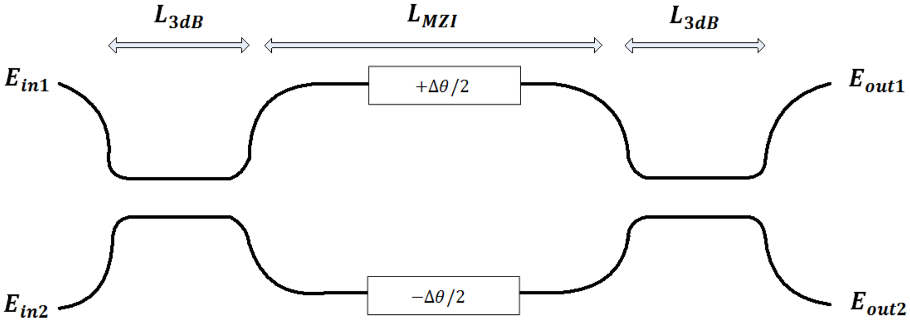

Figure 6- Schematic of the push-pull MZI used as the power divider part in the LMM design

The push-pull MZI model is used as the power divider part in the LMM design in which the phase shift for the top arm is $\frac{\Delta\theta}{2}$ and the phase shift for the bottom arm is $-\frac{\Delta\theta}{2}$. By substituting these values in Equation (11) the output matrix for push-pull MZI can be derived as

$$\begin{bmatrix} E_{out1} \\ E_{out2} \end{bmatrix} = B \begin{bmatrix} \sin\frac{\Delta\theta}{2} & \cos\frac{\Delta\theta}{2} \\ \cos\frac{\Delta\theta}{2} & -\sin\frac{\Delta\theta}{2} \end{bmatrix} \begin{bmatrix} E_{in1} \\ E_{in2} \end{bmatrix} \tag{21}$$

where all of the phase-related terms can be summarized as a constant value of B shown as

$$B = -je^{-j(2\varphi+\theta)} \tag{22}$$

The only differences between the output matrix of a conventional MZI in Equation (20) and the output matrix of a push-pull MZI in Equation (21) are the phase-related constant values of A and B. For amplitude modulation, which is the focus of this chapter, the phase-related differences of two electrode designs are ignorable.

4.3 Operating principles for LMM

In Section 4.1, the LMM is described as two identical 3dB couplers that are cascaded to create an MZI, with the output waveguides connected to form a loop-mirror. A schematic of the designed LMM is shown in Fig. 7. In this section, the analysis and design of LMM are presented. To propagate through the LMM, the propagating light must go through the two couplers, twice through the waveguides of the MZI, and once around the loop-mirror.

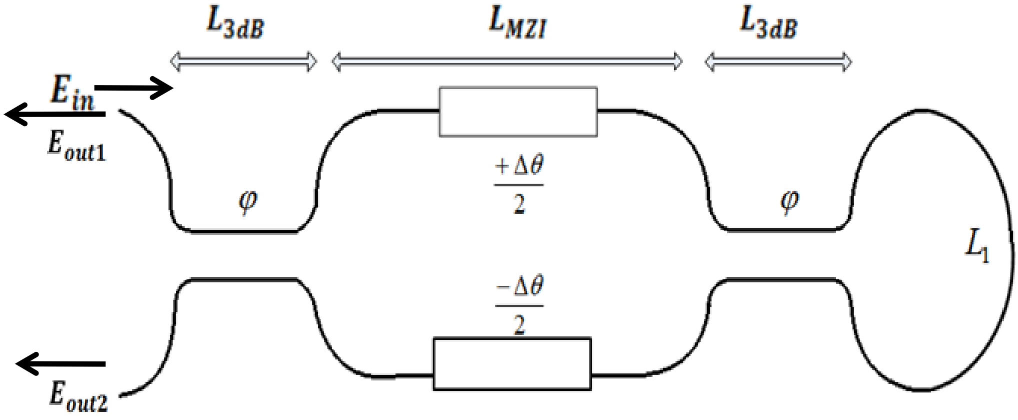

Figure 7- Schematic of LMM with MZI as power divider

The matrix for an MZI with push-pull electrode configuration is given as M_{P-MZI}, the loop matrix is given as L, in which β is the propagation constant of the waveguides, and $L_1$is the length of the loop. The matrix for 3dB coupler is given in Equation (10). The input matrix is $\begin{bmatrix} E_{in} \\ 0 \end{bmatrix}$, and the expression for the output is given by $\begin{bmatrix} E_{out1} \\ E_{out2} \end{bmatrix}$.

$$M_{P-MZI} = \begin{bmatrix} e^{-j(\theta + \frac{\Delta\theta}{2})} & 0 \\ 0 & e^{-j(\theta - \frac{\Delta\theta}{2})} \end{bmatrix} \tag{23}$$

$$L = \begin{bmatrix} e^{-j\beta L_1} & 0 \\ 0 & e^{-j\beta L_1} \end{bmatrix} \tag{24}$$

The transfer matrix for LMM can be achieved from Equation (25) as

$$\begin{bmatrix} E_{out1} \\ E_{out2} \end{bmatrix} = C. M_{P-MZI}. C. L. M_{P-MZI}. C. \begin{bmatrix} E_{in} \\ 0 \end{bmatrix} \tag{25}$$

$$\overrightarrow{E_{in}} = \begin{bmatrix} E_{in} \\ 0 \end{bmatrix} \tag{26}$$

$$E_{out1-LMM} = E_{in} e^{-j\beta L_1} \left(-\sin^2 \frac{\Delta\theta}{2} + \cos^2 \frac{\Delta\theta}{2} \right) = E_{in} e^{-j\beta L_1} \cos \Delta\theta \tag{27}$$

In the LMM, the length of 3dB couplers is known from Section 4.2.1 and Equation (9). To design the length of the MZI arms, we need to calculate the effective refractive index and the change in refractive index of optical waveguide due to EO effect. For this reason, the Lumerical MODE [8] and DEVICE [10] solutions software are used. The methodology of DEVICE solution in this software is based on solving Poisson's equation and the drift-diffusion equations to model the steady-state and transient behavior of electrons and holes in the PN junction. A schematic of the simulated rib waveguide and its dimensions are shown in Figure 8.

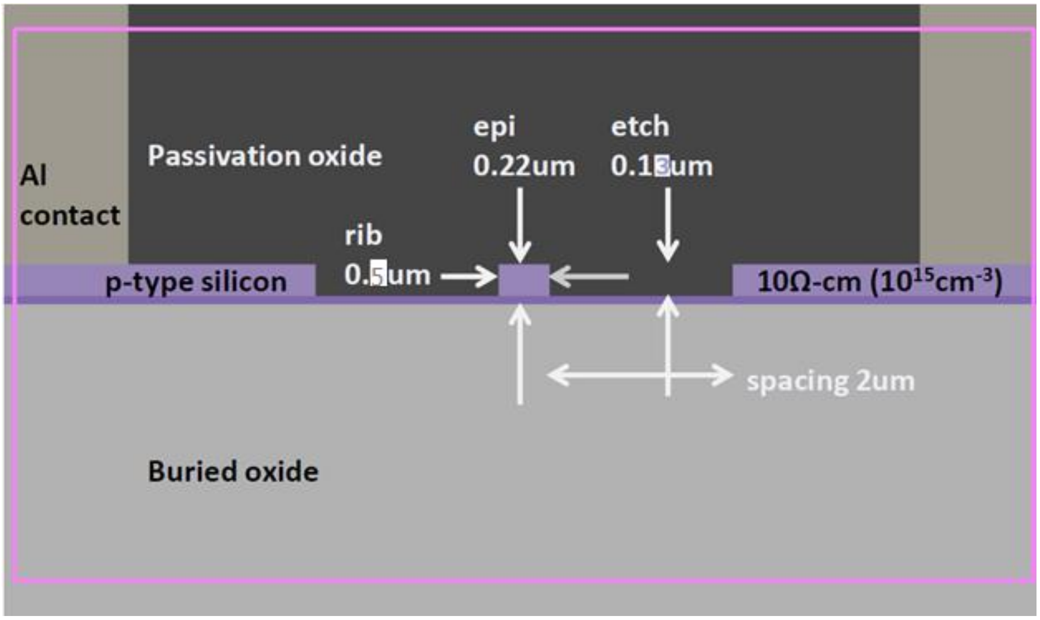

Figure 8- Schematic of the simulation parameters

The simulated results and the related graphs are illustrated in Figure 7 and Figure 8. When bias voltage becomes more negative, the number of circulating charges increases (Figure 9).

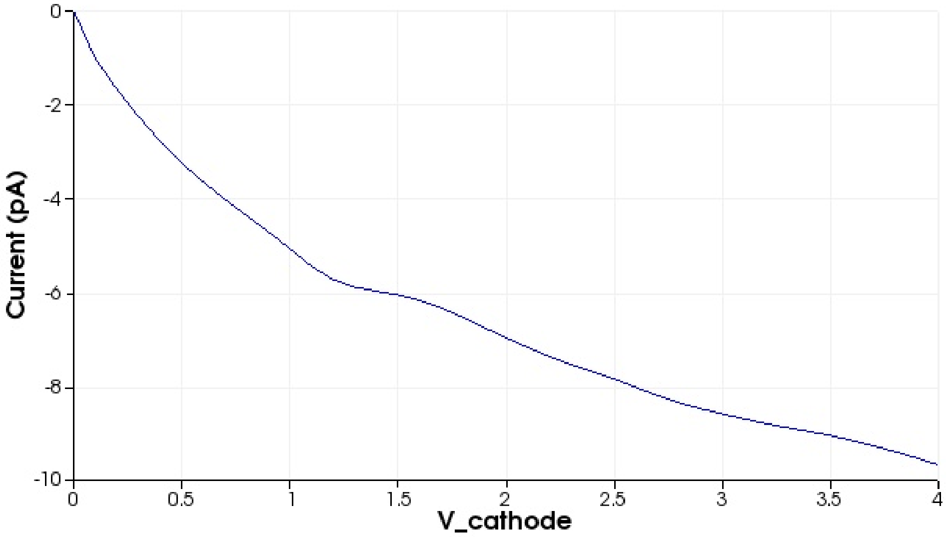

Figure 9- Applied voltage vs. current in the reverse bias PN junction

When the applied voltage in the reverse bias increases, the change in the effective refractive index of the PN junction increases. This can be observed in Figure 10.

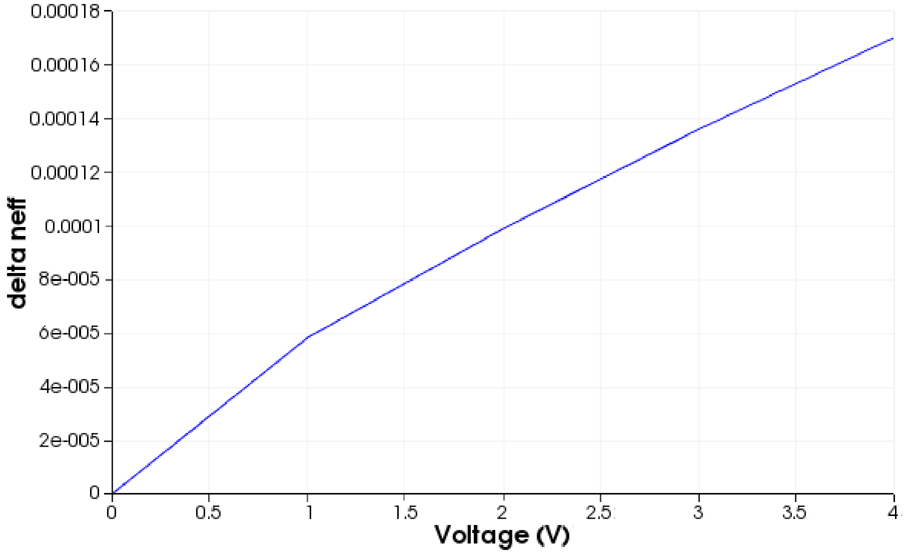

Figure 10- Results of EO effect for applied voltage relative to Δn_{eff} in the optical waveguide

When LMM is in the "OFF" state the LMM is supposed to have no transmission and the relative amplitude modulation is zero; that means $\frac{|E_{out-LMM}|}{E_{in}} = 0$. As a result, in Equation (27) we have $\cos \Delta\theta = 0$, and therefore the maximum phase shift is $\Delta\theta = \frac{\pi}{2}$. By using the results for Δn_{eff} from the graph in Fig. 9 and Equation (14), the value for the phase shift can be used to calculate the length of the MZI arm as the maximum active phase shift region. In our design the MZI is considered symmetric (i.e. both MZI arms have similar dimensions), and $\lambda = 1.55\ \mu m$. Different values for L_{MZI} are calculated based on the differential value of the effective refractive index regarding to the applied voltage (Figure 8). The results are summarized in Table 2.

Table 2 – Results for the length of MZI arm according to EO effect

Applied voltage (V)	Δn_{eff}	L_{MZI} (mm)
2.0	1.0×10^{-4}	3.875
4.0	1.7×10^{-4}	2.279

Because of pre-defined size of optical chips and fabrication limitations for the dimension of designed devices, we decided to select a 4V actuation voltage and the length of the MZI arm as

$$L_{MZI} = 2.279 \text{ mm} \tag{28}$$

When the LMM is in the "ON" state, it is supposed to have maximum transmission and the relative amplitude modulation is one; that means $\frac{|E_{out-LMM}|}{E_{in}} = 1$. As a result, in Equation (27) we have $\cos\Delta\theta = 1$, and the minimum phase shift is $\Delta\theta = 0$. By using this value for the phase shift and Equation (14) we obtain $\Delta n_{eff} = 0$. This proves that there is no modulation when the LMM is in the "ON" state. The results of the modulation state and the related modulation power and phase shifts are summarized in Table 3.

Table 3- Modulation characteristics of MZI for LMM design

Modulation state	Relative amplitude modulation	Phase shift
OFF	0	π/2
ON	1	0

The normalized output power of an LMM and a standard MZI-based on Equations (21) and (27) are plotted in Figure 11.

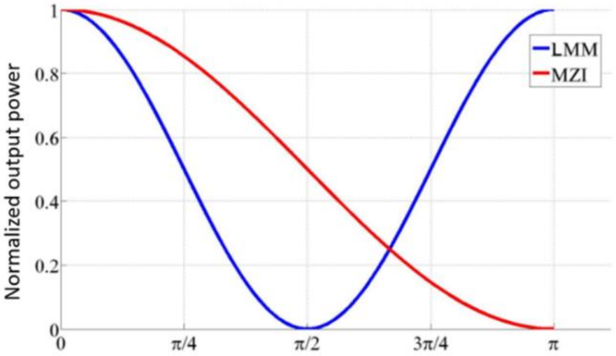

Figure 11- Phase shift comparison of standard MZI and loop-mirror MZI

From Figure 11 it is possible to compare the operational characteristics of LMM and standard MZI. The physical explanation is that in a phase shift period between zero and π, the LMM can sweep through 1-0-1 levels but the regular MZI only sweeps through 1-0 levels. To achieve a complete modulation LMM requires smaller phase shifts than in a standard MZI with similar actuation voltage and equivalent dimensions. This translates into a decrease of the voltage required to actuate the modulator; consequently, the device has lower power consumption. The LMM requires one-half the phase shift and one-quarter of the actuation power of an MZI without the loop-mirror, as the power consumption is related to the square of the driving voltage. In other words, the addition of the loop-mirror causes a significant reduction in the coupling ratio required to obtain complete modulation with the MZI – it drops from 100% to 50%. As it will be explained in detail in Section 4.4, these conclusions are only valid for an LMM with the lumped electrode regime. The difference between the lumped model and the traveling wave model, as well as the critical length for the lumped LLM have been explained in Section 5.5.

4.4 Operating principles for LMM with a traveling wave (TW) electrode configuration

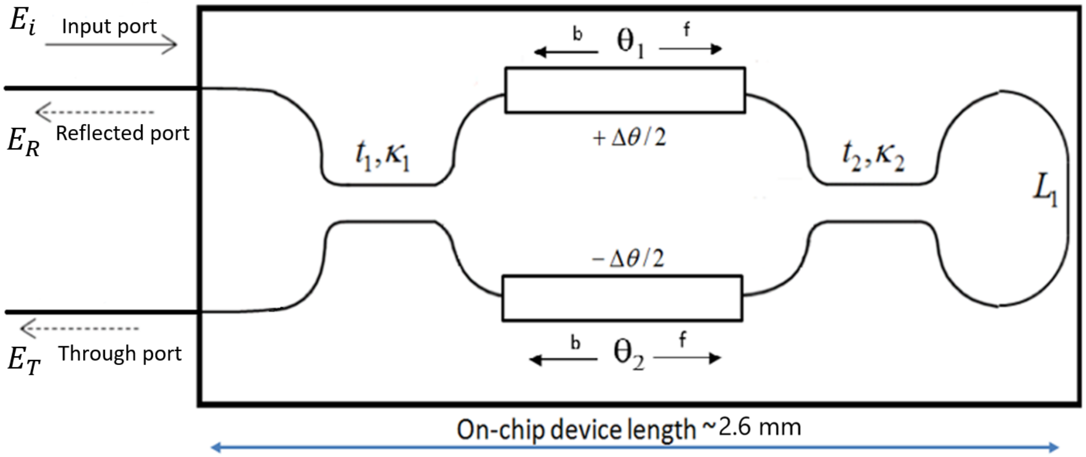

Figure 12- Schematic of the fabricated LMM

The optical transfer function of the series push-pull LMM is obtained as follows. In the LMM, the arms of the MZI have the same length, and, thus, the device is symmetric. Assuming lossless propagation in the couplers, if the coupler matrix is expressed as parameter *C* from Equation (10), the loop matrix as *L* from Equation (24), the MZI matrix for forward propagation as M_f, the MZI matrix for backward propagation as M_b, and the input as vector $\overrightarrow{E_{in}}$ from Equation (26), then the expression of the output is given by the vector $\overrightarrow{E_{out-LMM}}$ as:

$$M_f = \begin{bmatrix} e^{-j(\theta+\theta_{1f})} & 0 \\ 0 & e^{-j(\theta+\theta_{2f})} \end{bmatrix} \tag{29}$$

$$M_b = \begin{bmatrix} e^{-j(\theta+\theta_{1b})} & 0 \\ 0 & e^{-j(\theta+\theta_{2b})} \end{bmatrix} \tag{30}$$

$$\overrightarrow{E_{out-LMM}} = \begin{bmatrix} E_R \\ E_T \end{bmatrix} \tag{31}$$

$$\overrightarrow{E_{out-LMM}} = \mathrm{C}.M_b.\mathrm{C}.\mathrm{L}.\mathrm{C}.M_f.\mathrm{C}.\overrightarrow{E_{in}} \tag{32}$$

where β is the propagation constant of the waveguides, and L_1 is the length of the loop. The angle θ is the fixed phase difference between the MZI arms from Equation (13), θ_{1f} and θ_{2f} are the phase shifts experienced by the forward going signals due to the modulation of the effective refractive index of the upper and lower MZI arms, respectively, and similarly θ_{1b} and θ_{2b} are the phase shifts experienced by the backward propagating signals due to the modulation of the effective refractive index of the upper and lower MZI arms. Due to the traveling-wave electrodes regime design and discussions for velocity match between optical and RF signals in forward and backward propagation, the phase shifts in Equations (29) and (30) are different from phase shift in Equation (23) which is presenting the lumped electrode regime design of the LMM. The angle φ is the fixed phase difference in the 3dB couplers from Equation (12). L_{MZI} is the length of the phase-shifter in the MZI, and L_{3dB} is the length of the 3dB couplers. The difference between a traveling-wave regime and a lumped regime and the critical length will be explained in detail in Section 5.5.

The output of the LMM based on the phase shift accumulated in each arm of the MZI, as shown in Figure 12, can be obtained by the following calculations. For the upper arm of the MZI, the phase shift is defined by $\theta_1 = \theta_{1b} + \theta_{1f}$. Similarly, for the bottom arm of the MZI the total phase shift of the signal is defined as $\theta_2 = \theta_{2b} + \theta_{2f}$. By considering the phase shift in the upper and bottom arms together as shown in Figure 12, the amplitude of the output electric field at the reflected port of the LMM can be expressed as:

$$E_{R-LMM}(\theta_1, \theta_2) = -\tfrac{1}{2} e^{-jL_1\beta} \left(e^{-j(\theta_{1b}+\theta_{1f})} - e^{-j(\theta_{2b}+\theta_{2f})} \right) \tag{34}$$

To evaluate the modulation efficiency of the LMM, it is important to understand the EO response of the modulator as a function of frequency. To obtain this, we must first calculate the output of the LMM based on the phase shift accumulated in each arm of the MZI, as shown in Equation (34). The frequency dependent electrical field obtained at the output is given by:

$$E_{R-LMM}(f, \theta_1, \theta_2) = -\frac{1}{2} e^{-jL_1\beta} \left(e^{-j\left(\theta_{1b}\times H_b(f) + \theta_{1f}\times H_f(f)\right)} - e^{-j\left(\theta_{2b}\times H_b(f) + \theta_{2f}\times H_f(f)\right)} \right) \tag{35}$$

where $H_f(f)$ is the phase response of the forward propagating signal, and $H_b(f)$ is the phase response of the backward propagating signal. The phase responses are derived based on [11], [12], and for each direction, they are given by:

$$H_f(f) = e^{\frac{-\alpha L_2}{2}} \left[\frac{\sinh^2\left(\frac{\alpha L_2}{2}\right) + \sin^2\left(\frac{\omega \Delta v_{co} L_2}{2}\right)}{\left(\frac{\alpha L_2}{2}\right)^2 + \left(\frac{\omega \Delta v_{co} L_2}{2}\right)^2} \right]^{\frac{1}{2}}, \quad \Delta v_{co} = \frac{\omega}{c} \times \left| \left(\frac{n_m - n_g}{n_m \times n_g} \right) \right| \tag{36}$$

$$H_b(f) = e^{\frac{-\alpha L_2}{2}}[\frac{sinh^2\left(\frac{\alpha L_2}{2}\right)+sin^2\left(\frac{\omega \Delta v_{counter} L_2}{2}\right)}{\left(\frac{\alpha L_2}{2}\right)^2+\left(\frac{\omega \Delta v_{counter} L_2}{2}\right)^2}]^{\frac{1}{2}}, \quad \Delta v_{counter} = \frac{\omega}{c} \times \left|\frac{n_m+n_g}{n_m \times n_g}\right| \qquad (37)$$

where α is the total propagation loss, c is the speed of light in free space, L_2 is the length of phase shift region (length of MZI arm), n_m is the refractive index of the microwave drive signal, n_g is the refractive group index of the optical signal, Δv_{co} is the mismatch between the optical group velocity and the microwave phase velocity of the co-propagating signals, $\Delta v_{counter}$ is the mismatch between the optical group velocity and the microwave phase velocity of the counter-propagating signals, and ω is the angular frequency. Here, n_m is a frequency dependent parameter and can be estimated from the Lumerical INTERCONNECT software [13] as $n_m \cong 4$ for ease of simulation, and $n_g = 3.8$ is obtained from simulations using Lumerical MODE solutions software [8].

The frequency dependent EO response of a TW-MZM with a configuration equivalent to the one of the LMM for signals propagating in the forward (co-propagating, blue line) and backward (counter-propagating, red line) directions are presented in Figure 13. In order to obtain the EO response of the LMM, the forward propagation response and the backward propagation response are to be added up. This is done by inserting Equations (36) and (37) in Equation (35). As a result, we obtain the blue line in Figure 14. The EO response of an MZM without a loop-mirror but driven by the same voltage as the LMM is also included in Figure 14 (red line).

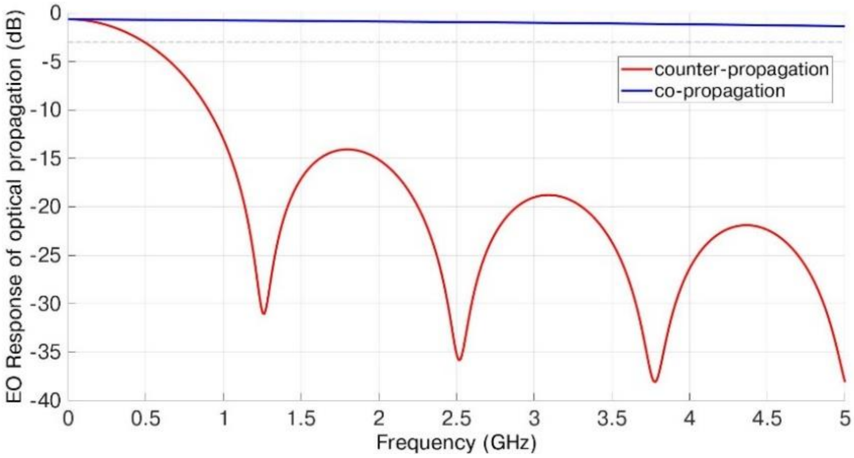

Figure 13 – EO bandwidth of a standard MZM (blue line) response for co-propagating optical and microwave signals' (red line) response for counter-propagating signals.

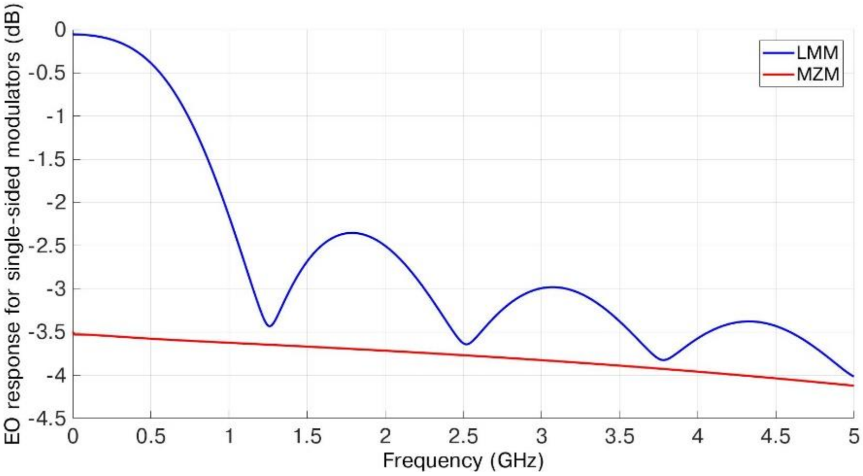

Figure 14 – (blue line) EO response for an LMM combining co-propagation and counter-propagation (red line) responses for a standard MZM driven by the same voltage as the LMM.

The EO modulation response rolls off very quickly at around 1 GHz in counter-propagation; thus, at higher frequencies the optical signal is only modulated when it propagates in the forward direction. Therefore, at high frequencies, the LMM displays modulation efficiency comparable to that of an MZI without a loop-mirror when both are modulated by the same drive voltage. However, as can be seen in Figure 12, for the same drive voltage, the LMM can provide twice the modulation depth (extinction ratio) for frequencies below 1 GHz. This corresponds to the frequency range over which the LMM electrodes can be considered as lumped electrodes regime instead of

TW electrodes regime. Moreover, since the propagation time inside the loop-mirror is negligible, in this regime, the LMM will efficiently modulate the signal in both co- and counter-propagation. The difference between the traveling-wave regime and the lumped regime, as well as the critical length for the lumped LMM will be explained in detail in Section 5.5.

The EO bandwidth of LMM is investigated experimentally by using a lightwave component analyzer (LCA). The schematic of the setup used to verify the device under the test (DUT) is shown in Figure 15. The DUT includes the LMM with 50 Ω termination. The electrical frequency is swept in order to achieve the EO response which is the correlation between electrical and optical sweeps.

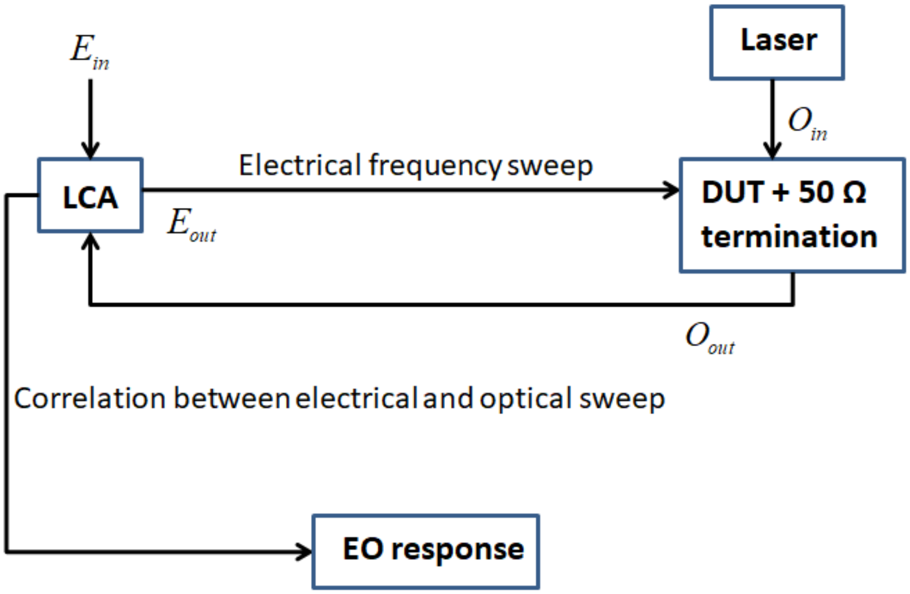

Figure 15- Schematic of EO bandwidth measurement setup

The EO response of LMM, which can be observed in Figure 16, also correlates at 5 volts with the theoretical results explained in Figure 14 (rolls off around 1 GHz).

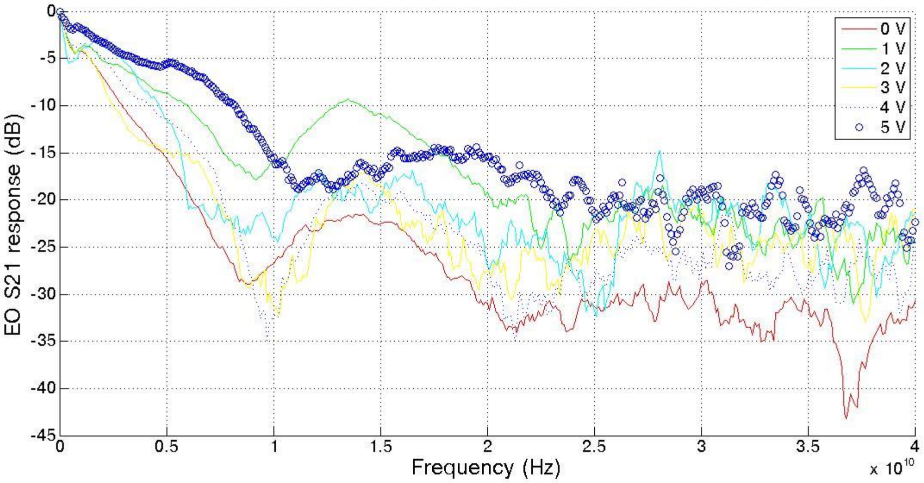

Figure 16- Experimental results for EO bandwidth of LMM

An idea which will be investigated elaborately in future works is a revised LMM design that contains shorter electrodes and therefore a smaller phase shift region. The lumped model for LMM will provide higher modulation speed with lower power consumption as discussed in Section 4.3. Furthermore, as reported in [2], [3], [14], the forward propagating light in the MZI has a good velocity match with the RF signal of the driver in the lumped electrode regime. To implement LMM, two different electrode configurations in TW electrode regime for reverse-biased PN junction were designed and fabricated. The first TW configuration is series push-pull; it is used to develop LMM with OOK modulation, as described in Chapter 5. The second TW configuration is dual-drive; it is used to demonstrate LMM with DPSK modulation, will be described in Chapter 6.

References

[1] D. B. Mortimore, “Fiber loop reflectors.,” *J. Light. Technol.*, vol. 6, no. 7, pp. 1217–1224, 1988.

[2] C. A. Millar, D. Harvey, and U. Paul, “Fiber reflection Mach-Zehnder interferometer,” *Opt. Commun.*, vol. 70, no. 4, pp. 1–5, 1989.

[3] G. Dickinson, D. a Chapman, and D. a Gorham, “Properties of the fiber reflection Mach-Zehnder interferometer with identical couplers.,” *Opt. Lett.*, vol. 17, no. 17, pp. 1192–1194, 1992.

[4] K. P. Oakley, N. M. O’Sullivan, C. D. Hussey, and T. A. Birks, “Miniature high-performance fiber loop reflector,” *Electron. Lett.*, vol. 27, no. 25, 1991.

[5] I. Aryanfar, L. Kok-Sing, W.-Y. Chong, S. Wadi Harun, and H. Ahmad, “Add-drop filter based on microfiber Mach-Zehnder/Sagnac interferometer,” *IEEE J. Quantum Electron.*, vol. 48, no. 11, pp. 1411–1414, 2012.

[6] J. C. Mikkelsen, W. D. Sacher, and J. K. S. Poon, “Dimensional variation tolerant silicon-on-insulator directional couplers,” *Opt. Express*, vol. 22, no. 3, pp. 3145–3150, 2014.

[7] L. Chrostowski and M. Hochberg, *Silicon Photonics Design: From Devices to Systems*. Cambridge: Cambridge University Press, 2015.

[8] “Lumerical MODE Solutions.” [Online]. Available: www.lumerical.com.

[9] P. Dong, “Low voltage silicon photonic modulators,” *IEEE Photonics Soc. Summer Top. Meet. Ser. PSST 2012*, vol. 1, pp. 130–131, 2012.

[10] “Lumerical DEVICE Solutions.” [Online]. Available: www.lumerical.com.

[11] A. Samani *et al.*, “A low-voltage 35-GHz silicon photonic modulator-enabled 112-Gb/s transmission system,” *IEEE Photonics J.*, vol. 7, no. 3, 2015.

[12] D. Patel, “Design, analysis, and performance of a silicon photonic traveling wave Mach-Zehnder modulator,” McGill University, 2014.

[13] “Lumerical INTERCONNECT Solutions.” [Online]. Available: www.lumerical.com.

[14] B. Desruelle, E. Desurvire, and S. Bigo, “Analysis of the polarization group velocity dispersion effect in polarization-independent nonlinear-optical loop-mirror demultiplexers,” *Opt. Lett.*, vol. 20, no. 5, pp. 516–518, 1995.

Chapter 5

Measurement Results of Loop-Mirror Modulator in On-Off Keying Modulation

5.1 Introduction

The analytical model of the LMM was previously described in Chapter 4. In this chapter, the measurement method and characterization results for the silicon-based LMM are presented. To our knowledge it is a novel approach of EO MZI as a reflective modulator for Gigabit PON (GPON) [1]. The LMM is compatible with colorless architectures, low-cost to fabricate and power-efficient [2], [3], [1]. Moreover, in this chapter we demonstrate that LMM can achieve error-free modulation rates above 10 Gb/s.

5.2 Design and fabrication of LMM in TW electrode regime

The relative phase shift between the two arms of the interferometer in the LMM is controlled by reverse bias PN junctions. The schematic of the rib waveguide structure used to implement the phase shift region is shown in Figure 1. The waveguides have a height of 220 nm and a width of 500 nm, and are surrounded by a 90 nm thick slab. The cladding is silicon dioxide. The metallurgical junction (i.e. the separation between the electrons (N) and holes (P)) is positioned at a 100 nm offset, about the center of the waveguide toward the N-side of the junction. This offset increases the mode overlap with the P-type semiconductor and improves the modulation efficiency. The reason for locating this offset in the PN junction comes from high sensitivity of the plasma dispersion effect to changes in the hole concentration rather than changes in the electron concentration [4]. A controllable phase shift is produced by the application of a reverse bias voltage across the PN junction formed at the center of the waveguides. These PN diodes are connected to series push-pull (SPP) TW electrodes regime [5] to modulate the refractive index of the MZI arms. Higher doping (P++ and N++) is used to form ohmic contacts with the electrodes, and lower doping (N and P) is used in the core of the waveguides where light is confined, and the electric field is concentrated. The values of carrier concentrations are listed in Table 1. A negative

DC bias voltage is applied to the common N-doped region between the two PN junctions with SPP-TW electrodes [5]–[7] to operate them in reverse bias.

Table 1 – Values of carrier concentrations in the PN junction

Carrier type	Concentration (cm^{-3})
P	7×10^{17}
P++	1.7×10^{20}
N	5×10^{17}
N++	5×10^{20}

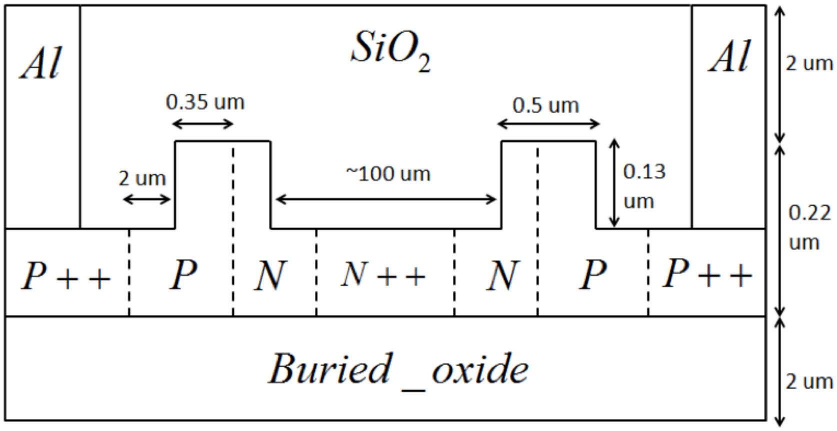

Figure 1 – Schematic and dimensions of the rib waveguide and position of the carriers

The effect of the change in carrier concentration on the effective refractive index of the silicon waveguides can be predicted based on the work by Soref *et al.* [4], [8]. Using this, together with single mode simulations of the rib waveguide, we obtain the following relationship between the electron and hole carrier concentrations and the refractive index variation:

$$\Delta n = -5.4 \times 10^{-22} \Delta N^{1.011} - 1.53 \times 10^{-18} \Delta P^{0.838} \quad (1)$$

where *ΔN* and *ΔP* are the changes in the concentration of electrons and holes, respectively, caused by the application of an electric field. The schematic of the carrier injection region and the dimensions in the actual designed LMM is shown in Figure 2. The drop output can be analyzed by positioning an off-chip circulator at the input. In the OFF state, delivering power to the modulator at the drop port does not affect the tunable laser. This is because of the presence of insulators that are placed in the laser frame in order to block the reflections that are coming back into the laser.

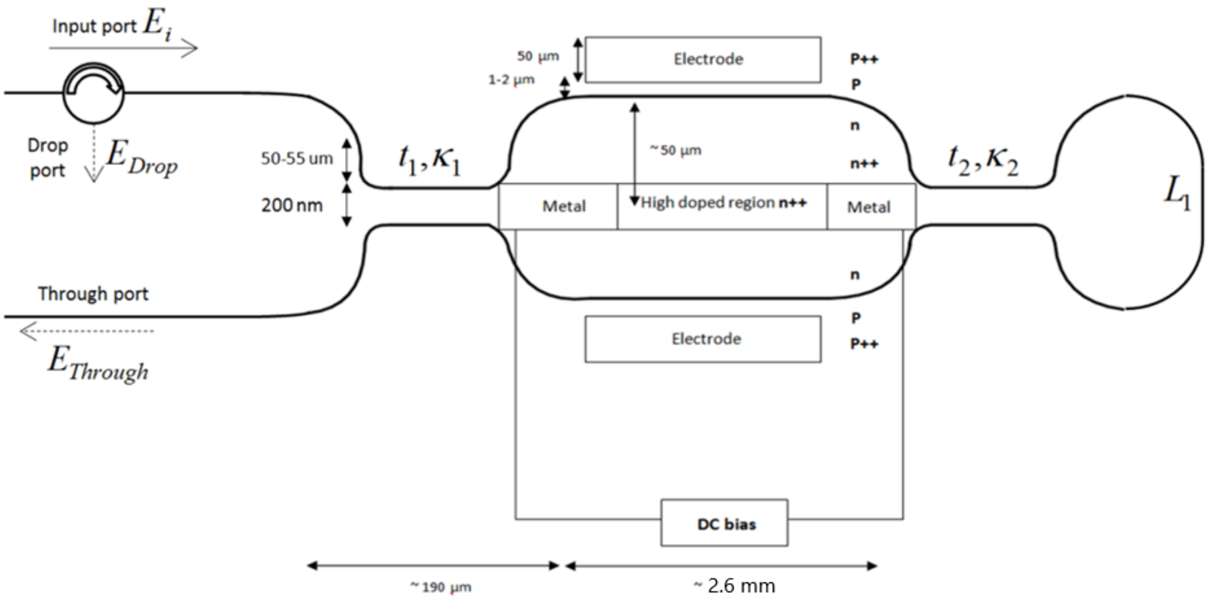

Figure 2 - Schematic of the loop-mirror MZI

Adiabatic 3dB couplers are selected to implement the LMM because their wavelength dependency is very small, and they have more robust fabrication tolerances than other types of couplers, such as multimode interference (MMI) or 3dB directional couplers [17]-[20]. The length of the adiabatic 3dB couplers is designed in Section 4.2.1 to be $L_{3dB} = 7.61\ \mu\text{m}$. The minimum separation between waveguides in the adiabatic coupler is 200 nm. The total length of the loop is 250 μm, and the radius of curvature is 10 μm. The loop is designed to connect the two outputs of the MZI. The distance between electrodes and waveguide in the active area is 1 µm.

Based on Equation (1) and the phase shift required to achieve complete intensity modulation, the length of the interferometer arms can be calculated for a target actuation voltage and operating wavelength. Taking into the account that the signal is modulated in only one direction, at $\lambda = 1.55\ \mu\text{m}$ for an actuation voltage of 4 V, the change in the effective index is $\Delta \text{n}_{\text{eff}} = 1.7\ \times 10^{-4}$. Accordingly from Section 4.3, the length of the arms of the interferometer in the LMM must be $\text{L}_{\text{LMM}} = 2.28$ mm to achieve the required phase shift [2], [3].

The loop-mirror MZI used in this research was fabricated using a commercial SOI process provided by the Institute of Microelectronics (IME) A*STAR (Singapore) and accessed through the services of CMC Microsystems. As shown in Figure 3, ground (G) and signal (S) pads for the RF probes are placed at both ends of the MZI. A DC pad is placed in the middle of the MZI to control bias conditions. The adiabatic 3dB couplers are identical on both sides. The loop is located on the right side of Figure 3, and the input and output ports are visible on the left side.

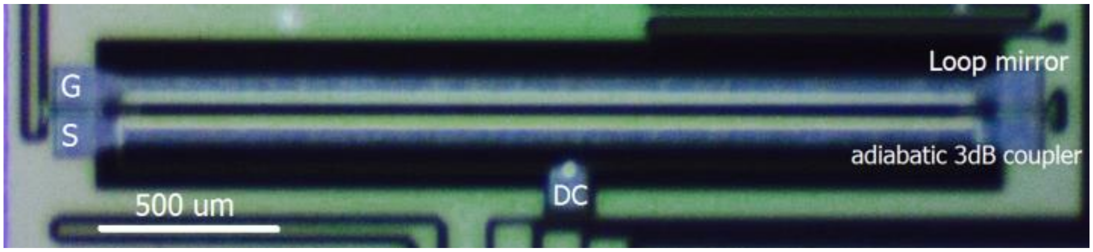

Figure 3 – Micrograph of the fabricated loop-mirror MZI

5.3 DC measurements of LMM

In order to characterize each arm of the loop-mirror MZI, a stimulus is applied to the terminals of the TW electrodes using a ground-signal (GS) probe. For each arm, the DC bias is applied separately. To perform the DC measurement, one of the diodes is shorted by applying the same potential to the P and N terminals of the diode. The experimental setup is shown in Figure 4. The light was coupled vertically to the chip using a fiber array.

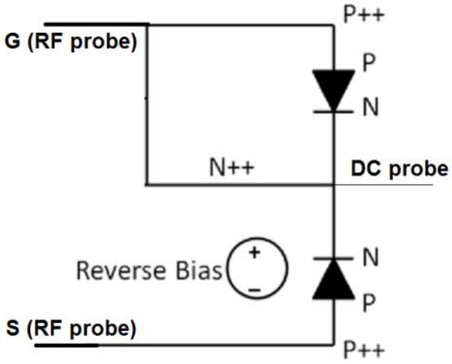

Figure 4 – Schematic of the equivalent DC bias measurement of the loop-mirror MZI

Figure 5 shows the measured transmission spectrum of the loop-mirror MZI after normalization to a reference waveguide to remove the coupling loss and the wavelength dependence of the grating couplers. As the graph indicates, the loop-mirror MZI has a broadband transmission spectrum in the C-band with less than 2 dB of variation. Due to the availability of optical equipment in our lab, a manual sweep of wavelength with a power meter was done which resulted in a coarse wavelength sweep. We estimated the insertion loss of a single grating coupler to be 6.8 dB and the total insertion loss caused by routing from the grating couplers to the modulator I/O to be 3.7 dB. After the grating coupler loss is subtracted from the transmission spectrum of the actual device, the additional propagation loss due to the presence of PN junctions in the waveguides forming the MZI arms is approximately 2.6 dB. The total insertion loss of the modulator is 10 dB, and the expected loss for each 3dB adiabatic coupler is about 1.0 dB [10].

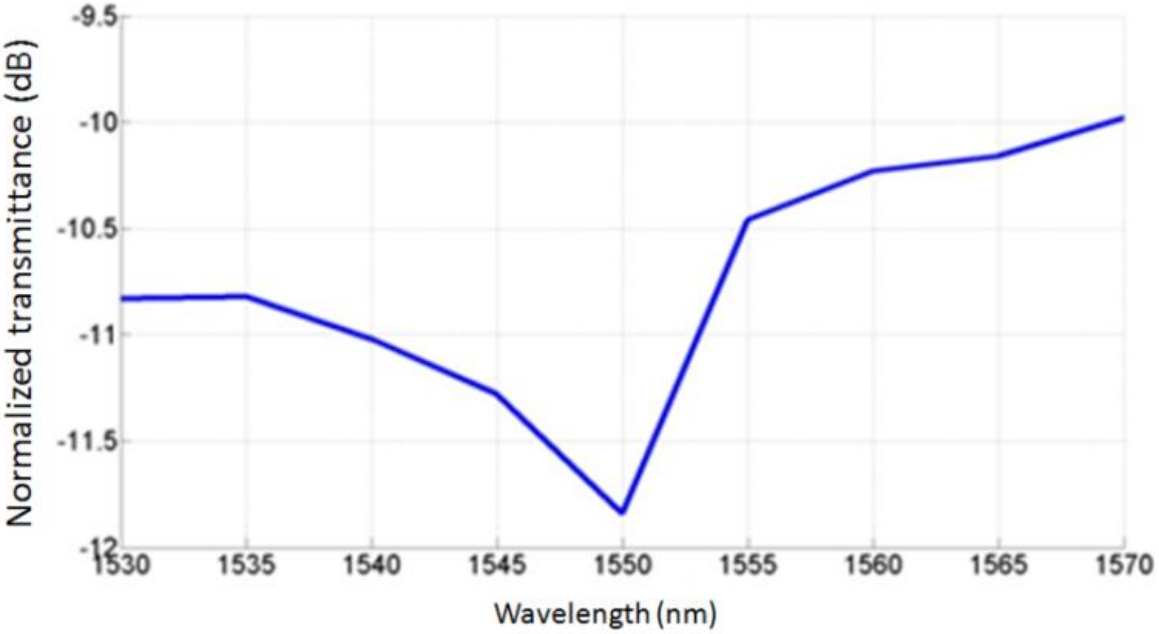

Figure 5 - Transmission spectrum of the loop-mirror MZI normalized to a reference waveguide

The transmission as a function of the applied reverse bias voltage for this device at $\lambda = 1555\ nm$ is shown in Figure 6. The minimum value in transmission occurs with 5 V applied across the PN junctions. The maximum DC modulation depth of the LMM is 25 dB.

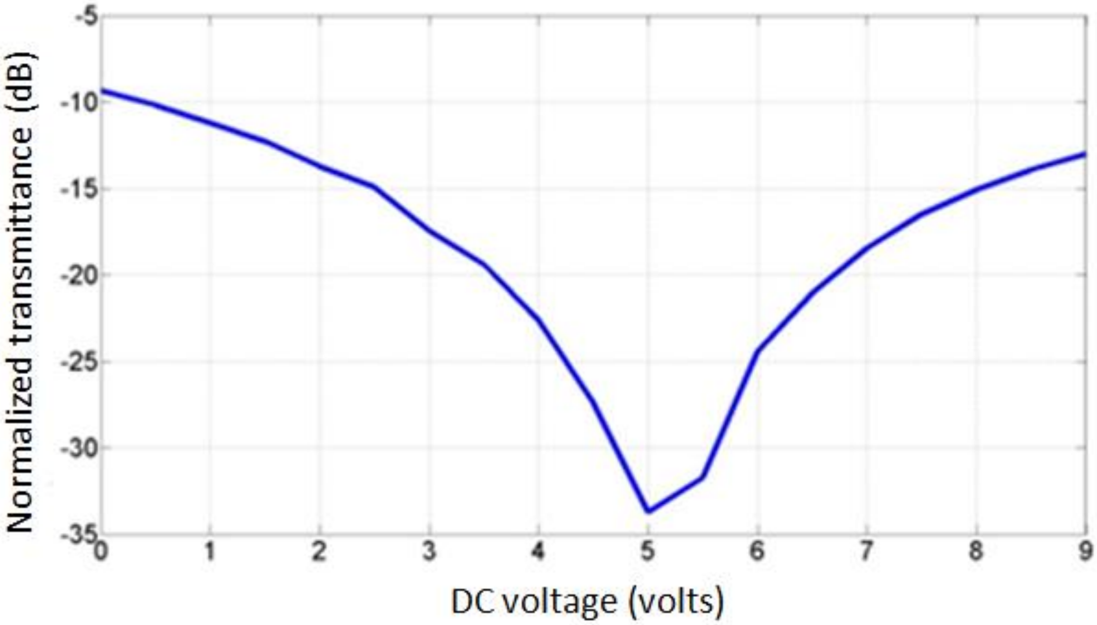

Figure 6 - Optical output power as a function of the DC bias applied across the loop-mirror MZI modulator

5.4 Experimental demonstration of LMM

We evaluated the large signal performance of the loop-mirror MZI with the experimental demonstration setup shown in Figure 7. We used a continuous wave (CW) light signal from a tunable laser. The modulated optical signal at the output of the LMM was amplified by an erbium-doped fiber amplifier (EDFA) and filtered (Agiltron with the 3dB bandwidth of 0.25 nm) to cancel noises before we entered a digital communication analyzer (DCA) to generate optical eye diagrams. A bit pattern generator (BPG) created a pseudo-random bit sequence (PRBS) signal with a peak-to-peak voltage (V_{pp}) that was used to drive the modulator. The GS probes were placed at the two ends of the electrodes of the device: one to apply the RF signal and the other to connect a 50 Ω termination to minimize reflections.

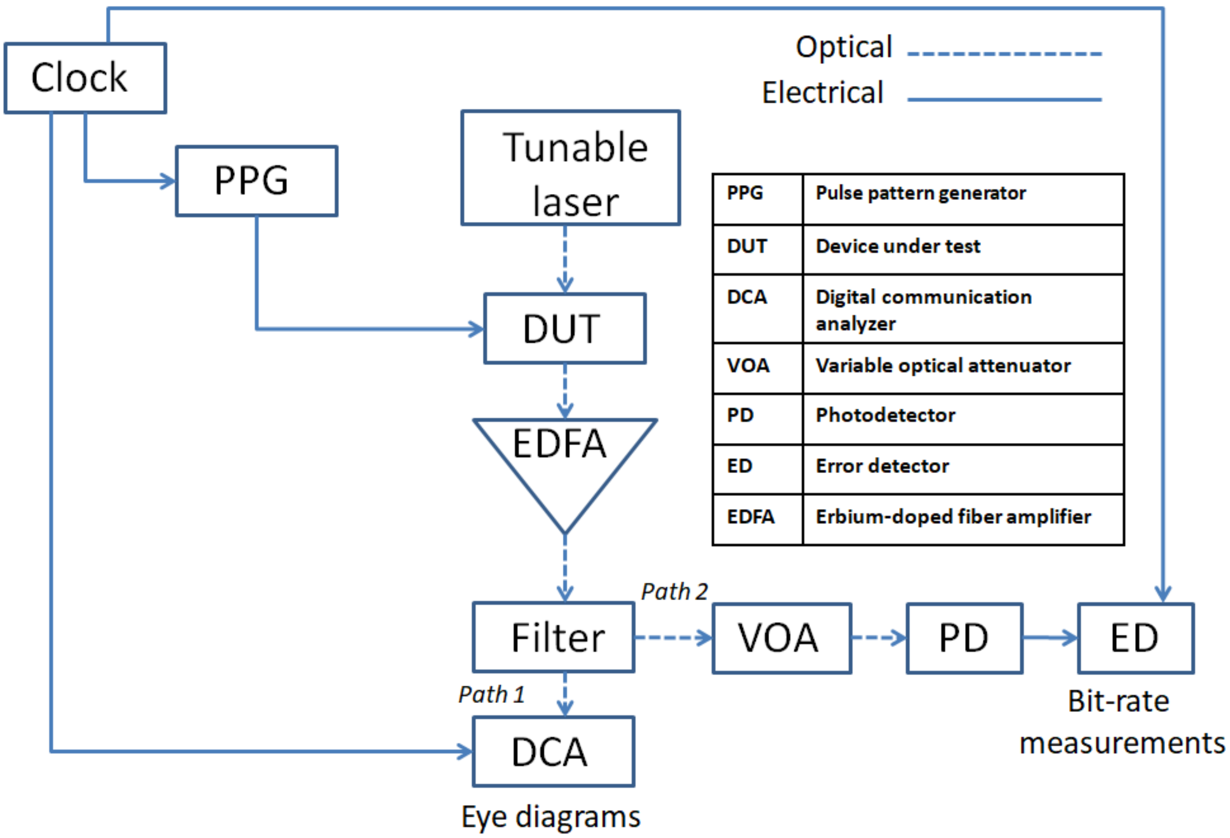

Figure 7 - Schematic of the experimental demonstration setup

To observe the performance of LMM at 10 Gb/s, a BPG was used to create a $2^7 - 1$ PRBS signal with $V_{PP} = 6.26\ \mathrm{V}$ that was applied to drive the modulator in the linear region. A DC reverse bias voltage of $2.62\ \mathrm{V}$ is applied to the modulator. This difference between the V_{PP} applied here to the LMM for big signal characterization and the quadrature voltage ($V_\pi = 5V$) measured during DC characterization (Section 5.3) comes from overdriving the LMM to reach the optimum ER. The motivation to overdrive the modulator will be explained later at this section. The clear optical eye diagram obtained at 10 Gb/s is shown in Figure 8. The measured ER is 13 dB.

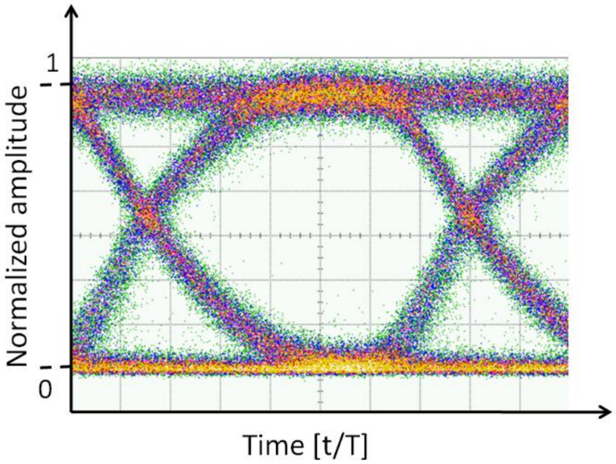

Figure 8- Optical eye diagrams at Bitrate: 10 Gb/s, ER: 13.0 dB

To quantitatively examine the modulator performance at 10 Gb/s, we performed BER tests of the system. To do this, the amplified response of the device was passed through a variable optical attenuator (VOA) coupled to a Picometrix PIN+TIA (PT-40A) receiver. Note that the receiver used here is not as sensitive as typical GPON receivers. A transmittance amplifier (TIA) is AC coupled to a photodetector (PD) to improve the sensitivity of the optical receiver. The bandwidth of the receiver is 40 GHz. The output was connected to the error detector (ED). Error-free operation ($\mathrm{BER} < 10^{-12}$) is obtained at 10 Gb/s with a received power of 0.33 dBm (Figure 9). The no-errors line indicates a measurement with zero errors detected in three terabits, thus allowing us to claim error-free operation with a 95% confidence level [8], [17], an assertion verified by the clear optical eye diagrams.

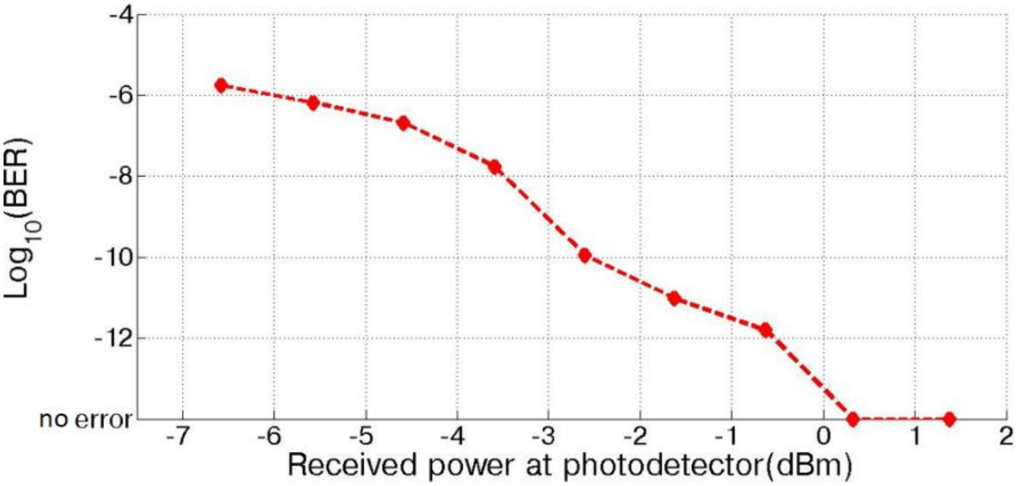

Figure 9- Sensitivity curves at 10 Gb/s

Furthermore, in a similar experiment as the case for 10 Gb/s which is also based on the setup in Figure 7, but for higher modulation rates, we used a CW light signal from a tunable laser with a wavelength of 1565 nm and a power of 14 dBm. We used NRZ modulation to perform the measurements. A BPG created a $2^{31}-1$ PRBS signal with $V_{PP}=2.6$ V that was used to drive the modulator. Because of equipment limitations, we could only apply a DC reverse bias voltage of 2.0 V to the modulator. Since the modulator is not biased at the exact quadrature point, we could not use the optimum modulation amplitude, limiting the extinction ratio [11].

Optical eye diagrams at different bitrates are shown in Figures 10-14. Clear optical eyes are observed up to 20 Gb/s. Additional electrical and optical design optimizations should make it possible to increase the modulation speed. Due to the effect of the counter-propagation signal coming back from the loop-mirror section of the device, the openings in the optical eye diagrams are asymmetric (oval-shaped) and the eye-opening spaces become smaller for the higher modulation rates.

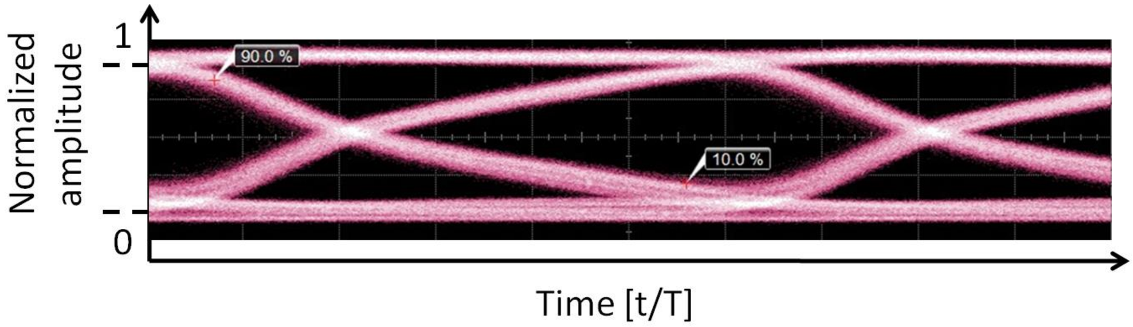

Figure 10 - Bitrate: 15 Gb/s, ER: 4.093 dB

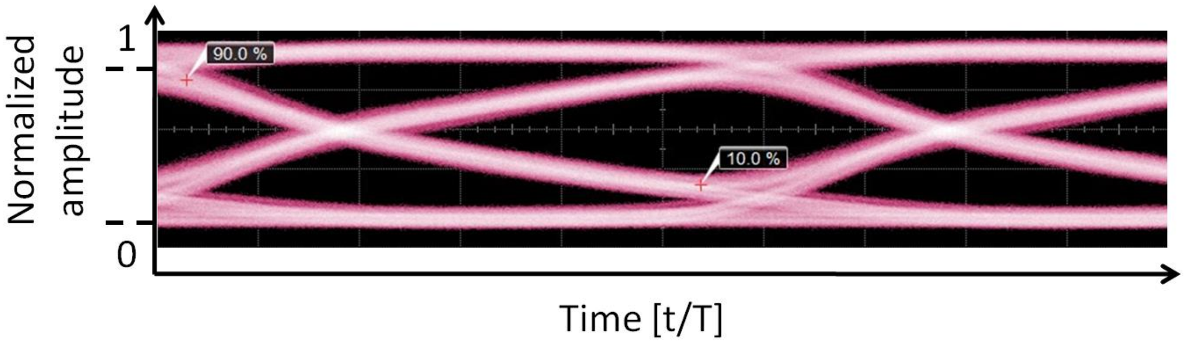

Figure 11 - Bitrate: 18 Gb/s, ER: 3.607 dB

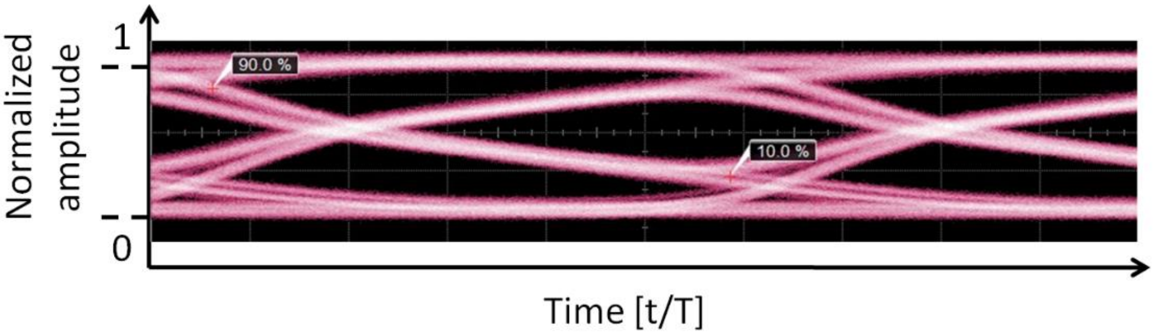

Figure 12 - Bitrate: 20 Gb/s, ER: 2.958 dB

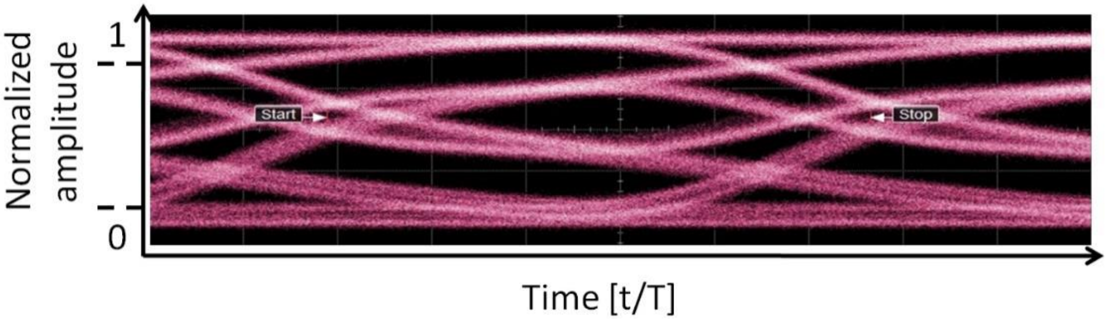

Figure 13 - Bitrate: 25 Gb/s, ER: 2.449 dB

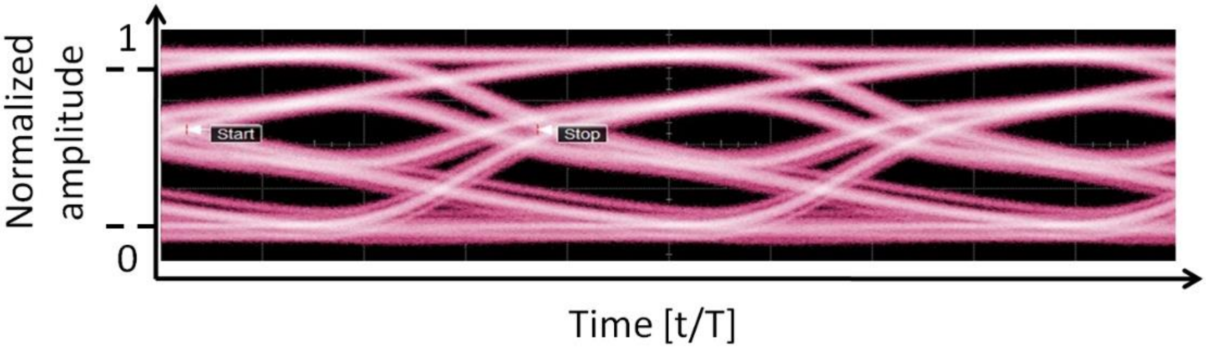

Figure 14 – Bitrate: 26 Gb/s, ER: 2.515 dB

To quantitatively examine the modulator performance, the BER test has been performed as shown in Figure 7. Error-free $BER < 10^{-12}$ operation is obtained up to 18 Gb/s with a received power of 4 dBm (blue line - Figure 15). The no-errors linear trend line indicates a measurement with zero errors detected in three terabits, allowing us to claim error-free operation with clear optical eye diagrams. In addition, operation with a $BER < 10^{-6}$ is achieved up to 21 Gb/s with the same received power, well below the requirement for links implemented with forward error correction (red line - Figure 15).

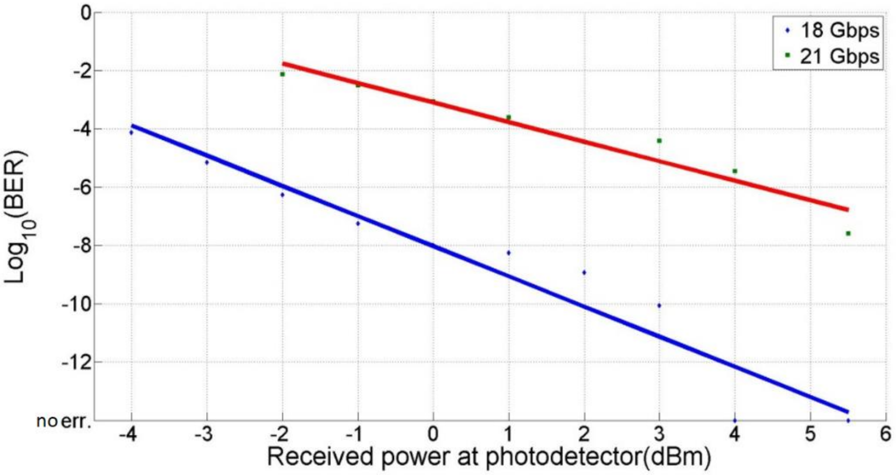

Figure 15 - Sensitivity curves at 18 Gb/s and 21 Gb/s modulation speed

In the large signal characterization of a loop-mirror MZI, we can report that in a TW electrode regime, this device is capable of a 20 Gb/s modulation rate. Furthermore, the theoretical prediction of Chapter 4 is that the LMM has reduced power requirements compared to a conventional MZI in the lumped electrode regime. Finally, the integrated loop-mirror device has the potential to be used as a reflective mirror in integrated laser cavities.

As explained in the large signal measurement for 10 Gb/s, the V_{PP} which was applied in order to achieve optimum big signal performance is slightly higher than V_π used for DC characterization. To obtain a physical explanation of LMM biasing, we used the analytical model extracted in Section 4.4. We can show that overdriving the LMM reduces the frequency roll-off shown in Fig. 16. As we observed experimentally and listed in Table 2, the effect of change in the various values of V_{PP} on the ER is significant and proves the importance of appropriate biasing of the modulator to achieve optimum performance as well mentioned in [18] for different types of silicon-based modulators.

Table 2 – Experimental values for LMM performance at 10 Gb/s

V_{PP} (V)	V_π (V)	ER (dB)
4.09	$0.818V_\pi$	5.45
5.93	$1.186V_\pi$	10.36
6.26	$1.25V_\pi$	13.00

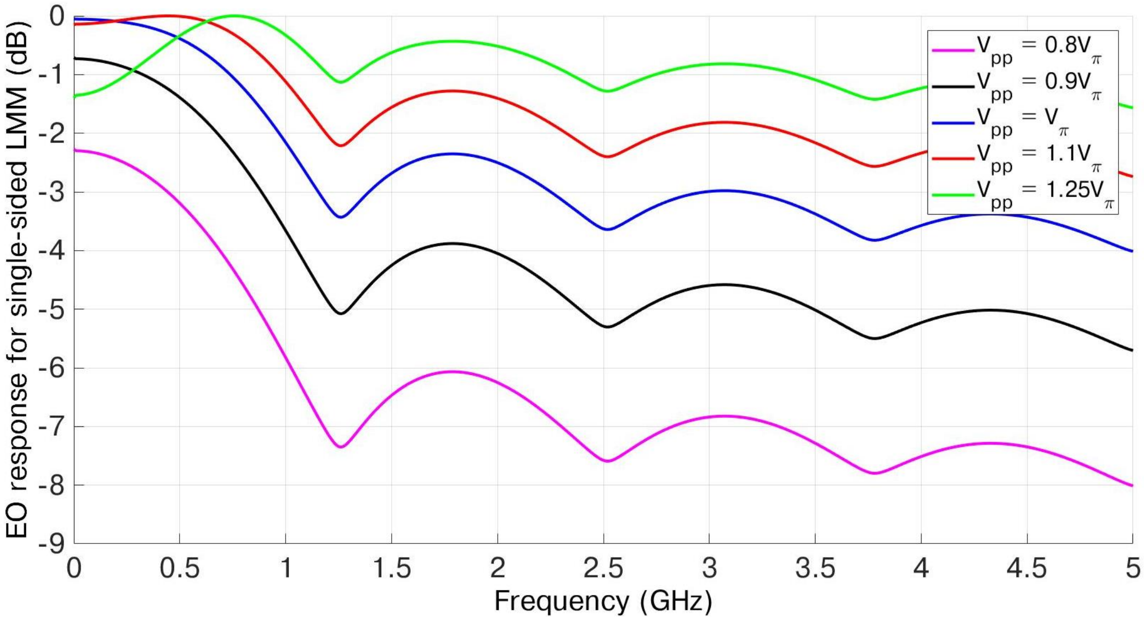

Figure 16- EO response of LMM for different tolerances of V_{PP}

In this section, we showed that an integrated EO modulator that combines an MZI with a loop-mirror has the potential to be used as a reflective modulator in a passive optical networks (PON) and a Gigabit PON (GPON). The 10 Gb/s modulation rate is similar to the recent modulation rate used in PONs. As stated in Section 2.7, the LMM can be a potential candidate for upstream transmission in PON. The LMM has the possibility to act as a low-cost modulator for GPON applications and has a suitable transmission bandwidth. As explained in Section 4.4, in the TW regime, the frequency response of LMM approaches that of an equivalent MZI operated at the same drive voltage. The counter-propagation modulation in our demonstrator is efficient at low frequencies. However, the 1 GHz frequency limit for efficient operation could be raised significantly if shorter electrodes were available in our current designed chip. Thus, in that regime the LMM can generate a phase difference between its arms twice as large as an equivalent MZI for the same modulation voltage which results in significantly lower power consumption in comparison to an MZI with an equivalent configuration [2]. The experimental results for 3dB bandwidth of LMM are also included in Section 4.4.

5.5 Lumped loop-mirror modulator estimations

In general, when the length of an optical device is approximately bigger than one-tenth of the guiding wavelength λ_g, one needs to use the distributed element analysis (i.e. traveling wave regime) rather than the lumped regime element analysis. In other words, the length of the phase-shifter region should be comparable with the wavelength of the electrical wave [12], [13]. For the LMM the length of the phase shift region in MZI is 2.28 mm and the length of the TW electrode (total length of LMM device) is 4.0 mm. For the guiding wavelength we have

$$\lambda_g = \frac{c_0}{f\sqrt{\varepsilon_{re}}} \tag{2}$$

where ε_{re} is the effective relative permittivity of the guiding medium, f is the frequency, and c_0 is the speed of light. If $L_{critical}$ is the critical length that determines when traveling-wave analysis should be performed, then

$$L_{critical} = \frac{\lambda_g}{10} \tag{3}$$

As a rough estimation from Figure 1 that ignores the dispersion and the dependency to the cross-section of the transmission line, we have

$$\varepsilon_{re} = \frac{C_{superstrate}+C_{substrate}}{2C_{superstrate}} = \frac{\varepsilon_{air}+\varepsilon_{silicon}}{2} = \frac{1+11.7}{2} = 6.35 \tag{4}$$

Consequently, if $f \cong 20\ GHz$ then $L_{critical} \cong 0.6\ mm.$

5.6 Comparison of the design and performance of the LMM with the similar state-of-the-art MZI devices

The head-to-head comparison of the LMM with the state-of-the-art devices in terms of design and performance are presented in Tables 3 and 4. This comparison shows where the LMM stands among the existing MZI-based modulators.

Table 3 – Comparison of the LMM with the existing state-of-the-art MZI-based modulators which have carrier depletion in the lateral PN diodes

	Phase-shifter length (mm)	Waveguide width x height (um x um)	Slab height (nm)	BOX eight (um)	Transmission rate (Gb/s)	V_{π}(V) reverse bias	Vpp (V) + Vdc-bias (V)	λ (nm)	Extinction ratio (dB)	Reference
1	2.28	0.5 x 0.22	130	2	18 -20	5	2.6 + (-2)	1565	3.6 - 3	LMM
2	1	0.5 x 0.25	200	3	12 – 12.5	6	6 + (-3)	1550	> 6 ~ 7	[22]
3	1 mm - 750 um	0.5 x 0.22	120	1	12.5		4 + (-4)	1531	3	[23]
4	2	0.5 x 0.22	120	1	4		4 + (-4)	1535.5	7	[23]
5	1mm - 750 um	0.5 x 0.22	120	1	12.5		1.2 + (-3)	1542	10.5	[24]
6	1mm - 750 um	0.5 x 0.22	120	1	20				9.1	[24]
7	6	0.5 x 0.22	130	3	20	3.1	3.5 + (-3)	1550	10	[25]
8	2	0.5 x 0.22	130	3	40~50	12	(4.5~5.5) + (-4~6)		4.7	[25]
9	4	0.6 x 0.22	110 - 160	2	10		5 + (-3.75)		6.1	[26]
10	750 um	0.45 x 0.34	260	2	45-60	~ 8	6.5 + (-5)	1558.79	7.5	[27]

Table 4 – Comparison of the various carriers in the PN junctions listed in Table 3

#	P (cm^{-3})	P+ (cm^{-3})	N (cm^{-3})	N+ (cm^{-3})	Reference
1	7×10^{17}	1.7×10^{20}	5×10^{17}	5×10^{20}	LMM
2	5×10^{17}	1×10^{20}	1×10^{18}	1×10^{20}	[22]
3	1×10^{18}	1×10^{20}	1×10^{19}	1×10^{20}	[23]
4	5×10^{18}	1×10^{20}	1×10^{19}	1×10^{20}	[23]
5	1×10^{18}	1×10^{20}	1×10^{19}	1×10^{20}	[24]
6	1×10^{18}	1×10^{20}	1×10^{19}	1×10^{20}	[24]
7	5×10^{17}	1×10^{20}	5×10^{17}	1×10^{20}	[25]
8	5×10^{17}	1×10^{20}	5×10^{17}	1×10^{20}	[25]
9	5×10^{17}	1×10^{20}	5×10^{17}	1×10^{20}	[26]
10	2×10^{17}	1×10^{20}	4×10^{17}	1×10^{20}	[27]

5.7 Power consumption of LMM

The analysis of the LMM design requires that the effect of both the co- and counter-propagation of the optical signal with respect to the RF modulating voltage be considered. Chapter 4 shows that at high frequencies, the LMM has a frequency response comparable to that of an equivalent MZI for the same drive voltage. However, based on our analysis in Section 4.3 and also in [2], [12], and [13], we argue that for a reversed bias LMM with lumped electrodes using NRZ signaling, the required energy/bit is one-quarter of the switching energy needed by an MZI [14]. Based on the work reported by Miller [15] and Plant [6], [16], the power consumption under NRZ signaling of an MZI can be related to the square of the driving voltage as

$$P = C_t V_{pp}^2 / 4 \tag{5}$$

$$\Delta E = P \times (bitperiod) \tag{6}$$

where ΔE is the energy stored per cycle and C_t is the capacitance of the PN junctions used to generate the phase shift, which is a function of the reverse applied voltage. The capacitance of the PN junctions can be estimated based on their dimensions and the density of carriers across the waveguide cross-section. Since an LMM with lumped electrodes regime requires one-half the modulation voltage required by an equivalent MZI to provide the same modulation depth, the estimated power consumption of the former is one-quarter that of the latter because, as shown in Equation (5), the power consumption is a function of the square of the modulating voltage. This is expressed as:

$$P_{LMM} = C_t (V_{pp}/2)^2 / 4 \tag{7}$$

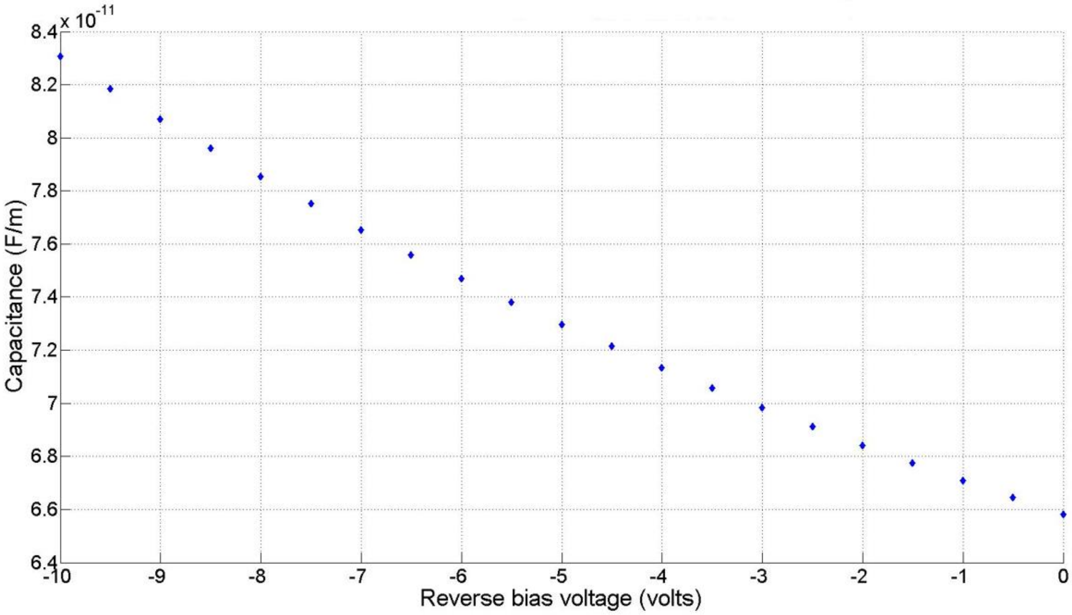

Figure 17- Simulated capacitance of PN junction by the applied reverse bias voltage

As mentioned in Section 5.4, the driving voltage to modulate at 20 Gb/s is $\mathrm{V_{PP}} = 2.6\ \mathrm{V}$. The dynamic power consumption of the LMM device at a modulation rate of 20 Gb/s is estimated to be 65.01 pJ/bit.

5.8 Conclusion

In this chapter, we present integrated silicon-based LMM. As described in Section 2.7, the silicon-based LMM is a cost-efficient solution in comparison to other remote modulation devices such as IL-FP, RSOA, and EAM. As explained in Section 4.4, the added loop does not affect the bandwidth or the frequency response of LMM. Most of the losses of the LMM are due to coupling and routing, which can easily be improved [19]. Some other modifications that can be done to reduce the insertion loss are developments in the end-face polishing techniques [20], and improvements in the alignment of connectors [21]. For future works, the revised LMM design contains shorter electrodes with a smaller phase shift. The lumped model regime is expected to provide higher modulation speed with lower power consumption than previously mentioned methods.

References

[1] F. Soltani, M. Menard, and A. G. Kirk, “Integrated silicon photonic reflective modulator for passive optical networks,” in *IEEE/OSA CLEO conference*, 2017.

[2] F. Soltani, M. Menard, and A. G. Kirk, “Optical modulator with an integrated loop-mirror,” in *IEEE Optical interconnects conference (OI)*, 2015.

[3] F. Soltani, M. Menard, and A. G. Kirk, “Low-power 20Gb / s modulator with an integrated loop-mirror,” in *Asia Communications and Photonics Conference (ACP) IEEE/OSA/SPIE sponsored*, 2015.

[4] R. A. Soref and B. R. Bennett, “Electrooptical effects in silicon,” *IEEE J. Quantum Electron.*, vol. 23, no. 1, pp. 123–129, 1987.

[5] P. Dong, L. Chen, and Y. Chen, “High-speed low-voltage single-drive push-pull silicon Mach-Zehnder modulators,” *Opt. Express*, vol. 20, no. 6, pp. 6163–6169, 2012.

[6] D. Patel, V. Veerasubramanian, S. Ghosh, A. Samani, Q. Zhong, and D. V Plant, “High-speed compact silicon photonic Michelson interferometric modulator.,” *Opt. Express*, vol. 22, no. 22, pp. 26788–802, 2014.

[7] R. Ding *et al.*, “Design and characterization of a 30-GHz bandwidth low-power silicon traveling-wave modulator,” *Opt. Commun.*, vol. 321, pp. 124–133, 2014.

[8] M. Nedeljkovic, R. Soref, and G. Z. Mashanovich, “Free-carrier electro-refraction and electro-absorption modulation predictions for silicon over the 1-14-um infrared wavelength range,” *IEEE Photonics J.*, vol. 3, no. 6, pp. 1171–1180, 2011.

[9] K. Solehmainen, M. Kapulainen, M. Harjanne, and T. Aalto, “Adiabatic and multimode interference couplers on silicon-on-insulator,” *IEEE Photonics Technol. Lett.*, vol. 18, no. 21, pp. 2287–2289, 2006.

[10] H. Yun *et al.*, “2x2 broadband adiabatic 3-dB couplers on SOI strip waveguides for TE and TM modes,” *Proc. SPIE, Photonics North*, vol. 29, p. 89150v, 2013.

[11] Y. Fu, X. Zhang, B. Hraimel, T. Liu, and D. Shen, “Mach-Zehnder: A review of bias control techniques for mach-zehnder modulators in photonic analog links,” *IEEE Microw. Mag.*, vol. 14, no. 7, pp. 102–107, 2013.

[12] A. Samani, “Design and Characterization of 35 GHz Silicon Photonic Travelling Wave Modulator for Next Generation Short Reach Communication Links,” McGill University, 2014.

[13] D. Patel, “Design, analysis, and performance of a silicon photonic traveling wave Mach-Zehnder modulator,” McGill University, 2014.

[14] M. R. Watts, W. A. Zortman, D. C. Trotter, R. W. Young, and A. L. Lentine, “Vertical junction silicon microdisk modulators and switches,” *Opt. Express*, vol. 19, no. 22, pp. 21989–2003, 2011.

[15] D. A. B. Miller, “Energy consumption in optical modulators for interconnects,” *Opt. Express*, vol. 20, no. S2, pp. A293–A308, 2012.

[16] A. Samani *et al.*, “A low-voltage 35-GHz silicon photonic modulator-enabled 112-Gb/s transmission system,” *IEEE Photonics J.*, vol. 7, no. 3, 2015.

[17] F. Payoux, P. Chanclou, and N. Genay, “WDM-PON with colorless ONUs,” *OFC/NFOEC 2007 - Opt. Fiber Commun. Natl. Fiber Opt. Eng. Conf. 2007*, pp. 2–4, 2007.

[18] G. T. Reed, G. Mashanovich, F. Y. Gardes, and D. J. Thomson, “Silicon optical modulators,” *Nat. Photonics*, vol. 4, no. 8, pp. 518–526, 2010.

[19] A. Michaels and E. Yablonovtich, “Inverse Design of Near Unity Efficiency Perfectly Vertical Grating Couplers,” vol. 25, no. 15, pp. 119–122, 2017.

[20] S. I.-E. Lin, “Effect of polishing conditions on terminating optical connectors with spherical convex polished ends.,” *Appl. Opt.*, vol. 41, no. 1, pp. 88–95, 2002.

[21] M. Margolin and I. Grois, “Fiber optic connector,” US4705352 A, 10-Nov-1987.

[22] N. Feng, S. Liao, D. Feng, P. Dong, D. Zheng, and H. Liang, “High speed carrier depletion modulators with 1 . 4V-cm V π L integrated on 0 . 25 μ m silicon-on- insulator waveguides,” *Opt. Express*, vol.

18, no. 8, pp. 7994–7999, 2010.

[23] J. W. Park, J.-B. You, I. G. Kim, and G. Kim, “High-modulation efficiency silicon Mach-Zehnder optical modulator based on carrier depletion in a PN Diode.,” *Opt. Express*, vol. 17, no. 18, pp. 15520–4, 2009.

[24] G. Kim, J. W. Park, I. G. Kim, S. Kim, S. Kim, J. M. Lee, G. S. Park, J. Joo, K.-S. Jang, J. H. Oh, S. A. Kim, J. H. Kim, J. Y. Lee, J. M. Park, D.-W. Kim, D.-K. Jeong, M.-S. Hwang, J.-K. Kim, K.-S. Park, H.-K. Chi, H.-C. Kim, D.-W. Kim, and M. H. Cho, “Low-voltage high-performance silicon photonic devices and photonic integrated circuits operating up to 30 Gb/s.,” *Opt. Express*, vol. 19, no. 27, pp. 26936–47, 2011.

[25] P. Dong, L. Chen, and Y. Chen, “High-speed low-voltage single-drive push-pull silicon Mach-Zehnder modulators,” *Opt. Express*, vol. 20, no. 6, pp. 6163–6169, 2012.

[26] T. Y. Liow, K. W. Ang, Q. Fang, J. F. Song, Y. Z. Xiong, M. Bin Yu, G. Q. Lo, and D. L. Kwong, “Silicon modulators and germanium photodetectors on SOI: Monolithic integration, compatibility, and performance optimization,” *IEEE J. Sel. Top. Quantum Electron.*, vol. 16, no. 1, pp. 307–315, 2010.

[27] X. Xiao, H. Xu, X. Li, Z. Li, T. Chu, Y. Yu, and J. Yu, “High-speed, low-loss silicon Mach-Zehnder modulators with doping optimization.,” *Opt. Express*, vol. 21, no. 4, pp. 4116–25, 2013.

Chapter 6

Design and Measurement Results of Loop-Mirror Modulator in Differential Phase Shift Keying Modulation

6.1 Introduction

Advanced modulation schemes use phase modulation to improve spectral efficiency in long-haul optical transmissions. One such format is differential phase shift keying (DPSK). As it is described in Chapter 2, Section 2.6, in DPSK information is encoded by changing the phase of the optical signal when there is a transition between bit symbols in the data stream. DPSK has several advantages. In comparison to OOK, DPSK provides a sensitivity improvement of approximately 3 dB [1]. Furthermore, DPSK generates optical signals that are less sensitive to chromatic dispersion in optical fibers [2]. DPSK has also been demonstrated in dense short-reach interconnects using WDM channels to enhance power budget margins [4]. High order modulation formats, such as DPSK and quadrature phase shift keying (QPSK), are often generated with modulators comprising many MZMs in a nested configuration. A very recent demonstration of DPSK modulation on an SOI platform using ring resonators was reported in [5]. DPSK modulation can also be performed with SOI OOK based MZMs [4], [6] by changing the electrical bias voltage of the device.

Here, we demonstrate DPSK modulation using an LMM. This modulator is capable of performing arbitrary intensity and phase modulation. The details of the LMM design and performance in OOK have been presented in Chapter 4 and 5 as well as in [7] and [8]. In Section 6.2, we showed analytically that this device is capable of phase-only modulation by considering a critical condition for the applied voltage to the electrodes. Based on a theoretical analysis in [9], we show that in the lumped electrode regime LMM requires only one-half the applied drive voltage and, consequently, has a one-quarter the power consumption of MZM devices with an equivalent configuration and a similar drive voltage [10]. We also present experimental data showing that the LMM is functional in the TW regime. As explained in Chapter 4, in the TW model at high frequencies, the response of the device approaches that of an equivalent MZM operating at a similar drive voltage [7]–[9], [11]. In this chapter DPSK modulation at 10 Gb/s with a dual-drive loop-mirror MZM is presented. The LMM has the potential to operate at higher speeds but we were limited in our demonstration by our BER detector.

6.2 Theory

The LMM, which was introduced in Chapter 4 and also in [9] and [11], is an optical modulator made by addition of a loop-mirror to one end of an MZI, as shown in Figure 1. In LMM, the arms of the MZI have a slight length difference (22 μm); thus, the device is asymmetric. The optical transfer function of the LMM is obtained as follows.

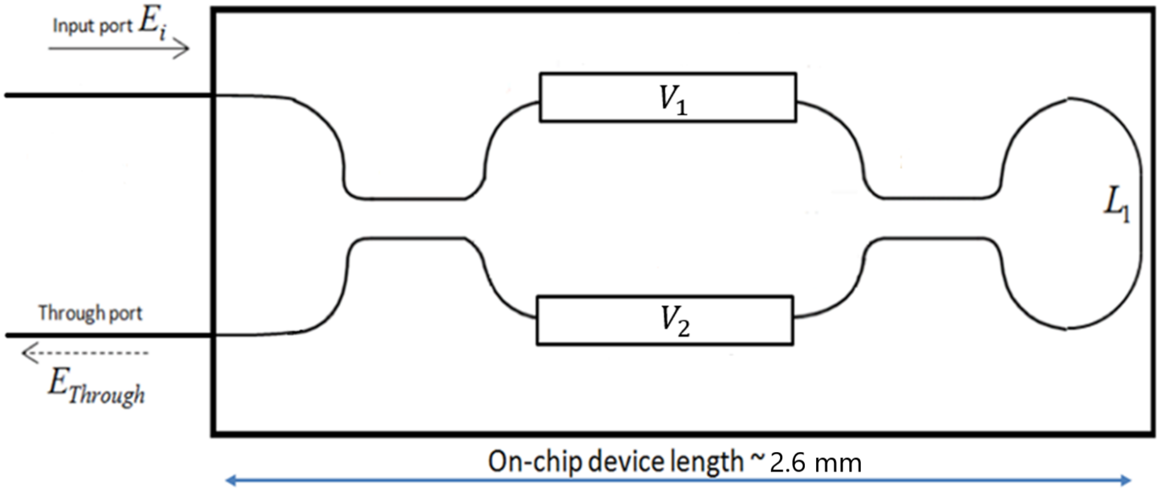

Figure 1- Schematic of LMM

Assuming lossless propagation in the couplers, if the coupler matrix is expressed as parameter C in Equation (1), the loop matrix is expressed as parameter L in Equation (2), the matrix for the upper arm of the single-drive MZI in LMM is M_f in Equation (3), the matrix for the bottom arm of the single-drive MZI in LMM is M_b in Equation (4), and the input vector is E_{in} in Equation (5), then the expression for the output of the single-drive LMM is given by the vector E_{thru} in Equation (7):

$$C = \begin{bmatrix} \frac{\sqrt{2}}{2} e^{-j\phi} & -j\frac{\sqrt{2}}{2} e^{-j\phi} \\ -j\frac{\sqrt{2}}{2} e^{-j\phi} & \frac{\sqrt{2}}{2} e^{-j\phi} \end{bmatrix} \tag{1}$$

$$L = \begin{bmatrix} e^{-j\beta \mathrm{L}_1} & 0 \\ 0 & e^{-j\beta \mathrm{L}_1} \end{bmatrix} \tag{2}$$

$$M_f = \begin{bmatrix} e^{-j(\theta_0 + N_1 V_1)} & 0 \\ 0 & e^{-j\theta_0} \end{bmatrix} \tag{3}$$

$$M_b = \begin{bmatrix} e^{-j(\theta_0 + N_1 V_2)} & 0 \\ 0 & e^{-j\theta_0} \end{bmatrix} \tag{4}$$

$$\overrightarrow{E_{in}} = \begin{bmatrix} E_{in} \\ 0 \end{bmatrix} \tag{5}$$

$$\overrightarrow{E_{out}} = \begin{bmatrix} E_R \\ E_T \end{bmatrix} \tag{6}$$

$$E_{thru} = C.M_f.C.L.C.M_b.C.E_{in} \tag{7}$$

where $\boldsymbol{\beta}$ is the propagation constant of the waveguides, angle $\boldsymbol{\varphi}$ is the fixed phase difference in the 3dB couplers, $\mathbf{L_1}$ is the length of the loop, angle $\boldsymbol{\theta_0}$ is the initial phase difference between the MZI arms, and the constant $\boldsymbol{N_1}$equals to is given by $\boldsymbol{N_1} = \frac{-\boldsymbol{\pi}}{\boldsymbol{V_{p1}}}$ in which $\boldsymbol{V_{p1}} \cong \mathbf{5}\ \boldsymbol{V}$ is the voltage required for a π phase shift of the single-drive MZI and is obtained experimentally for this device during characterization. $\boldsymbol{V_{DC}}$ is the DC bias voltage applied across the PN junction to change the effective index of the MZI; $\boldsymbol{V_1}$ is the drive voltage applied to the top arm of the MZI; $\boldsymbol{V_2}$ is the drive voltage applied to the bottom arm of the MZI. The relationships between these angles and the geometry of the modulator are expressed in Equations (8) and (9):

$$\theta_0 = \frac{2\pi}{\lambda} n_{eff} L_{MZI} \tag{8}$$

$$\varphi = \frac{2\pi}{\lambda} n_{eff} L_{3dB} \tag{9}$$

where L_{MZI} is the length of the phase-shifter part of the MZI, L_{3dB} is the length of the 3dB couplers, and n_{eff} is the effective index of the device obtained with the Lumerical MODE Solutions software. Based on Equations (1) - (9), E_{thru} can be expressed by:

$$E_{R-LMM}(V_1, V_2) = \frac{j}{2} e^{\frac{-j\left(\pi V_2 + V_{p1}(\mathrm{L}_1 \beta + 4\phi)\right)}{V_{p1}}} \left(-1 + e^{\frac{j\pi(V_1 + V_2)}{V_{p1}}}\right) \tag{10}$$

By examining Equation (10), it is possible to show that the LMM is capable of phase-only modulation. First, to simplify Equation (10) we can assume that $\mathrm{L}_1 = 1, \beta = 2\pi, \phi = 0$, and using trigonometric identities then

$$E_{R-LMM}(V_1, V_2) = \frac{1}{2}\; e^{j\pi \frac{V_1}{V_{p1}} + j\frac{\pi}{2}} - \frac{1}{2} e^{-j\pi \frac{V_2}{V_{p1}} + j\frac{\pi}{2}} \tag{11}$$

The intensity of LMM is derived in Equation (12) and plotted in Figure 2. Consequently, the phase of LMM is derived in Equation (13) and plotted in Figure 3.

$$|E_{R-LMM}|^2 = \frac{1}{2}\;[1 + \cos(\frac{\pi}{V_\pi}(V_1 + V_2 + V_\pi)] \tag{12}$$

$$\angle E_{R-LMM} = -\frac{\pi}{2V_\pi}(2V_2 + V_\pi) \tag{13}$$

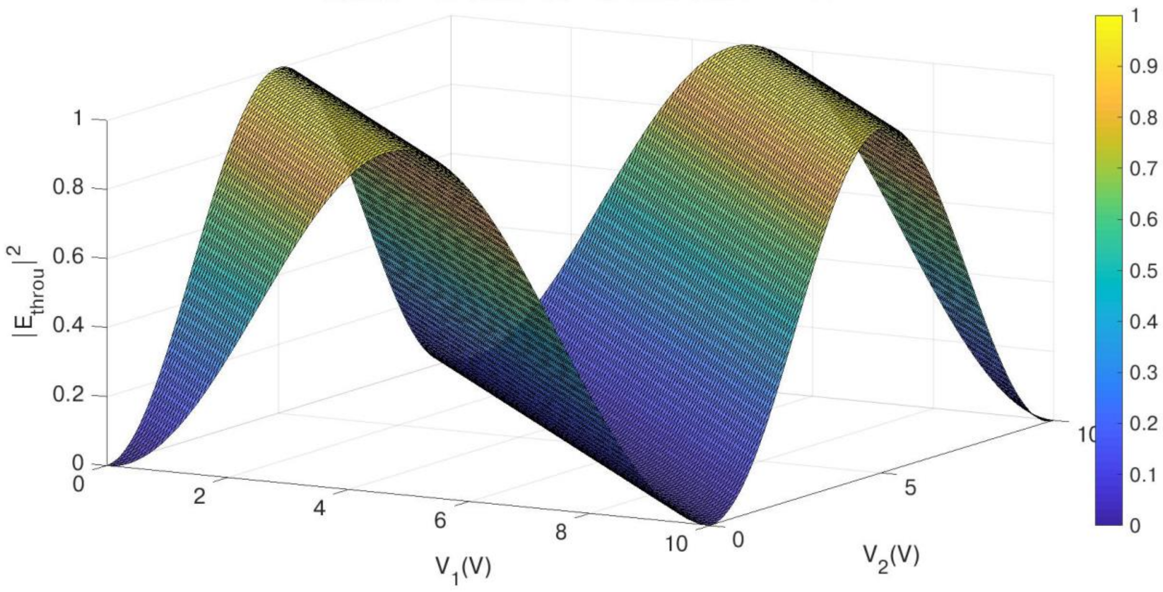

Figure 2- Intensity of LMM as a function of applied voltages when $V_\pi = 5V$

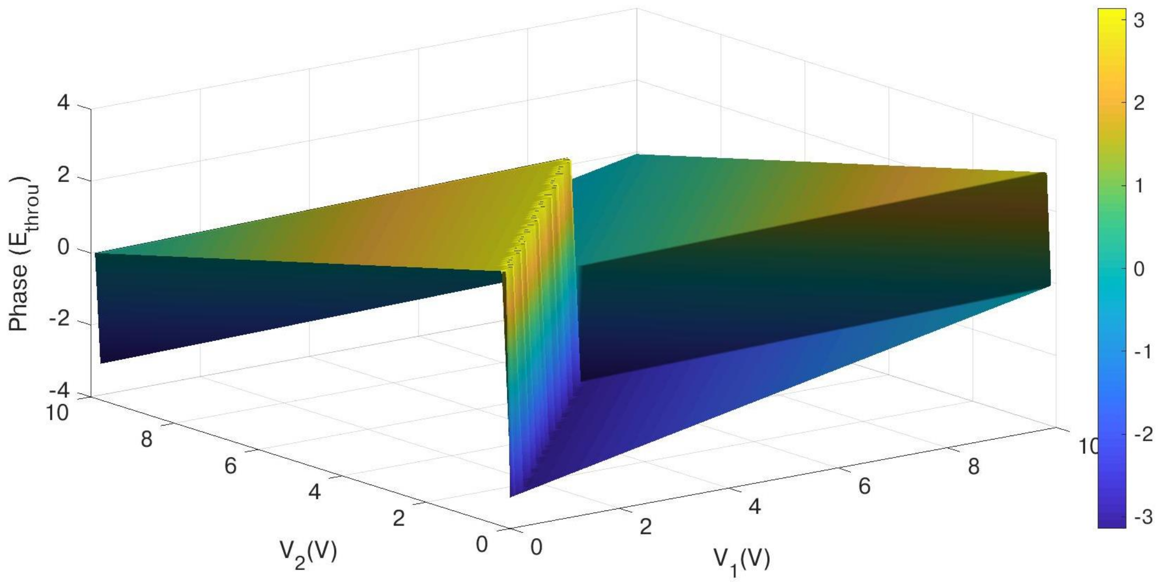

Figure 3- Phase of LMM as a function of applied voltages when $V_\pi = 5V$

Phase-only modulation with the LMM is possible when the output intensity maintains a constant unit amplitude value. By requiring that $|E_{thru}|^2 = 1$, we obtain a condition for V$_2$ as a function of V$_1$:

$$V_2 = V_{p1} - V_1 \tag{14}$$

This expression for V_2 is symmetric with V_1, since $V_2 - V_1 = \pm V_{p1}$. By changing the expression $V_2 = V_{p1} - V_1$ to the more general expression $V_2 = V_c - V_1$ where $V_c \leq V_{p1}$, the LMM output intensity will range from zero (for $V_c = 0$) to one (for $V_c = V_{p1}$). This proves that the LMM can provide both an arbitrary phase and amplitude modulation. Through Equation (11), the voltages V_1 and V_2 can be written as functions of the amplitude and phase output of the LMM. The resulting equations are, respectively:

$$V_1 = \frac{V_\pi}{\pi}(cos^{-1}(2\,|E_{R-LMM}|^2 - 1) + \angle E_{R-LMM} - \frac{\pi}{2}) \tag{15}$$

$$V_2 = \frac{V_\pi}{\pi}(-\angle E_{R-LMM} - \frac{\pi}{2}) \tag{16}$$

The physical explanation of the principles of DPSK modulation format relies on the fact that the amplitude is constant and thus $|E_{R-LMM}| = 1$, while the phase varies as $\angle E_{R-LMM} = 0, \pi$. Different voltage values required for phase modulation according to Equations (15) and (16) are extracted and the results are summerized in Table 1 as below.

Table 1 – Different voltage values required for phase modulation

$\angle \boldsymbol{E_{R-LMM}}$	$\boldsymbol{V_1}$	$\boldsymbol{V_2}$
0	$V_\pi/2$	$V_\pi/2$
$\boldsymbol{\pi}$	$V_\pi/2$	$3V_\pi/2$

To evaluate the modulation efficiency of the LMM, it is important to understand the EO response of the modulator as a function of frequency. To obtain this, we used the calculated output of the LMM from [9]. By assuming the relation between phase shift and the applied voltage to each arm of MZM in LMM shown here in Equation (17)

$$\theta_{1b} = \frac{\pi(V_{1b}+V_{dc})}{V_{p1}} \quad , \quad \theta_{1f} = \frac{\pi(V_{2f}+V_{dc})}{V_{p1}}$$

$$\theta_{2b} = \frac{\pi(V_{2b}+V_{dc})}{V_{p1}} + \frac{\pi}{2} \quad , \quad \theta_{2f} = \frac{\pi(V_{1f}+V_{dc})}{V_{p1}} + \frac{\pi}{2} \tag{17}$$

where angles θ_{1f} and θ_{2f} are the phase shifts experienced by the forward going signals due to the modulation of the effective refractive index of the upper and lower MZI arms, respectively, and similarly θ_{1b} and θ_{2b} are the phase shifts experienced by the backward propagating signals due to the modulation of the effective refractive index of the upper and lower MZI arms. For the upper arm of the MZI, the phase shift is defined by $\theta_1 = \theta_{1b} + \theta_{1f}$. Similarly, for the bottom arm of the MZI the total phase shift of the signal is defined as $\theta_2 = \theta_{2b} + \theta_{2f}$. Voltages V_{1f} and V_{2f} are the applied voltages at the forward going signals to the upper and lower MZI arms, respectively, and similarly V_{1b} and V_{2b} are the applied voltages at the backward propagating signals to the upper and lower MZI arms. For the upper arm of the MZI, the total applied voltage is defined as $V_1 = V_{1b} + V_{1f}$. Similarly, for the bottom arm of the MZI the total applied voltage is defined as $V_2 = V_{2b} + V_{2f}$. Considering these relations in Equation (17) the voltage-based output of LMM can be refined as phase shift-based output of LMM. That means

$$E_{R-LMM}(f, \theta_1, \theta_2) \equiv E_{R-LMM}(f, V_1, V_2) \tag{18}$$

The EO response for intensity modulation of the LMM for phase values of 0 (blue line) and π (red line) are obtained in Figure 4. As it can be observed there is roll-off around 1 GHz for intensity modulation. The efficiency of EO response for intensity modulation is interrupted by counter-propagating signals. At high frequencies the EO response of LMM to tend toward zero since the phase mismatch between the optical and RF waves increases.

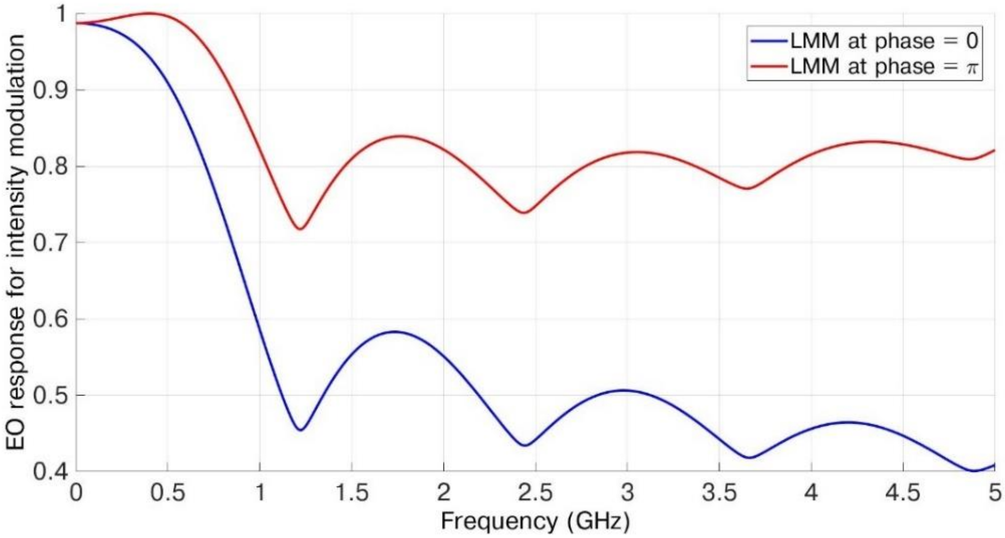

Figure 4 – EO response for intensity modulation of LMM at phase values of 0 and π

The EO response for phase modulation of the LMM for phase values of 0 (blue line) and π (red line) are obtained in Fig. 5. As it can be observed there is roll-off around 1 GHz for intensity modulation. Similar to intensity modulation, the efficiency of EO response for phase modulation is also interrupted by counter-propagating signals. At high frequencies the EO response of LMM to tend toward zero as well.

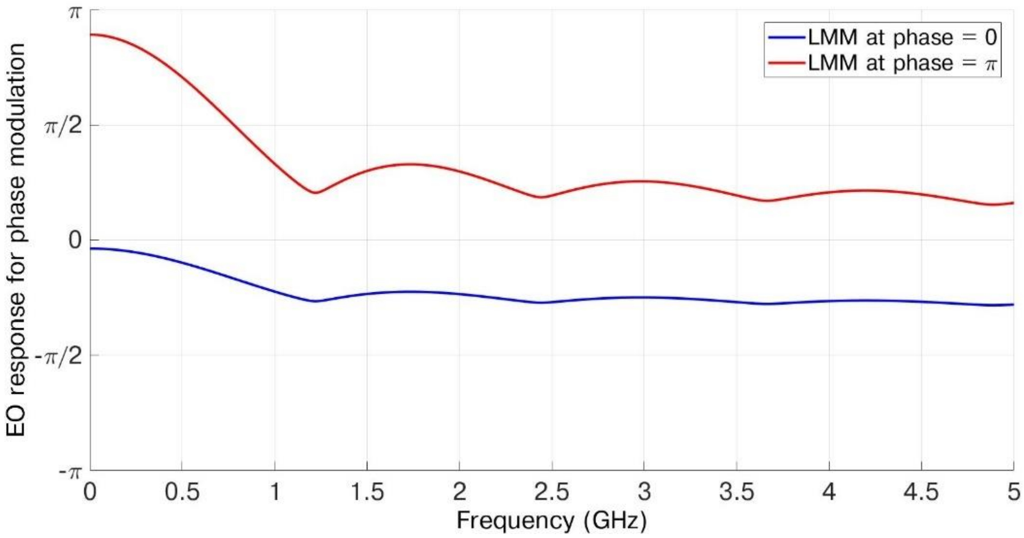

Figure 5 – EO response for phase modulation of LMM at phase values of 0 and π

The difference of EO response for phase modulation of the LMM at phase values of 0 and π is obtained with the blue line in Fig. 6. The EO response of an MZI of the same length without a loop-mirror that is driven with the voltage as the LMM is also included in Fig. 6 (red line).

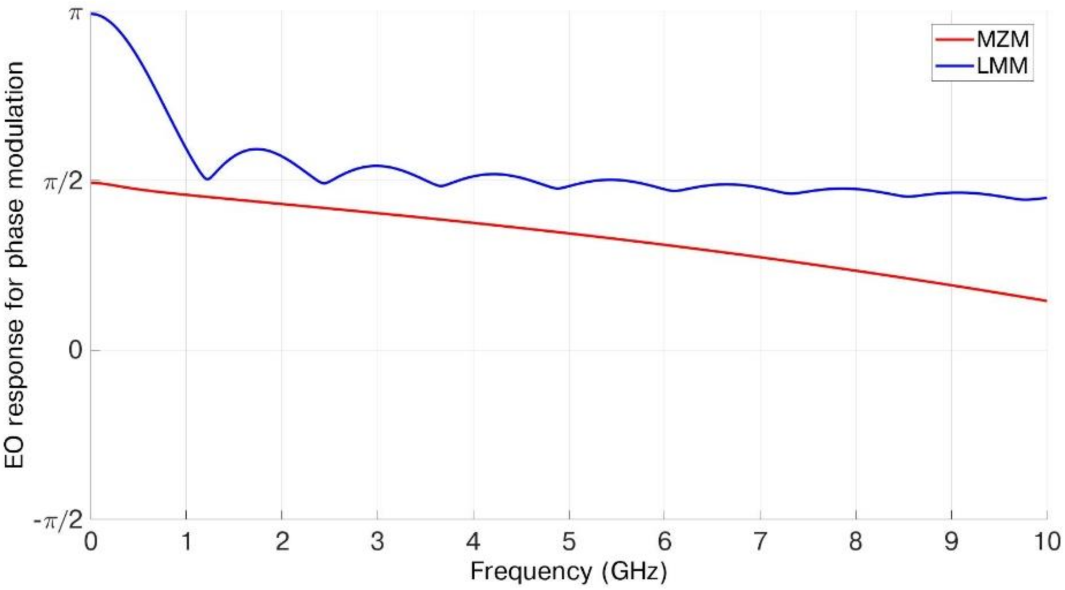

Figure 6 – (blue line) EO response for phase modulation of an LMM, (red line) EO response for phase modulation of a standard MZI driven with the same voltage as the LMM.

The EO response for phase modulation rolls off around 1 GHz. Similar to intensity modulation [9], the efficiency of EO response for phase modulation is also affected by counter-propagating signals. At high frequencies the LMM displays a modulation efficiency comparable to an MZI without a loop-mirror and is modulated with the same drive voltage. However, the LMM can provide twice the modulation depth for frequencies below 1 GHz. This corresponds to the frequency range over which the LMM electrodes can be considered in the lumped regime instead of the traveling wave regime.

6.3 Design and fabrication

The device discussed here was fabricated at the Institute of Microelectronics (IME)/A*STAR through an OpSIS (Optoelectronics Systems Integration in Silicon) Multi-Project Wafer run. PN diodes with dual-drive TW electrodes operated in reverse bias were used to modulate the refractive index of the MZI arms. The length of both modulation regions was 2.28 mm. The power splitters used to form the MZI were two identical adiabatic3dB couplers. In Figure 7, the loop, which has a radius of curvature of 10 µm, is located on the right side and the input and output ports are visible on the left side. The schematic of the device with the electrode configuration is shown in Figure 7 and is similar to the device presented in [6], [7].The geometry of the doping regions is shown in Figure 8.

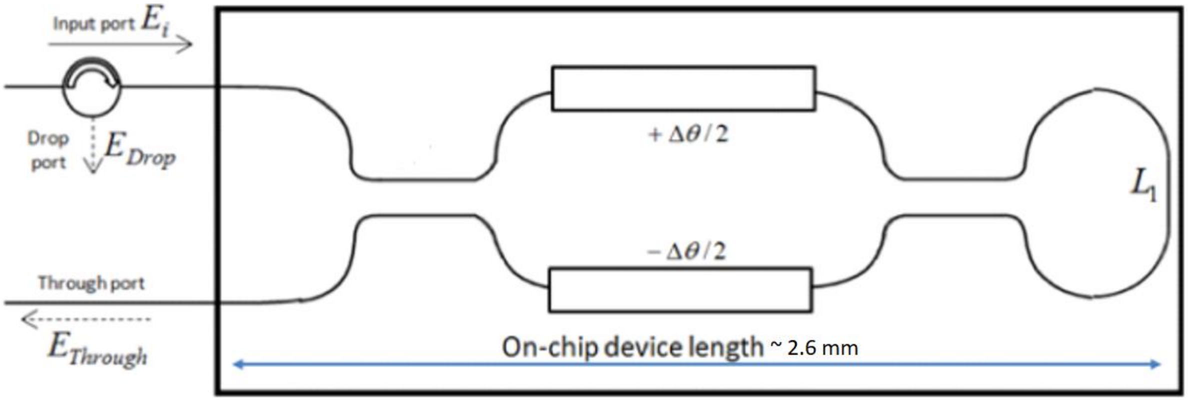

Figure 7 - Schematic of the LMM

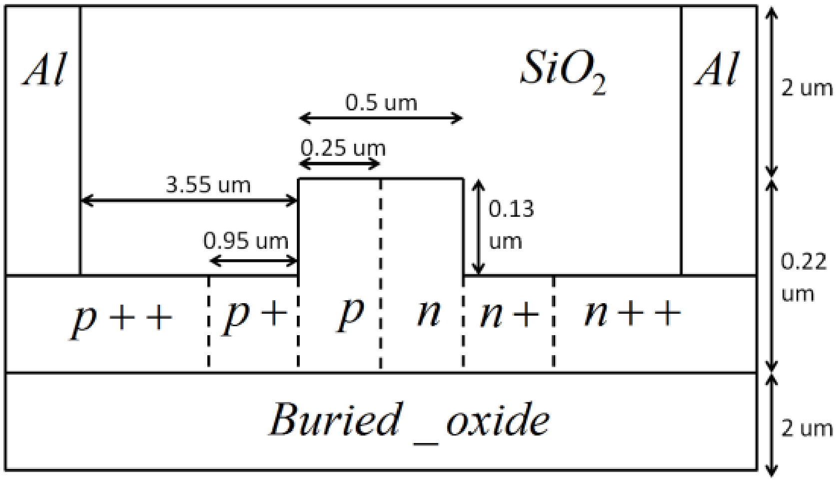

Figure 8- PN junction geometry of the LMM

The measured transmission spectrum of the TW-LMM, normalized to a reference waveguide, is shown for different DC biases in Figure 9. In this figure, the waveguide routing propagation loss is 2.0 dB. The insertion loss due to the pair of each grating coupler is 5.7 dB. The insertion loss of the LMM (without considering the grating couplers) is 8.1 dB. As shown in Figure 9, the FSR of the TW-LMM is 20 nm, and the measured V_π is 5 V, matching the 22 µm length difference between the arms of the MZM. The modulation depth observed is about 25 dB, similar to that reported in [6], [7].

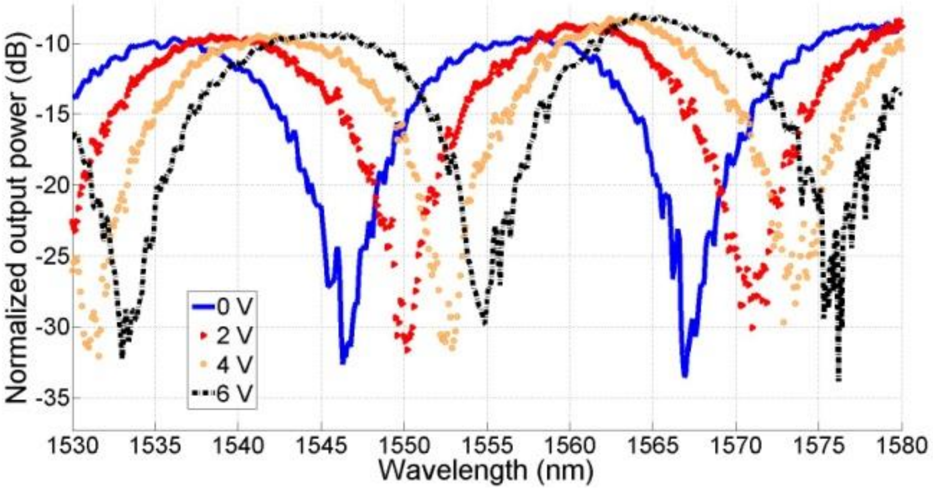

Figure 9 - Normalized transmission spectrum of the LMM with different bias voltages

6.4 Experimental demonstration of DPSK at 10 Gb/s

We tested the modulator by applying a 2^7-1 PRBS signal via a GSGSG probe on one side of the device. The other end of the modulator was terminated with a 50 Ω load to minimize RF reflections. The amplified drive signal was 4.09 Vpp, applied to the lower arm of the device, which operated as a single-drive modulator. A reverse bias voltage of 1.84 V was applied to the modulator using a bias tee. In this experiment, we used a tunable all-fiber delay-line interferometer for DPSK demodulation [3]. At the receiver, a DC voltage of 1.46 V was used to tune the DPSK demodulator to optimize the optical eye diagrams. The experimental setup to evaluate the performance of the LMM for DPSK modulation is illustrated in Figure 10. The DPSK optical eye diagram before processing by the tunable-DPSK demodulator is presented in Figure 10 beside the DCA. With single-drive electrode modulation the LMM could not meet the phase-only modulation requirement. This optical eye diagram indicates compound phase and intensity modulation. We used single-drive electrode modulation because due to fabrication error the other electrode was not functioning properly, and the dual-drive electrode modulation was asymmetric.

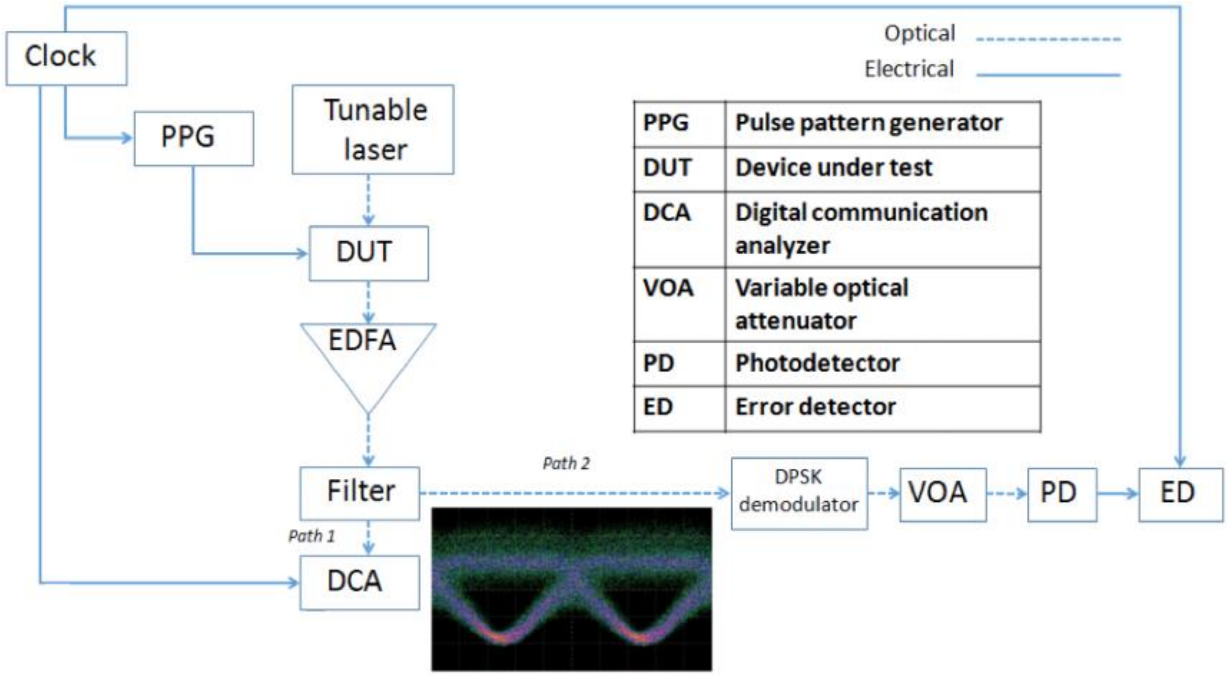

PPG	Pulse pattern generator
DUT	Device under test
DCA	Digital communication analyzer
VOA	Variable optical attenuator
PD	Photodetector
ED	Error detector

Figure 10 – Schematic of the experimental setup used to evaluate the DPSK performance of the LMM

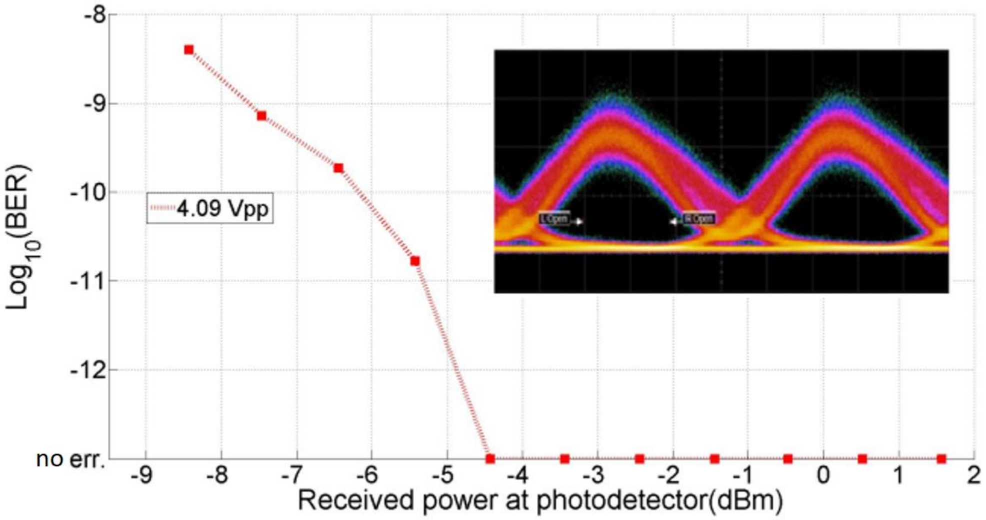

Figure 11 - BER measurements for 10Gbit/s DPSK modulation using 3dB and 6dB attenuators before the RF probe to improve quality of the optical eye diagrams

In the DPSK, signal information remains in the phase variations of the optical signal. As a photodetector is insensitive to phase variations in the optical signal, a demodulator is needed at the receiver front end to convert the phase variations of the DPSK signals to intensity variations. In our demodulated DPSK optical eye diagrams (see Figure 11), the optical eye width was 38 ps, the ER (ER) was 16.7 dB, and the OSNR was 6.7 dB. The BER data we obtained after using the DPSK demodulator is shown in Figure 11. In our experiment, we obtained error-free operation ($\mathbf{BER} < \mathbf{10^{-12}}$) at a received power of -4.5 dBm, as shown in Figure 11; the zero errors line indicates a measurement with zero errors detected in three terabits. Therefore, we can claim error-free operation with a 95% confidence level [12]. This claim is supported by the clear optical eye diagram.

6.5 Chirp analysis for loop-mirror modulator

Any mismatch in the propagation of optical signals via the two arms of an MZI generates chirp. This mismatch can happen either from asymmetric phase shift or asymmetric amplitude (and intensity) at the arms of the MZI. Based on [14-16], the chirp of an optical modulator (α) can be defined as the ratio of the phase modulation to the intensity modulation described by

$$\alpha = \frac{2I\left(\frac{d\phi}{dt}\right)}{\left(\frac{dI}{dt}\right)} \tag{19}$$

where I is the intensity of the optical signal, ϕ is the phase of the optical signal, and t represents time. Chirp results in pulse broadening when $\alpha > 0$ and pulse compression when $\alpha < 0$. For a regular dual-drive MZI, if the effective refractive index per volt changes equally in both arms of the MZI, then in the small-signal regime the chirp can be simplified as [16]:

$$\alpha = \frac{V_1 + \gamma^2 V_2}{\gamma(V_1 - V_2)} \tag{20}$$

where V_1 and V_2 represent the amplitudes of the sinusoidal drive signals, and the scaling factor $0 < \gamma < 1$ is present because of asymmetric splitting/combining ratios in the MZI device. The value of γ can be extracted from the measured DC modulation depth, ε, by Equation (21) below:

$$\gamma = \frac{\sqrt{\varepsilon} - 1}{\sqrt{\varepsilon} + 1} \tag{21}$$

Based on the experimental measurements for the dual-drive LMM we obtain $\gamma \cong 1$. The resulting chirp estimation is equal to

$$\alpha = \frac{V_1 + V_2}{V_1 - V_2} \tag{22}$$

For the series push-pull (SPP) LMM we have $V_1 = -V_2$ and consequently Equation (22) implies that $\alpha_{SPP} = 0$. For the dual-drive (DD) LMM, the voltage condition that is derived from Equation (14) is $V_2 = V_{p1} - V_1$. From Section 6.4 we obtain the values $V_{p1} = 5\ V$ and $V_1 = -4.09\ V$, which yield $\alpha_{DD} = -0.37$. For the sake of comparison, the corresponding values in the case of the existing Mach-Zehnder based silicon optical modulators in [17], [18] are $\alpha \cong -1.7$ for a single-drive MZI and $\alpha \cong 0$ for a dual-drive MZI.

6.6 Conclusion

In the experiment described here, we generated a 10 Gbit/s DPSK signal using a TW-LMM and achieved error-free operation. We presented an analysis of the device and obtained an expression for the conditions that are necessary to obtain arbitrary phase and amplitude output as a function of the two drive voltages. This device has the potential to operate at higher speeds, but we were limited in our demonstration by our BER detector. The drive voltage of the proposed TW-LMM is 4.09 Vpp. Theoretical analysis in [9] shows that in the lumped model, the power consumption of the LMM is one-quarter that of an equivalent TW-MZM with similar drive voltage

[8]. Based on Equation (7) in Chapter 5, the dynamic power consumption of the LMM device at a modulation rate of 10 Gb/s for DPSK modulation is estimated to be 8.4 pJ/bit. Further work would be necessary to generate the phase-only modulation required for DPSK modulation.

References

[1] A. H. Gnauck and P. J. Winzer, “Optical phase-shift-keyed transmission,” *J. Light. Technol.*, vol. 23, no. 1, pp. 115–130, 2005.

[2] H. Zhu *et al.*, “Single-drive push-pull silicon Mach-Zehnder modulator for OOK and BPSK modulation,” in *OECC/ACOFT*, 2014, no. July, pp. 174–175.

[3] F. Scguin and F. Gonthier, “Tunable all-fiber delay-line interferometer for DPSK demodulation,” in *Optical Fiber Communication Conference*, 2005, pp. 5–7.

[4] M. S. Hai and O. Liboiron-ladouceur, “Robust and Compact 45 Gb / s MMI-based SOI-DPSK demodulator for On-chip Optical IO Layer,” in *CLEO*, 2013, pp. 5–6.

[5] M. S. Hai and O. Liboiron-Ladouceur, “Thermally stable 50 Gb/s SOI DPSK demodulator,” in *IEEE Photonic Society 24th Annual Meeting*, 2011, vol. 2, pp. 338–339.

[6] B. Banan, M. S. Hai, E. Lisicka-Skrzek, P. Berini, and O. Liboiron-Ladouceur, “Multichannel transmission through a gold strip plasmonic waveguide embedded in cytop,” *IEEE Photonics J.*, vol. 5, no. 3, 2013.

[7] F. Soltani, M. Menard, and A. G. Kirk, “Low-power 20Gb / s modulator with an integrated loop-mirror,” in *Asia Communications and Photonics Conference (ACP) IEEE/OSA/SPIE sponsored*, 2015.

[8] F. Soltani, M. Menard, and A. G. Kirk, “Optical modulator with an integrated loop-mirror,” in *IEEE Optical interconnects conference (OI)*, 2015.

[9] F. Soltani, M. Menard, and A. G. Kirk, “Integrated silicon photonic reflective modulator for passive optical networks,” in *IEEE/OSA CLEO conference*, 2017.

[10] M. Aamer *et al.*, “10 Gbit/s error-free DPSK modulation using a push-pull dual-drive silicon modulator,” *Opt. Commun.*, vol. 304, no. 1, pp. 107–110, 2013.

[11] F. Soltani, D. Patel, M. Menard, D. V. Plant, and A. G. Kirk, “Low-power DPSK modulation at 10 Gbps using a silicon photonic loop-mirror modulator,” in *IEEE PhotonicsConference (IPC)*, 2016.

[12] Dennis Derickson and M. Müller, *Digital communications test and measurement: High-speed physical layer characterization*. Boston MA USA: Pearson Eduaction, Inc., 2008.

[13] D. A. B. Miller, “Energy consumption in optical modulators for interconnects,” *Opt. Express*, vol.

20, no. S2, pp. A293–A308, 2012.

[14] F. Koyama and K. Iga, “Frequency chirping in external modulators,” *J. Light. Technol.*, vol. 6, no. 1, pp. 87–93, 1988.

[15] R. Li *et al.*, “High-speed low-chirp PAM-4 transmission based on push-pull silicon photonic microring modulators,” *Opt. Express*, vol. 25, no. 12, pp. 13222–13229, 2017.

[16] H. Kim and A. H. Gnauck, “Chirp characteristics of dual-drive. Mach-Zehnder modulator with a finite DC extinction ratio,” *IEEE Photonics Technol. Lett.*, vol. 14, no. 3, pp. 298–300, 2002.

[17] D. J. Thomson *et al.*, “High Performance Mach Zehnder-Based Silicon Optical Modulators,” *IEEE J. Sel. Top. Quantum Electron.*, vol. 19, no. 6, pp. 85–94, 2013

[18] K. Ogawa *et al.*, “20-Gbps Silicon Photonic Waveguide Nested Mach-Zehnder QPSK Modulator,” in *Optical Fiber Communication Conference and Exposition (OFC/NFOEC)*, 2012, p. JTh2A.20.

Chapter 7

Conclusion

7.1 Applications and implications of power-efficient optical switches and modulators

There is an increasing demand for consumer applications requiring larger bandwidth and higher capacities in telecommunication and datacom networks [1]. Optical components with low-power consumption can provide a solution to this demand. This thesis investigates the low-power, high-speed silicon-based optical modulators for broadband applications. We demonstrate for the first time a non-resonant silicon-based integrated photonics optical modulator that combines an MZM with a loop-mirror, resulting in a loop-mirror modulator (LMM).

This thesis is an investigation to explain this hypothesis that resonant devices and non-resonant devices implemented in EO materials are capable to reduce power consumption while achieving high-speed performance. This is a general principle which is in particular applicable to implemented devices in EO effect and can be extended to the devices that are implemented using the plasma dispersion method. The quantitative evidence for the above claim is given in Chapter 3 where we exhibit the switching energy comparison of the resonant (based on FPI) and the non-resonant (based on MZI) EO switches. The derived analytical results show that the resonant switches are suitable for use in optical networks at low frequencies since their power consumption is less than the non-resonant switches. However, the resonant switches have a narrow bandwidth that limits their applications. Furthermore, there is a certain frequency at which the resonant switches have switching energy equal to the non-resonant switches and the demonstrated modulation characteristics of these switches become identical. By an analytical model, in Chapter 3 we show that at frequencies higher than this critical frequency, non-resonant switches are preferable.

The LMM that is designed in Chapter 4 uses carrier depletion with a reversed bias voltage to provide complete modulation. Chapter 4 theoretically affirms that LMM in lumped electrodes regime requires smaller phase shift, and hence it can operate with lower actuation voltage and less power consumption than equivalent MZMs with similar drive voltage [2]. In Chapter 5 we show the results of large signal characterization and big signal measurements of a series push-pull TW-LMM. The maximum rate for OOK modulation before distortion is 20 Gb/s and it has a potential to work at a higher modulation speed with further optimization to reduce the EO velocity mismatch. In Chapter 6 we demonstrate the results of 10 Gb/s DPSK modulation with a dual-drive TW-LMM. These results are obtained with error-free BER operation. The TW-LMM has the potential to operate at higher speeds for DPSK modulation, but we were limited in our demonstration by our BER detector. In addition, using a balanced photodiode might help to show the received eye diagram of the DPSK signal. However, the necessary equipment for this investigation was not available at the time we were doing the DPSK experiments. Moreover, in Chapter 6 we perform an analysis of the TW-LMM and obtain an expression for the optimized performance conditions. This condition is necessary in order to achieve arbitrary phase and amplitude output as a function of the two drive voltages. The characterization results and enhanced features for LMM in both OOK and DPSK modulation are listed in Table 1 as below.

Table 1 – Enhanced features for LMM in OOK and DPSK modulation

Characterization parameters	**OOK modulation**	**DPSK modulation**
Operating bandwidth	40 nm (C-band)	40 nm (C-band)
Maximum modulation speed	20 Gb/s	10 Gb/s
V_π	5 volts	5 volts
V_{pp}	2.6 volts	~ 2.25 volts
Extinction ratio	3 dB	5.3 dB
Insertion loss	2.6 dB	3.0 dB
Footprint	4 mm x 2 mm	3 mm x 2.5 mm
Modulation depth	25 dB	∼25 dB

In addition to the characteristics of LMM that are noted above, we also investigate the EO modulation response of LMM for OOK modulation in Chapter 5. The simulation results show that EO response rolls off very quickly at around 1 GHz in counter-propagation; thus, at higher frequencies the optical signal is only modulated when it propagates in the forward direction. Therefore, at high frequencies, the LMM displays modulation efficiency comparable to that of an MZM without a loop-mirror when both are modulated by the same drive voltage. However, for the same drive voltage, the LMM can provide twice the modulation depth for frequencies below 1 GHz. This corresponds to the frequency range over which the LMM electrodes can be considered as lumped electrodes regime instead of TW electrodes regime. Moreover, since the propagation time inside the loop-mirror is negligible, in this regime, the LMM will efficiently modulate the signal in both co- and counter-propagation.

The LMM is proposed as a reflective modulator for GPON networks. We expect that it can result in significant cost reductions and offer a suitable bandwidth. Our theoretical model in Chapter 4 indicates that the LMM can provide improved performance if its MZM is implemented with a lumped electrode design instead of TW electrodes. As explained in EO bandwidth analysis, counter-propagation modulation in our demonstrator is efficient at low frequencies where the TW electrodes effectively work as lumped one. Thus, in that regime the LMM is able to generate a phase difference between its arms twice as large as an equivalent MZM for the same modulation voltage. To demonstrate this, we recently sent for fabrication an LMM with shorter electrodes (750 µm instead of 2.2 mm) that should operate as a lumped MZM at frequencies higher than 10 GHz based on the microwave model presented in [3].

7.2 Future work

The silicon-based LMM is a cost-efficient solution in comparison to other remote modulation devices such as IL-FP [4], [5], RSOA [6]–[9], and EAM [10]–[14]. Most of the losses of the LMM are due to coupling and routing, which can easily be improved [15]. Besides the back-to-back measurements, a more explicit way to show the performance of the LMM would be to consider transmission experiments over a few km of fiber (for the intra-data center and PON applications) or at least 80 km (for long-haul applications). In this case a discussion of the penalties should also be included.

Some other modifications that can be done to reduce the insertion loss are developments in the end-face polishing techniques [16], and improvements in the alignment of connectors [17]. Furthermore, in comparison to the low-power and high-speed modulators based on ring resonators, the LMM design is based on MZI and has a broad bandwidth with high fabrication tolerance. These advantages in addition to the colorless nature of the device, makes LMM a significant candidate to be considered in WDM systems. In future work, we will examine a revised LMM lumped design which contains shorter electrodes. The lumped model will provide higher modulation speed with lower power consumption than the methods that were previously mentioned. Furthermore, as reported in [18]–[20], the velocity match of optical and RF signals is not an issue in the lumped electrode regime. It is important to indicate that in the characterization of the proposed LMM, we have not measured the polarization dependency of this device. However, the LMM is designed for polarization-independent operations.

Hybrid silicon and EO polymer photonic devices combine the low-power actuation of polymers and the small footprint of silicon photonics to make the desired device with high modulation efficiency and large bandwidth. The LMM design has the advantage of low-power consumption as explained in previous sections. Its power consumption should be one-quarter that of conventional MZI and this makes it an innovative idea in power-efficient optical modulation. It is possible to combine the low-power consumption of EO polymer with the low-power advantage of loop-mirror devices. Eventually the expected design will be the LMM fabricated with EO polymer cladding as a highly power-efficient optical modulator. Also, because EO polymers are not limited by the drift velocity of charge carriers, the fabricated modulator should achieve high speeds as well. This can respond to the demand for a low-power and high-speed optical device. As one of the short-term future objectives for this prototype, the 40 Gbps modulation rate for telecommunication applications and 10 Gbps modulation rate for datacom applications can be targeted with this hybrid silicon and EO polymer device. However, reaching solutions with faster modulation rate can be considered for long-term future of this prototype. The next step will be to design and fabricate this hybrid optical modulator through available foundries. Then as a post-fabrication process, the provided EO polymer will be deposited to form the cladding. This device will be the building block that enables the implementation of novel integrated high-performance optical modulators. In addition to telecommunication and datacom, EO polymer modulators may also find applications to incorporate the optical switches and modulators in high bandwidth fiber and wireless communication devices, video transmission and radio frequency distribution, ultrafast analog to digital converter, optical detection and radar systems [21].

References

[1] C. H. Lee, W. V. Sorin, and B. Y. Kim, “Fiber to the home using a PON infrastructure,” *J. Light. Technol.*, vol. 24, no. 12, pp. 4568–4583, 2006.

[2] F. Soltani, M. Menard, and A. G. Kirk, “Optical modulator with an integrated loop mirror,” in *IEEE Optical interconnects conference (OI)*, 2015.

[3] D. Patel, V. Veerasubramanian, S. Ghosh, A. Samani, Q. Zhong, and D. V Plant, “High-speed compact silicon photonic Michelson interferometric modulator.,” *Opt. Express*, vol. 22, no. 22, pp. 26788–802, 2014.

[4] Q. T. Nguyen *et al.*, “24 channels colorless WDM-PON with L-band 10 Gb / s downstream and C-band 2 . 5 Gb / s upstream using multiple- wavelengths seeding sources based on mode-locked lasers,” in *OFC/NFOEC*, 2010.

[5] S. M. Lee, K. M. Choi, S. G. Mun, J. H. Moon, and C. H. Lee, “Dense WDM-PON based on wavelength-locked Fabry-Pérot laser diodes,” *IEEE Photonics Technol. Lett.*, vol. 17, no. 7, pp. 1579–1581, 2005.

[6] B. Schrenk, G. De Valicourt, M. Omella, J. A. Lazaro, R. Brenot, and J. Prat, “Direct 10-Gb/s modulation of a single-section RSOA in PONs with high optical budget,” *IEEE Photonics Technol. Lett.*, vol. 22, no. 6, pp. 392–394, 2010.

[7] G. De Valicourt *et al.*, “High gain (30 dB) and high saturation power (11 dBm) RSOA devices as colorless ONU sources in long-reach hybrid WDM/TDM-PON architecture,” *IEEE Photonics Technol. Lett.*, vol. 22, no. 3, pp. 191–193, 2010.

[8] Y. C. Chung, “Recent advancement in WDM PON technology,” in *37th European Conference and Exposition on Optical Communications*, 2011, p. Th.11.C.4.

[9] K. Y. Cho, J. H. Chang, B. S. Choi, Y. Takushima, and Y. C. Chung, “Demonstration of 25.78-Gb/s, 20-km reach WDM PON using directly-modulated bandwidth-limited RSOA,” in *Optical Fiber Communication Conference and Exposition and the National Fiber Optic Engineers Conference*, 2011, pp. 1–3.

[10] D.-H. Lee *et al.*, “Design and performance of 10-Gb/s L-band REAM-SOA for OLT Transmitter in next generation access networks,” *Opt. Express*, vol. 23, no. 3, p. 2339, 2015.

[11] K. Lawniczuk *et al.*, “40-Gb/s colorless reflective amplified modulator,” *IEEE Photonics Technol. Lett.*, vol. 25, no. 4, pp. 341–343, 2013.

[12] H. Kim, D. C. Kim, K. Kim, B. Choi, and O. Kwon, “10.7 Gb/s reflective electroabsorption modulator monolithically integrated with semiconductor optical amplifier for colorless WDM-PON,” *Opt. Express*, vol. 18, no. 22, pp. 23324–23330, 2010.

[13] B. Schrenk, J. A. Lazaro, C. Kazmierski, and J. Prat, “Colorless FSK demodulation and detection with integrated fabrypérot-type SOA/REAM,” *IEEE Photonics Technol. Lett.*, vol. 22, no. 13, pp. 1002–1004, 2010.

[14] C. Kazmierski, “Electro-Absorption-Based Fast Photonic Integrated Circuit Sources for Next Network Capacity Scaling,” *J. Opt. Commun. Netw.*, vol. 4, no. 9, p. A8, 2012.

[15] A. Michaels and E. Yablonovtich, “Inverse Design of Near Unity Efficiency Perfectly Vertical Grating Couplers,” vol. 25, no. 15, pp. 119–122, 2017.

[16] S. I.-E. Lin, “Effect of polishing conditions on terminating optical connectors with spherical convex polished ends.,” *Appl. Opt.*, vol. 41, no. 1, pp. 88–95, 2002.

[17] M. Margolin and I. Grois, “Fiber optic connector,” US4705352 A, 10-Nov-1987.

[18] G. Dickinson, D. a Chapman, and D. a Gorham, “Properties of the fiber reflection Mach-Zehnder interferometer with identical couplers.,” *Opt. Lett.*, vol. 17, no. 17, pp. 1192–1194, 1992.

[19] B. Desruelle, E. Desurvire, and S. Bigo, “Analysis of the polarization group-velocity dispersion effect in polarization-independent nonlinear-optical loop mirror demultiplexers,” *Opt. Lett.*, vol. 20, no. 5, pp. 516–518, 1995.

[20] C. A. Millar, D. Harvey, and U. Paul, “Fiber reflection Mach-Zehnder interferometer,” *Opt. Commun.*, vol. 70, no. 4, pp. 1–5, 1989.

[21] L. R. Dalton *et al.*, “From molecules to opto-chips : organic electro-optic materials,” *J. Mater. Chem.*, vol. 9, no. 9, pp. 1905–1920, 1999.